THESIS FOR THE DEGREE OF DOCTOR OF ENGINEERING

Nanoplasmonic Alloy Hydrogen Sensors

A Quest for Fast, Sensitive and Poisoning-Resistant Hydrogen Detection

FERRY ANGGORO ARDY NUGROHO

CHALMERS

Department of Physics
CHALMERS UNIVERSITY OF TECHNOLOGY
Gothenburg, Sweden 2018

Nanoplasmonic Alloy Hydrogen Sensors
A Quest for Fast, Sensitive and Poisoning-Resistant Hydrogen Detection
FERRY ANGGORO ARDY NUGROHO
ISBN: 978-91-7597-717-1

Doktorsavhandlingar vid Chalmers tekniska högskola
Ny serie nr 4398
ISSN 0346-718X

Department of Physics
Chalmers University of Technology
SE-412 96 Gothenburg
Sweden
Telephone + 46 (0)31-772 3007

Cover: A cartoon representation of the superior hydrogen sensing characteristics of an alloy nanoplasmonic sensor. Art by Nesia Anindita (nesianindita.com).

Printed at Chalmers Reproservice
Gothenburg, Sweden 2018

Nanoplasmonic Alloy Hydrogen Sensors
A Quest for Fast, Sensitive and Poisoning-Resistant Hydrogen Detection

Ferry Anggoro Ardy Nugroho
Department of Physics
Chalmers University of Technology

Abstract

The hydrogen economy proposes hydrogen gas as the main energy carrier thanks to its high energy density and the possibility to produce it in a sustainable way without CO_2 emission. However, the wide flammability range of hydrogen-air mixtures dictates that hydrogen sensors will be a mandatory accessory to any appliance or vehicle fueled by hydrogen. Exploiting a phenomenon occurring at the nanoscale, a new type of hydrogen sensor based on the strong interaction of light with metal nanoparticles has rapidly developed in the past years. These so-called nanoplasmonic hydrogen sensors rely on hydride-forming metal nanoparticles that sustain localized surface plasmon resonance (LSPR); a collective oscillation of electrons in the nanoparticles induced by irradiated light. The energy at which the resonance occurs depends on the permittivity, as well as size and shape of the nanoparticles. Since both size and permittivity change significantly when a metal transforms into a metal hydride upon absorption of hydrogen, this effect can be used to detect it. To this date, palladium (Pd) has been the prototype material for both fundamental studies related to hydrogen sorption mechanisms in metals and in next-generation hydrogen detection devices across all sensing platforms. Specifically for the hydrogen detection, however, pure Pd does not satisfy the required sensing performance standard due to its inherent hysteresis during hydrogen absorption and desorption and slow kinetics. Furthermore it is also prone to deactivation by species like carbon monoxide and nitric oxides.

To address these limitations, in this thesis a new class of plasmonic hydrogen sensors based on noble metal alloy nanoparticles comprised of Pd, Gold (Au) and Copper (Cu) is explored. To enable such sensors, we first developed a nanofabrication method to produce alloy nanoparticles with precise control of their composition, size and shape. Investigating the fundamental properties of these alloy systems upon interaction with hydrogen, we found a universal correlation between the amount of hydrogen absorbed and the optical response, independent of alloy composition. Moreover, we demonstrated how segregation of Au atoms to surface of PdAu nanoparticles can be measured as a distinct change in the plasmonic response. Focusing on the optical hydrogen sensor application, we then studied in detail the performance of various PdAu, PdCu and PdAuCu alloys, as well as the use of thin polymer selective membrane coatings to prevent sensor deactivation by poisoning gases. As the main result, we created sensors with hysteresis-free sub-second response with sub-5 ppm sensitivity that meet or exceed stringent performance targets. To push the concept closer to application, we also demonstrated the integration of alloy nanoparticles with optical fibers for hydrogen sensing.

Keywords: sensors, localized surface plasmon resonance, plasmonic sensors, indirect nanoplasmonic sensing, nanofabrication, palladium, alloy nanoparticles, hydrogen sensors, polymers, fiber optics, carbon capture and storage

“And the best of people are those who are most beneficial to people.”

Muhammad ibn Abdullah

LIST OF APPENDED PAPERS

This thesis is based on the work presented in the following publications:

Paper I

Bottom-Up Nanofabrication of Supported Noble Metal Alloy Nanoparticle Arrays for Plasmonics

Ferry A. A. Nugroho, Beniamino Iandolo, Jakob B. Wagner and Christoph Langhammer

ACS Nano, 10 (2), 2871–2879 (2016)

Paper II

Universal Scaling and Design Rules of Hydrogen-Induced Optical Properties in Pd and Pd-Alloy Nanoparticles

Ferry A. A. Nugroho, Vladimir P. Zhdanov and Christoph Langhammer

Submitted for publication

Paper III

Hysteresis-Free Nanoplasmonic Pd –Au Alloy Hydrogen Sensors

Carl Wadell‡, Ferry A. A. Nugroho‡, Emil Lidström, Beniamino Iandolo, Jakob B. Wagner and Christoph Langhammer

(‡equal contribution)

Nano Letters, 15 (5), 3563–3570 (2015)

Paper IV

Rationally Designed Binary and Ternary Alloy Nanoparticles for Poisoning-Resistant Nanoplasmonic Hydrogen Sensors with Hysteresis-Free Sub-Second Response

Iwan Darmadi‡, Ferry A. A. Nugroho‡, Shima Kadkhodazadeh, Jakob B. Wagner and Christoph Langhammer

(‡equal contribution)

Submitted for publication

Paper V

Nanoparticle – Polymer Hybrid Optical Hydrogen Sensors

Ferry A. A. Nugroho, Iwan Darmadi, Herman Schreuders, Arturo Susarrey-Arce, Alice Bastos da Silva Fanta, Lars Bannenberg, Shima Kadkhodazadeh, Jakob B. Wagner, Vladimir P. Zhdanov, Tomasz Antosiewicz, Bernard Dam and Christoph Langhammer

In manuscript

Paper VI

A Fiber-Optic Nanoplasmonic Hydrogen Sensor via Pattern-Transfer of Nanofabricated PdAu Alloy Nanostructures

Ferry A. A. Nugroho, Robin Eklund, Sara Nilsson and Christoph Langhammer

Submitted for publication

Paper VII

Probing Surface Segregation in Metal Alloy Nanoparticles using Plasmonic Sensing

Ferry A. A. Nugroho, Arturo Susarrey-Arce, Shima Kadkhodazadeh, Jakob B. Wagner and Christoph Langhammer

In manuscript

Paper VIII

UV –Visible and Plasmonic Spectroscopy of the CO_2 Adsorption Energetics in a Microporous Polymer

Ferry A. A. Nugroho, Chao Xu, Niklas Hedin and Christoph Langhammer

Analytical Chemistry, 87 (20), 10161–10165 (2015)

RELATED PAPERS NOT INCLUDED IN THIS THESIS

Colloidal Silica as Solid Carbon Dioxide Sorbent

Sara Nilsson, Ferry A. A. Nugroho, Michael Persson and Christoph Langhammer

In manuscript

Exploring the Origin of the Extraordinary Thermal Stability of ITIC based Solar Cells

Liyang Yu, David Kiefer, Renee Koon, Deping Qian, Johannes Benduhn, Ferry A. A. Nugroho, Eva Olsson, Christoph Langhammer, Koen Vandewal, Feng Gao and Christian Müller

In manuscript

Grain-Boundary-Mediated Hydriding Phase Transformations in Individual Polycrystalline Metal Nanoparticles

Svetlana Alekseeva, Alice Bastos da Silva Fanta, Beniamino Iandolo, Tomasz Antosiewicz, Ferry A. A. Nugroho, Jakob B. Wagner, Andrew Burrows, Vladimir P. Zhdanov and Christoph Langhammer

Nature Communications, 8 (1) 1084 (2017)

A Fullerene Alloy Based Photovoltaic Blend with a Glass Transition above 200 ^{o}C

Amaia Diaz de Zerio Mendaza, Armantas Melianas, Ferry A. A. Nugroho, Olof Bäcke, Eva Olsson, Christoph Langhammer, Olle Inganäs and Christian Müller

Journal of Materials Chemistry A, 5 (8) 4156–4162 (2017)

Plasmonic Nanospectroscopy for Thermal Analysis of Organic Semiconductor Thin Films

Ferry A. A. Nugroho, Amaia Diaz de Zerio Mendaza, Camilla Lindqvist, Tomasz Antosiewicz, Christian Müller and Christoph Langhammer

Analytical Chemistry, 89 (4) 2575–2582 (2017)

Topographically Flat Nanoplasmonic Sensor Chips for Biosensing and Materials Science

Ferry A. A. Nugroho, Rickard Frost, Tomasz Antosiewicz, Joachim Fritzsche, Elin Larsson Langhammer and Christoph Langhammer

ACS Sensors, 2 (1) 119–127 (2017)

Hydride Formation Thermodynamics and Hysteresis in Individual Pd Nanocrystals with Different Size and Shape

Svetlana Syrenova, Carl Wadell, Ferry A. A. Nugroho, Tina A. Gschneidtner, Yuri A. Diaz Fernandez, Giammarco Nalin, Dominika Świtllik, Fredrik Westerlund, Tomasz J. Antosiewicz, Vladimir P. Zhdanov, Kasper Moth-Poulsen and Christoph Langhammer

Nature Materials, 14 (12), 1236–1244 (2015)

PATENT APPLICATIONS

Method for Determining Thickness of a Material Deposited on a Plasmonic Sensor Arrangement.
Christoph Langhammer, Ferry A. A. Nugroho and Tomasz Antosiewicz
Publication number 17173955.0 - 1554.

Surface Plasmon Resonance Gas Sensor, Gas Sensing System, and Gas Sensing Method

Bengt Kasemo, Christoph Langhammer and Ferry A. A. Nugroho

PCT/EP2014/078484, publication number WO2015091811 A1

MY CONTRIBUTIONS TO THE APPENDED PAPERS

Paper I Fabricated all samples and performed the optical characterization. Wrote the first draft of the paper.

Paper II Performed all the experimental work and related analysis. Wrote the first draft of the paper.

Paper III Fabricated all samples and performed all the measurements. Analyzed the data together with C.W. and prepared the figures for the paper.

Paper IV Performed the experimental work and related analysis together with I.D. (except the QCM measurements and XPS and electron microscopy analysis). Co-wrote the first draft of the paper.

Paper V Performed the experimental work and related analysis (except deposition of PTFE and XPS and electron microscopy analysis). Co-wrote the first draft of the paper.

Paper VI Co-supervised the master student working on the project (R.E.). Performed part of experimental work and related analysis. Wrote the first draft of the paper.

Paper VII Fabricated the samples and characterized their optical and hydrogen sorption properties. Wrote the first draft of the paper.

Paper VIII Fabricated all sensor surfaces (the PIM-1 polymer was supplied by our collabor) and performed all the measurements (except the physical characterization of the polymer and the gravimetric CO_2 sorption experiments). Wrote the first draft of the paper.

Contents

1 Introduction

On May 6th 1937, the German commercial passenger airship *Hindenburg*, was scheduled to land in New Jersey, USA, after crossing the Atlantic ocean from Frankfurt, Germany. The air-travel was made possible by relying on a hydrogen-filled "balloon" (famously known as Zeppelin) to provide the buoyancy. The journey was deemed monumental as it was the first Hindenburg arrival to the USA and thus numerous reporters and news coverage were gathered to broadcast the event. At a mere moment before Hindenburg docked, it suddenly caught fire and was quickly engulfed in flames. In less than a minute, the biggest and most technologically advanced airship at the time crashed to the ground. The fatalities included 35 out of the total 97 on-board passengers and crewmen.

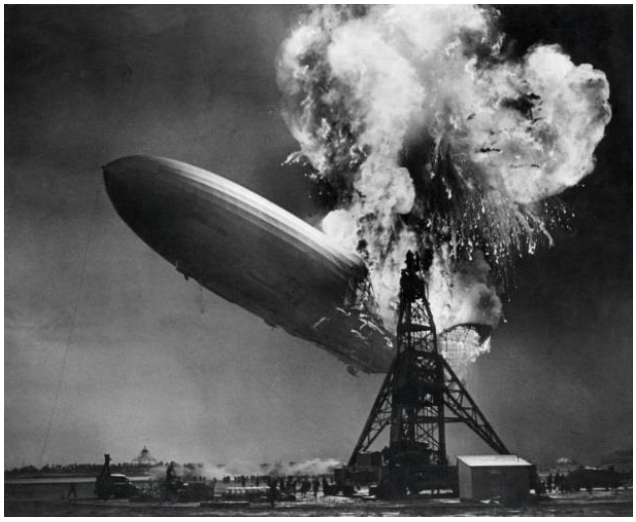

Figure 1.1. Hindenburg disaster. *The Hindenburg airship, the biggest and most technological advanced airship at the time, caught fire when it attempted to dock. This historical event was caught in films and many photographs and thus was widely publicized, triggering the end of the airship era. The photo is reproduced from ref. 1. © Nationaal Archief/Spaarnestad Photo Nederlands.*

This tragedy brought an end to the age of the rigid airship, which previously held a stellar record of 30 years accident-free operation (an equivalent of more than 2000 flights carrying tens of thousands passengers in commercial Zeppelins), and made way for the age of passenger airplanes. The crash was the first major technological disaster caught on film, and the sight was thus widely embedded in the public's consciousness. Despite the emergence of many theories on what caused the fire that appeared years later (the strongest one being the ignition of the balloon fabric by static electricity), public opinion back then had already blamed one culprit: the (leakage of) hydrogen gas. Hydrogen thus started being perceived as a dangerous gas. This prejudice worsened during the war period, when nuclear and, in particular, hydrogen bombs

were on everybody's lips. Even tough probably exaggerated, the public fear and tainted view of hydrogen was not at all unjustified. Hydrogen is indeed flammable when mixed with air and has a wide flammability range (4–75 vol.%). Furthermore, it can be ignited at relatively low energy such that an invisible electrostatic static spark can be enough.

On the other hand, hydrogen has great potential as one of the key enablers for a more sustainable society, for example when used as energy carrier. Thus, when a concept to use hydrogen as the main energy carrier was actually proposed many years later after the Hindenburg accident, one of the most important challenges has been how to change the public view on hydrogen by ensuring its safe use without any compromise.

1.1 Hydrogen Economy

Imagine a situation where the fuel we use (*e.g.* for transportation or in industry) generates *only* water as by-product and will never run out. Well, actually, this is not at all pure imagination. Hydrogen, the *smallest* yet most abundant element in the universe, if used as fuel, actually carries most energy per unit mass. Specifically, it has about three times the mass energy density of gasoline and seven times of the one of coal,[2] and it enables high efficiency during combustion.[3] In the 1970s, the vision of a world powered by hydrogen was coined; the hydrogen economy.[4,5] In this scenario, hydrogen is the center of a fully sustainable and carbon-free energy cycle. The idea is to use sustainable energy sources (*e.g.* solar and wind energy) to split water into hydrogen and oxygen. The hydrogen produced is then stored until the energy is needed. Finally, when the hydrogen is combusted or used to produce electricity in a fuel cell, the only waste product is water. This creates a truly sustainable energy cycle that is free from CO_2 emissions (**Figure 1.2**), which in the long term is predicted to improve the air quality, climate and, consequently, our health.[3]

Despite its very appealing prospects, we have not seen the hydrogen economy implemented at a large scale yet (though we can and *should* be confident as *e.g.* commercial hydrogen cars are already available and massive hydrogen fuelling infrastructures are being built[6]). The reason is that there still are numerous technological hurdles that need to be addressed before the concept can reach widespread use - for example to find efficient ways to produce, store and utilize hydrogen. Simultaneously, also the safety aspects of the hydrogen economy have to be addressed to make sure that the general public will be able to utilize hydrogen technologies in everyday life with at least the same level of safety and comfort as with today's fossil fuels. As a consequence, the development of *reliable* hydrogen sensors is crucial in the deployment of a safe hydrogen economy. Considering the risk, it becomes mandatory for any appliances using hydrogen (fuel) and also the related infrastructures to be equipped with hydrogen sensors. For example, no less than 15 hydrogen sensors are installed in the existing commercial hydrogen fuel cell cars to ensure a safe operation.[7] Hence, hydrogen sensors will play a critical role for successful realization of hydrogen economy. Furthermore, hydrogen sensors are already today also widely used in industrial process monitoring and in health diagnostics, further adding to their wide relevance.[8–12]

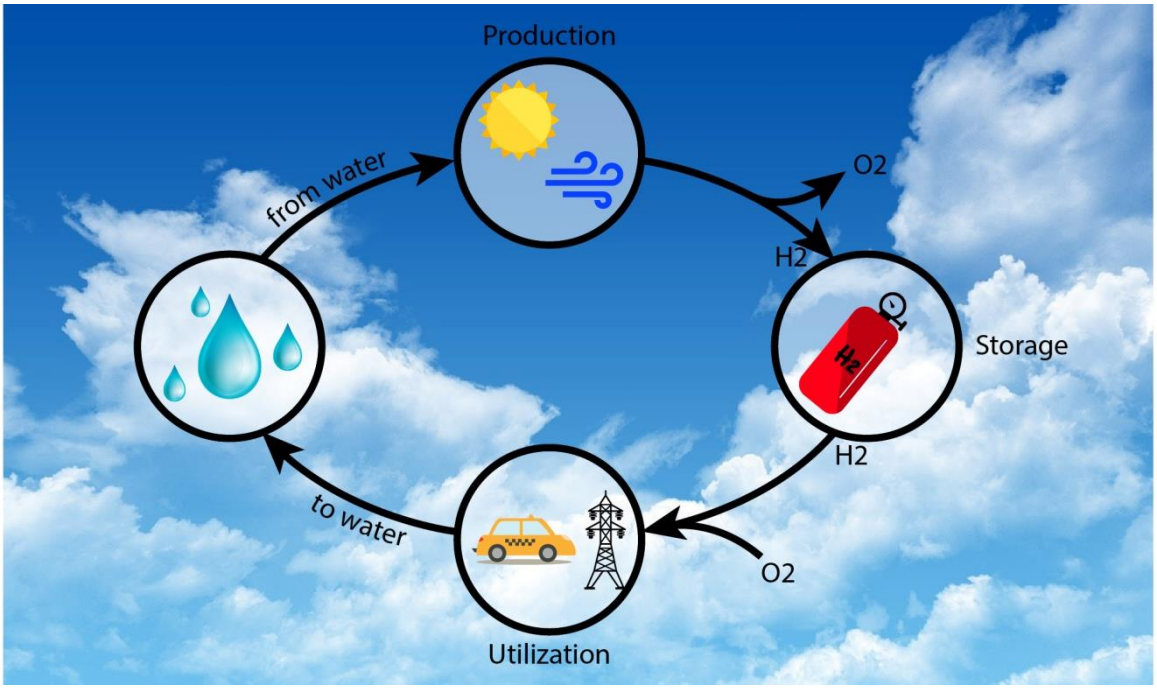

Figure 1.2. The hydrogen economy. *Hydrogen is produced by splitting water with electricity generated from sustainable energy sources, such as solar and wind. The hydrogen is then stored and distributed to users, where it is converted back into electrical energy in a fuel cell. The only waste product is water and, thus, the loop is closed. All the icons used in the schematic and the background picture are adapted from ref. 13 and ref. 14, respectively.*

1.2 Hydrogen Sensors

At ambient pressure and temperature hydrogen is a colorless, odourless and tasteless gas. A system that can detect hydrogen, which is seemingly non-existent to the human senses, is thus crucial. Hence, throughout the years, a variety of different hydrogen sensing schemes have been developed. Most of them rely on measuring a change in a physical or chemical property of a material as it is exposed to hydrogen. The change in the material upon interaction with hydrogen can then be converted into a measurable quantity that can be read by an observer or an instrument. This conversion is done by the signal transducer, which is an integral part of a sensor device. Sensors are thus usually classified based on the energy detected and converted by the transducer;[15] *i.e.* optical, mechanical, gravitational, electric, thermal and magnetic sensors can be distinguished. For hydrogen detection, most commonly a material that reacts directly with hydrogen is used as the transducer, with Palladium (Pd) being the most prominent example.[16] To this end, Pd-based hydrogen sensors employing different transducing mechanisms such as electrical and optical have been developed at the lab scale and are also available as commercial products.[17–20]

1.2.1 Requirements and Challenges

The requirements for hydrogen sensors are different depending on the application. Situations where users are in direct contact with hydrogen demand stricter requirements than those where users are not in direct contact with hydrogen. Hence, it is not surprising that the most stringent

regulations and demands come from the automotive industry, since in the context of a hydrogen-powered vehicle, exposure to hydrogen is inevitable *e.g.* when driving and fuelling. For stationary applications such as power stations, the requirements are less stringent. **Table 1.1** summarizes some of the hydrogen sensor requirements for stationary and automotive applications defined by various sources such as hydrogen detection ISO standards[21] and EU's integrated project on hydrogen storage systems.[22] It is important to note that the requirements vary depending on the source. Therefore, the presented table here by no means is intended to provide a complete data set, but meant to provide a relevant overview of the typical mandatory performance defined by some of the key stakeholders of hydrogen sensing technology.

Table 1.1 Typical performance requirements for hydrogen sensors in stationary and automotive applications.[23]

	Stationary	Automotive
Measuring range	Up to 4 vol.% H_2 (survive 100%)	
Lower detection limit	< 0.1 vol. %	
Response time (t_{90})	< 30 s	< 1 s
Recovery time (t_{10})	< 30 s	< 1 s
Accuracy	±10 %	±5 %
Ambient temperature	-20 to +50 ºC	-40 to +125 ºC
Ambient pressure	80–110 kPa	62–107 kPa
Ambient relative humidity	20–80%	0–100%
Lifetime	> 5 years	

The most striking difference between the two applications is related to the sensor speed. While stationary applications require sensor response times to 4 vol.% H_2 exposure as long as 30 s, automotive application demands detection in less than 1 s. As of now, very few sensors, including those developed only at the lab scale, satisfy this stringent response time target required in automotive application. Furthermore, this target has recently been made even tougher in the standard released by the US Department of Energy (DoE), where detection in less than 1 s is required at any hydrogen pressure from 0.1–10 vol.% H_2;[24] a performance that has not been achieved by any sensor reported to date.[25]

Even when putting the response speed requirement aside, meeting all the other performance targets is not at all a trivial task. The sensors are required to have a reasonable dynamic range while at the same time having high sensitivity and accuracy. Furthermore, excellent stability must also be achieved as they are expected to maintain their functionality amid widely different environments (variation in temperature and humidity, as well as other trace gases) for long time.

As mentioned above, current state-of-the-art hydrogen sensors employ Pd as transducer material. This is motivated by its intrinsic high selectivity to H_2 (*i.e.* the signal changes correspond exclusively to the presence of H_2 and are only to a very small extent caused by other species).[26] However, Pd essentially falls short in most other respects. For example, it responds quite slowly, exhibits very narrow dynamic range and features hysteresis,[27] which renders the measured signal to depend on the sensor history and thus results in ambiguous readout. Lastly, Pd is prone to deactivation (*i.e.* reduced or even loss of sensing functionality) by a number of gases, such as carbon monoxide (CO), sulfuric compounds and hydrocarbons, even at trace amounts.[19,20] This severely limits the usage and lifetime in situations where these gases are inevitably present *e.g.* in industrial process and, in the case of CO, also at ambient conditions were it is present in air at about 0.2 ppm.[28]

Over the years, numerous different sensing architectures have been developed, typically to alleviate each of the problems above *separately*.[20,25,26,29,30] The ultimate goal tackled in this thesis is to develop a sensing platform that is able to meet all of the performance targets *simultaneously*. In other words, the goal is to develop a platform that is versatile and robust enough to allow a multitude of modifications targeting different shortcomings, without compromising with the overall functionality. At the end, it is also highly desirable if the platform is scalable, so that low-cost production can be realized. Out of many different types of hydrogen sensors proposed and developed, I believe that *nanoplasmonic sensors*[26,31] are one of the, if not *the*, candidate(s) to be the core of next-generation high performance hydrogen sensor devices that are able to address all of the requirements outlined above.

1.2.2 Nanoplasmonic Hydrogen Sensors

Richard Feynman, a Noble Laureate and a *great* physicist, noted in his visionary lecture "*There is plenty of room at the bottom*" that the revolution in science and technology would be driven by something *very* small.[32] Particularly at the nanometer scale (a millionth time smaller than a centimeter!), the world is not the same as at the macroscopic scales we are living, as things may behave significantly, or even totally, differently, which may lead to the emergence of novel phenomena. For example, the shiny look of our golden rings will become red, green, or blue, depending on the size, if they are shrunk to the nanoscale, as shown by Larsson et al. who fabricated gold nanorings with various sizes of 75–150 nm (they do not even fit a bacteria's "body"!).[33] Exploiting these new properties opens the door to new technological advances in almost every aspect of our lives.

One of the most interesting nanoscale phenomena is the so-called *localized surface plasmon resonance* (*LSPR*). LSPR occurs in a metal particle smaller than the wavelength of light and constitutes the heart of the research field known as *nanoplasmonics*. LSPR makes nanoparticles exhibit efficient light scattering and absorption that depend on their size and shape. Historically, LSPR has empirically been exploited for nearly 1700 years, as shown by the *Lycurgus cup* crafted by a Roman glass artist from the 4th century A.D. (**Figure 1.3**). The Roman craftsman successfully (and unknowingly?[34]) incorporated small colloidal metallic particles of gold, silver and copper into the glass,[35] which results in the different colors exhibited when the glass is seen

in reflected and transmitted light. The reason why the cup displays different colours is the different scattering and absorption, respectively, exhibited by the metal nanoparticles.

Figure 1.1. The Lycurgus cup. *The famous Roman-era cup shows different coloration, i.e. green and red, when it is viewed in reflected and transmitted light, respectively. The phenomenon is due to the different absorption and scattering efficiencies of the metal nanoparticles dispersed in the glass. The photos are reproduced from the web page of the British Museum.*[36] *© Trustees of the British Museum.*

Despite being "employed" for more than a millennium, it is not until the last century when the characteristic optical properties of noble metal nanoparticles were unearthed in the context of colloidal chemistry, which allowed their controlled synthesis. The first step towards understanding the phenomenon was taken by Gustav Mie, a German scientist, who explained the strong interaction of light with metal nanoparticles by analytically solving Maxwell's equations.[37] Since then, the fundamental understanding of LSPR in nanoparticles has become significantly deeper and with the development of nanofabrication that allows production of nanoparticles with controlled shape and size, a plethora of applications has been demonstrated, especially in the last two decades. Among these applications are that LSPR can be utilized in optical waveguides,[38–40] to improve the resolution of microscopes,[41] as therapy agent in tumour treatment[42–44] and, of relevance here, as highly sensitive chemical and biological (nanoplasmonic) sensors.[45–51]

Expectedly, nanoplasmonic sensors have also found their way into hydrogen detection applications and, in fact, can be considered to constitute a major sub-field with a steadily growing community. A decade after the work by Langhammer et al., where optical hydrogen detection facilitated by Pd nanoparticles was demonstrated,[52] around 100 studies relating to nanoplasmonic hydrogen sensors have been published. The growing interest stems from the excellent potential shown by the sensors, whose key highlights include high sensitivity[53,54] possible miniaturization down to the single nanoparticle level[55–59] and fast response.[60,61] Furthermore, nanoplasmonic sensors also enjoy generic features of optical sensors, such as multiplexing capability, electrical passiveness, absence of electromagnetic interference and the possibility for remote sensing[15] Finally, typical nanoparticle preparation for nanoplasmonic

sensors promises scalable processing that is very important when real applications are considered.

With this proven excellence at hand, I have the utmost privilege and great excitement to work on nanoplasmonic sensors (and be creative in the process) in the pursuit of pushing the performance of hydrogen sensors by developing a platform that can satisfy all of the stringent performance requirements discussed above (*cf.* **Table 1.1**).

1.3 Gas Sensors for Environmental Sustainability

The overarching goal of the hydrogen economy is to create a sustainable environment through the use of hydrogen as a sustainable energy carrier. A loose definition of a sustainable environment used here is when our ecosystem (*i.e.* our lovely earth) is able to maintain its ability to provide its natural resources upon which we critically depend. Unfortunately, industrial revolution that began more than a century ago brought with it the release of unnatural amounts of polluting gases that disturb the balance of our environment. This is clearly reflected in global warming (caused specifically by the so-called greenhouse gases CO_2, CH_4, NO_2 and O_3) whose consequences includes *e.g.* rising sea levels and weather anomalies. In fact, global warming, along with the creation of a sustainable energy system, are two of society's grandest challenges in the 21st century.[62] Thus, in line with the goals behind the hydrogen economy, complementary action to monitor, control and finally reduce the emission of polluting gases is necessary. This creates a need for development of highly selective gas sensors for species beyond H_2, *i.e.* CO_2, CO, NO_2. Beyond the traditional purpose of simple "detection" of a species, a sensor can also serve as a means to assess characteristics of materials, for example how they "interact" with gas species. As a minor part of this thesis, I thus also explore the possibility of using nanoplasmonic sensors as an analytical tool to assess the CO_2 sorption properties of mesoporous materials.

1.3.1 Carbon Capture and Storage

Anthropogenic CO_2 emissions (*i.e.* the ones originating from human activity through *e.g.* fossil fuel combustion and industrial processes) constitute 65% of global greenhouse gases, and CO_2 has been pinned down as the gas most responsible for the global warming effect.[62,63] At the individual level, CO_2 pollution may cause an excessive amount of CO_2 in the blood, which typically results in a serious and sometimes fatal condition characterized by headache, nausea and visual disturbances.[64,65] Therefore, numerous mitigation strategies for CO_2 emission reduction are suggested or actively being applied. One particular direction is the *Carbon Capture and Storage (CCS)* scheme whose goal is to capture waste CO_2 from large point sources (*e.g.* fossil fuel power plants or concrete factories), transport it to a storage site and deposit it where it will not enter the atmosphere (or reuse it in a considerable amount for other industrial processes).

The successful deployment of CCS schemes requires close collaboration between different fields, ranging from politics to technology. One of the consequences of the increasing interest in CCS in the technological field is the accelerated search for *materials* that can capture CO_2. Numerous kinds of materials have been reported and used: *e.g.* (liquid) amines, metal oxides,

zeolites, metal-organic frameworks (MOFs) and polymers.[66–71] The last three of the mentioned examples belong to the class of mesoporous materials, which are attractive for CCS due to their very high specific surface area (the current record for the highest specific surface area for porous material is held by NU-109 and NU-110. Both belong to a class of MOF, whose surface area reaches 7000 m^2/g; that is, one kilogram of the material contains an internal surface area that could cover seven square kilometers![72]). However, despite the made progress in the field, the development of cheap, scalable and environmentally friendly CO_2 sorbents is still highly desired.

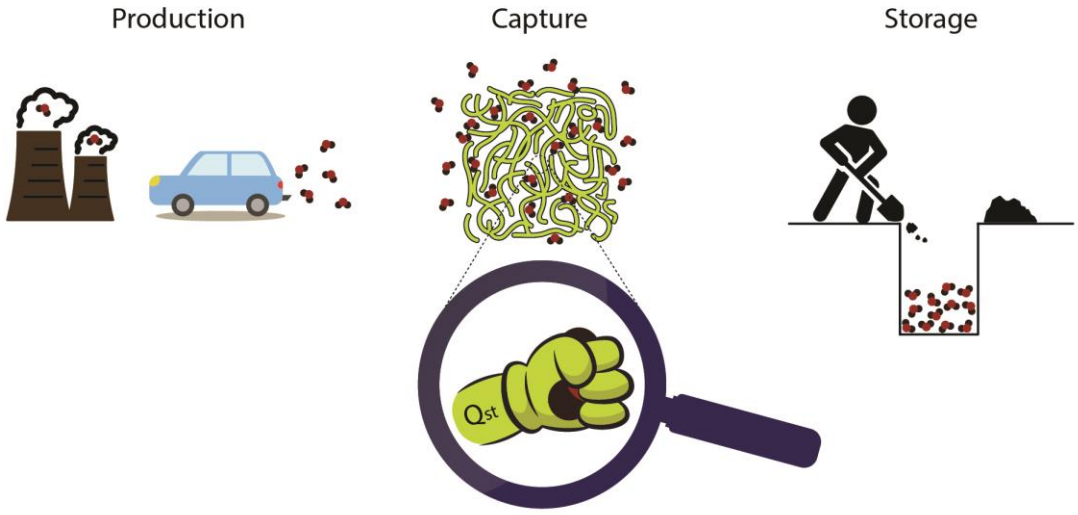

Figure 1.4. Carbon Capture and Storage. *Carbon Capture and Storage (CCS) is the process of capturing waste CO_2 from large point sources (e.g. fossil fuel power plant or concrete factory), transporting it to a storage site, and depositing it where it will not enter the atmosphere, normally an underground geological formation. One of the ways to capture the CO_2 is by utilizing sorbent materials that are able to selectively adsorb the CO_2 from gas mixtures. The interaction strength of CO_2 with the sorbent materials is expressed through the isosteric heat of adsorption (Q_{st}). Some of the icons used in the schematic are taken from a webpage.*[13]

Capture of CO_2 with these materials is based on the idea that CO_2 *selectively* adsorbs from gas mixtures and can be recovered as nearly pure CO_2 by cyclically increasing the temperature or decreasing the pressure.[66,73] For successful CO_2 capture (and release), the CO_2-adsorbent interaction strength should be engineered in an optimal way.[74] It should be strong enough so that CO_2 cannot easily escape at conditions characteristic for the environment from which it is to be removed (in other words, these conditions can vary greatly for specific applications) but also not too strong so that complete release can be achieved by mild heating to make the process energy efficient.

The interaction strength of CO_2 with a sorbent is typically assessed by measuring the *isosteric heat of adsorption* (Q_{st}) using various methods based on gravimetric and volumetric measurement principles. Gravimetric techniques are complicated by buoyancy and Knudsen

diffusion at low pressure, while volumetric techniques need accurate dead space volume determination for correction. Furthermore, both methods have a common requirement for accurate determination of sample initial weight and/or volume.[75] Additionally, porous polymer systems (as well as, *e.g.*, MOFs) potentially show swelling upon CO_2 adsorption, which further complicates their analysis.[76] Therefore it is very appealing to develop new experimental strategies for the scrutiny of CO_2 sorption processes in such materials. Ideally, the experimental methodology developed is generic, easy to use, accurate, and allows rapid characterization for efficient screening of new materials for CCS. Using indirect nanoplasmonic sensing, I demonstrate in **Paper VIII** that optical spectroscopy based on plasmonics is suitable for the aforementioned purposes.

1.4 This Thesis

This thesis comprises work related to *developing* and *establishing* nanoplasmonic materials and structures as hydrogen sensors. Specifically, in this thesis I introduce nanoalloys as a new class of transducing materials to be used in such sensors with the ambition that it can be the platform that is able to satisfy all of the hydrogen sensing metric requirements outlined in **Table 1.1**. In order to do so, the work undertaken in this thesis constitutes a coherent effort to reach this goal. At the heart of this effort is the first part of my work, where I demonstrate a bottom-up nanofabrication method to create alloy nanoparticle arrays for plasmonic applications in general, and for hydrogen sensing in particular (**Paper I**). Having established this base, and before taking the discussion to the level of the performance of alloy nanoparticles as hydrogen sensors, it was then of importance to establish the correlation between the generated optical signal of an alloy nanoplasmonic sensor and the hydrogen concentration inside the nanoparticles. Therefore, in **Paper II**, I scrutinize this correlation by establishing a combined gravimetric and optical experimental setup that enabled simultaneous measurement of the plasmonic response and the amount of hydrogen absorbed. In **Paper III** to **V** I demonstrate the use of alloy nanoparticles as hydrogen sensors and report their relevant sensing metrics for increasingly complex sensor configurations. Specifically, I use PdAu binary alloys in **Paper III**, PdCu and PdAuCu ternary alloys in **Paper IV** and finally in **Paper V**, I combine the PdAu alloy with different polymeric coating layers that serve as a molecular sieve to prevent sensor deactivation, as well as, as it turned out, significantly increase sensor response time. Finally, as an effort to further push the sensing platform closer to real applications, in **Paper VI** I try the idea of integrating the alloy nanoparticles on an optical fiber by pattern-transfer of lithographically made nanostructures from a flat host surface onto the fiber.

An almost inevitable consequence of working with alloys is the atomic segregation that may occur from the bulk to the alloy surface. Owing to high sensitivity of nanoplasmonic sensors, this process can actually be followed *directly* on the alloy nanoparticles I have developed, as demonstrated in **Paper VII** using PdAu alloy as the model system.

As a minor part of the thesis, I have also applied indirect nanoplasmonic sensing (INPS) to characterize the CO_2 adsorption energetics in a microporous solid sorbent material in **Paper VIII.** Specifically, we studied PIM-1,[77,78] a material that belongs to the rising class of microporous polymers that exhibit high CO_2 permeability and selectivity, which make them

attractive for Carbon Capture and Storage (CCS) applications.[79–81]

The organization of the remainder of this thesis is as follows: **Chapter 2** introduces the background physics to the LSPR phenomenon, with particular focus on the mechanisms through which metallic nanoparticles supporting LSPR can be utilized as sensors. **Chapter 3** discusses the basics of nanoalloys, including the surface segregation and their common production methods. **Chapter 4** provides an overview of metal hydride systems with particular focus on the phenomena relevant for the interpretation of the work presented in the thesis. It also includes a discussion about using metal hydrides as signal transducers in hydrogen sensors, with specific emphasis on nanoplasmonic sensors. **Chapter 5** describes the nanofabrication techniques that I have developed and employed to make my samples. **Chapter 6** explains the different characterization methods I have used to assess the fabricated structures and sensors. Finally, **Chapter 7** summarizes the main results obtained in the appended papers, and I also present a short outlook.

2 Nanoplasmonics

The field of nanoplasmonics, which explores localized surface plasmon resonance phenomena in noble metal nanoparticles, has been rapidly developing for about two decades. In simplest terms, a plasmon resonance is a *coherent collective oscillation* of the free electrons in a metal. In the particle analogy it can be understood as the quantum of the plasma oscillation (thus the –*on* suffix in plasmon). I believe this summary may not be sufficient for most of the readers and so this Chapter is written to briefly introduce the field of plasmonics and the concept of the localized surface plasmonic resonance. Furthermore, a well-developed application of localized plasmons, their use in sensors – the central topic of this thesis, will also be addressed.

2.1 Electrons in a Metal

In order to understand the optical properties of materials one should, at the beginning, refer to an approach developed by Hendrik Lorentz[82,83] to explain how electrons in a metal behave under the influence of an external electric field. In his model, better known as the *Lorentz Model*, the optical properties of a material is described in terms of the response of a classic harmonic oscillator to an external driving force. Electrons of matter are considered to be a collection of identical, independent, isotropic harmonic oscillators oscillating back and forth around their equilibrium position, *i.e.* the positively charged cores of the atom in the lattice of the solid. When an external electric field $\boldsymbol{E(x,t)}$ acts upon these oscillators they follow the equation of motion

$$m_e\ddot{\boldsymbol{x}} + m_e\Gamma\dot{\boldsymbol{x}} + k\boldsymbol{x} = -e\boldsymbol{E}(\boldsymbol{x},t) \tag{2.1}$$

where m_e is the mass of the electron, $\boldsymbol{x}$ is the displacement from equilibrium, Γ is the damping constant, k is the spring constant of the harmonic oscillator and e is the electronic charge. If the applied field is harmonic with frequency ω and the oscillation amplitude is small so that the field is approximately spatially constant, equation 2.1 has a single solution describing the induced dipole of a single oscillating electron as

$$\boldsymbol{p} = -e\boldsymbol{x} = \frac{\frac{e^2}{m_e}}{{\omega_0}^2-\omega^2-i\Gamma\omega}\boldsymbol{E} \tag{2.2}$$

where ω_0 is the resonance frequency of the oscillator defined as

$$\omega_0 = \sqrt{\frac{k}{m_e}} \tag{2.3}$$

Assuming a system consisting of a large number, *N*, of independent electrons, the polarization $\boldsymbol{P}$ (dipole moment per unit volume) can be calculated by multiplying *N* with equation 2.2. By using the constitutive relation[82]

$$\boldsymbol{P} = \varepsilon_0(\varepsilon - 1)\boldsymbol{E} \tag{2.4}$$

A complex dielectric function $\varepsilon(\omega)$ for a system with a large numbers of independent electrons can then be defined as

$$\varepsilon(\omega) = 1 + \frac{{\omega_P}^2}{{\omega_0}^2 - \omega^2 - i\Gamma\omega} = \left(1 + \frac{{\omega_P}^2({\omega_0}^2 - \omega^2)}{({\omega_0}^2 - \omega^2)^2 + \Gamma^2\omega^2}\right) + i\frac{{\omega_P}^2\Gamma\omega}{({\omega_0}^2 - \omega^2)^2 + \Gamma^2\omega^2} \tag{2.5}$$

The resonance frequency, ω_0, originates from the restoring force experienced by an electron bound to an atom while the damping constant, Γ, quantifies the associate inelastic processes, and lastly the plasma frequency, ω_P, is

$$\omega_P = \sqrt{\frac{Ne^2}{m_e\varepsilon_0}} \tag{2.6}$$

For an electric field with frequency $\omega < \omega_p$ the electrons will follow it and the dielectric function ε is complex (*i.e.* has a real and imaginary part, see equation 2.5). Within the metal, the field decays exponentially with the distance from the metal-dielectric interface. Therefore, the incident field is attenuated and the electromagnetic field is reflected back from the surface. If the opposite situation of $\omega > \omega_p$ occurs, the electrons inside the metal cannot respond fast enough to screen the electric field. The refractive index ε is then real and the metal behaves as a dielectric material *i.e.* the optical field is partly refracted and partly reflected. The bulk plasma frequencies of metals are located in the ultraviolet spectral range, and thus the condition of $\omega < \omega_p$ is fulfilled at the visible frequencies. This explains why metal surfaces appear shiny and reflective to the human eye.

2.2 Localized Surface Plasmon Resonance

When a metal entity becomes smaller and comparable to the wavelength of near-visible light, its optical properties change dramatically. Under this circumstance the free electrons of the particle can oscillate *collectively* when excited by the external optical electromagnetic field with appropriate frequency. The oscillation typically decays within few femtoseconds due to the significant damping (imaginary part of ε) characteristic for metals. The displaced electrons (together with the rigid positively charged atomic cores) create a polarization field of their own, which drives them back towards the equilibrium position. Due to the inertia, overshoot occurs even in the absence of the external field. When the frequency of the applied field matches with the system's eigenfrequency, a collective coherent resonance occurs. The size of the nanoparticle also imposes a boundary condition that prohibits the formation of a propagating longitudinal charge density wave, *i.e.* like in the case of bulk and surface plasmon resonance. Instead, in a simple picture, a standing electron wave oscillation with respect to the atomic core is accomplished. Hence the name *localized surface plasmon resonance* (*LSPR*).

LSPR is one of the best examples of how things may change significantly at the nanoscale. At the LSPR frequency, metal particles effectively scatter and absorb light, which gives rise to a strong peak in their light extinction (*i.e.* sum of scattering and absorption) spectrum, which later defines the "color" of the particles. Furthermore, the charge separation at the particle surface gives rise to a strong electric field close to the surface. **Figure 2.1** shows a schematic illustration of the collective motion of the free electrons under the applied field. It corresponds to an oscillating time-dependent electric dipole, which gives rise to an induced electric field due to the charge separation. Two higher order modes of the LSPR, which may play a role for bigger particles, are also shown.

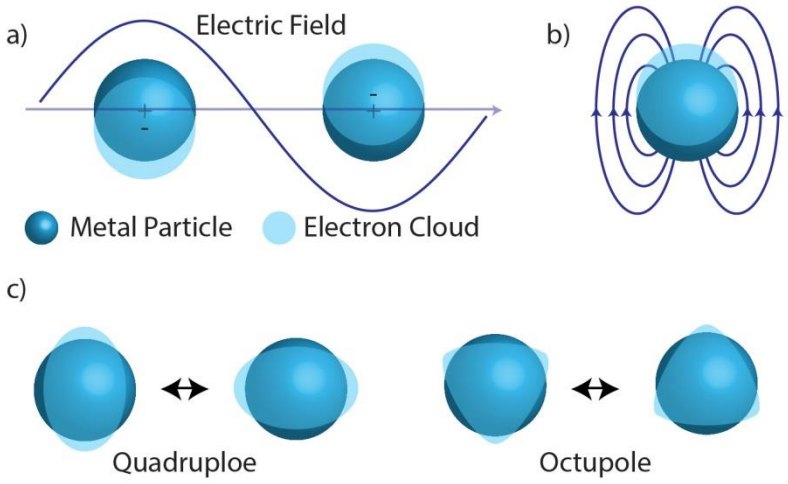

Figure 2.1. Schematic illustration of localized surface plasmon resonance in a small metal sphere. *(a) The external electromagnetic field created by irradiated light drives the electrons of the nanoparticle out of their equilibrium positions relative to the positively charged atomic cores. The free electrons oscillate collectively with largest amplitude when the light frequency matches their resonance or eigenfrequency. (b) Due to the oscillating charges, which lead to a polarization of charge on the surface of the nanoparticle, a strong electric field is developed in the vicinity of the particle. (c) For larger nanoparticles (relative to the wavelength), higher modes of the LSPR exist, for example quadrupole and octupole modes.*

LSPRs can typically be excited in the ultraviolet (UV), visible, and near infra-red (NIR) range of the electromagnetic spectrum. The excitation represents a time-dependent dipole that generates a strong local field, which is superimposed on the external field that drives the oscillation. Thus, due to the resonant nature of the excitation, the local field around the nanoparticles (near-field) is *enhanced*. This field can act as a *probe* of the nanoparticles' surrounding and makes the LSPR very sensitive to changes of the permittivity of the medium in the vicinity of the particle, as *e.g.* induced by molecular adsorption on the particle surface. Higher refractive index of the surrounding means higher polarizability, which in turn increases the screening of the dipolar field of the LSPR. The increased screening dampens the electron oscillation and, thus, decreases its energy (spectrally red-shifts the resonance, *i.e.* moves it towards longer wavelength). The plasmon energy is one key parameter in the characterization

of LSPR, and it is also commonly used as the main readout in sensing applications.[31,45,84] A detailed explanation of the sensing applications based on LSPR will be given in **Section 2.3**.

The lifetime of a typical LSPR excitation is in the range of 5-25 femtoseconds, depending on particle size, shape and material. There are two ways in which LSPR can be damped: radiatively and non-radiatively. The radiative damping process occurs when a photon of the same energy as the incident one is re-emitted from the particle.[85,86] Light that decays radiatively thus corresponds to an elastic scattering process of electromagnetic energy by the induced dipole and is referred to as *scattering*. The second damping process, non-radiative, involves dissipation either via electron-hole pair excitation (from below to above the Fermi level, also called as Landau damping) and, ultimately, production of heat through electron-phonon coupling.[85,86] Light that decays non-radiatively is referred to as being *absorbed* by the nanoparticle. Additionally, existence of adsorbates on the surface of the nanoparticle may also contribute to plasmon damping. This effect is commonly referred as chemical interface damping.[83]

The sum of absorption and scattering is called optical *extinction*, which corresponds to the total attenuation of the electromagnetic wave as it traverses a particle. The efficiency of the two decay mechanisms can be expressed through their respective cross-sections (*i.e.* how efficient the processes are). The analytical expressions for absorption, scattering, and extinction cross sections of a nanoplasmonic particle much smaller than the wavelength are[82]

$$\sigma_{abs} = k\mathrm{Im}(\alpha) \tag{2.7}$$

$$\sigma_{sca} = \frac{k^4}{6\pi}|\alpha|^2 \tag{2.8}$$

$$\sigma_{ext} = \sigma_{abs} + \sigma_{sca} \tag{2.9}$$

where α is the material polarizability (see below) and k is the wave vector.

The extinction cross section offers a convenient way to describe the interaction between light and nanoparticles. For a non-transparent object that does not resonantly interact with the electromagnetic field, the extinction cross section is equal to the projected geometric area of the particle and independent of the wavelength, *i.e.* only the light directly impinging on the particle will not be transmitted. For the case of strongly interacting particles, the extinction cross section depends on the wavelength and can be significantly larger than the projected geometric area of the particle. This is the reason why plasmonic nanoparticles appear colored (see *e.g.* Lycurgus Cup in **Chapter 1**). When white light hits the particles, a (major) part of the wavelengths of the incident light is attenuated, leaving the rest of the wavelengths transmitted, hence creating the "colored" appearance of the cup.

2.2.1 Understanding LSPR: The Electrostatic Approximation

A simple way to understand LSPR is the electrostatic approximation in the so-called quasi-static regime. This model considers the particle diameter D to be small compared to the wavelength of light ($D << \lambda$). This means that, in a first approximation, the electron oscillation

of the plasmon can be modeled as a point electric dipole. The mathematical form can be constructed if one considers a homogeneous, isotropic nanosphere placed in an arbitrary medium and subjected to a time-dependent external field $\boldsymbol{E_0}e^{-i\omega t}$. The induced local field of the particle then superimposes with the applied field, creating a dipole moment that can be described as

$$\boldsymbol{P}(\omega) = \varepsilon_d \alpha(\omega) \boldsymbol{E_0} e^{-i\omega t} \tag{2.10}$$

where ε_d is the dielectric constant of the surrounding medium and $\alpha(\omega)$ is the dipole polarizability of the nanosphere. Gustav Mie, a German physicist, presented the exact solution of the light-metal nanoparticle interaction by solving Maxwell's equation more than a century ago.[37] According to his work, famously known as Mie Theory, the polarizability $\alpha(\omega)$ of the nanosphere reads as

$$\alpha(\omega) = 4\pi \left(\frac{D}{2}\right)^3 \frac{\varepsilon_m(\omega) - \varepsilon_d}{\varepsilon_m(\omega) + 2\varepsilon_d} \tag{2.11}$$

where $\varepsilon_m(\omega)$ is the complex dielectric function of the nanosphere material. The magnetic permeabilities are assumed to be as in vacuum for both the sphere and the external medium; a reasonable assumption for optical frequencies.[83] Equation 2.11 shows that the polarization becomes very large when the denominator is equal to zero (at resonance), *i.e.* $\varepsilon_m(\omega) = -2\varepsilon_d$. This condition requires the dielectric constant of the particles to have a negative real part $\varepsilon_1(\omega)$ and, preferably, a small imaginary part $\varepsilon_2(\omega)$ (*i.e.* small losses) for a strong polarization to occur. Inserting the Drude dielectric function into the expression for the dipole polarizability (equation 2.11) yields

$$\alpha(\omega) \approx 4\pi \left(\frac{D}{2}\right)^3 \frac{{\omega^2}_{LSPR}}{{\omega^2}_{LSPR} - \omega^2 - i\Gamma\omega} \tag{2.12}$$

where

$$\omega_{LSPR} = \frac{\omega_P}{\sqrt{1+2\varepsilon_d}} \tag{2.13}$$

or, if we use wavelength instead of frequency as we commonly do in measurements:

$$\lambda_{LSPR} = \lambda_p \sqrt{1 + 2\varepsilon_d} \tag{2.14}$$

where λ_{LSPR} is the localized surface plasmon wavelength. The λ_{LSPR} is generally larger than the wavelength of the bulk plasmon, λ_p. Equation 2.14 indicates that the spectral position of the LSPR in the quasi-static limit depends purely on the surrounding dielectrics (*i.e.* ε_d) and the material itself (reflected through λ_p). However this is not entirely true since for very small particles (< 10 nm) the dielectric function of the metal is size-dependent. For larger particles, size-dependent retardation effects also influence the LSPR spectral position.[83] These effects will be explained in the next section.

One can also insert the dipole polarizability (equation 2.11) into the expressions of scattering and absorption cross sections (equation 2.7 and 2.8). This yields

$$\sigma_{abs} = k\mathrm{Im}(\alpha) = 4\pi k \left(\frac{D}{2}\right)^3 \mathrm{Im}\left(\frac{\varepsilon_m(\omega)-\varepsilon_d}{\varepsilon_m(\omega)+2\varepsilon_d}\right) \quad (2.15)$$

$$\sigma_{sca} = \frac{k^4}{6\pi}|\alpha|^2 = 8\pi \left(\frac{D}{2}\right)^6 k^4 \left(\frac{\varepsilon_m(\omega)-\varepsilon_d}{\varepsilon_m(\omega)+2\varepsilon_d}\right)^2 \quad (2.16)$$

Thus, the absorption is proportional to the sphere volume (D^3) while scattering is proportional to the square of the volume (D^6). Thus, for very small particles, absorption dominates, while scattering dominates LSPR decay for larger particles. For example in gold nanospheres and nanodisks, this transition occurs for particle diameters around 80 nm and 100 nm,[87,88] respectively. An example of an extinction spectrum (that is, the sum of absorption and scattering) for an array of plasmonic nanodisks fabricated by hole-mask colloidal lithography (explained in **Chapter 5**) is plotted in **Figure 2.2**.

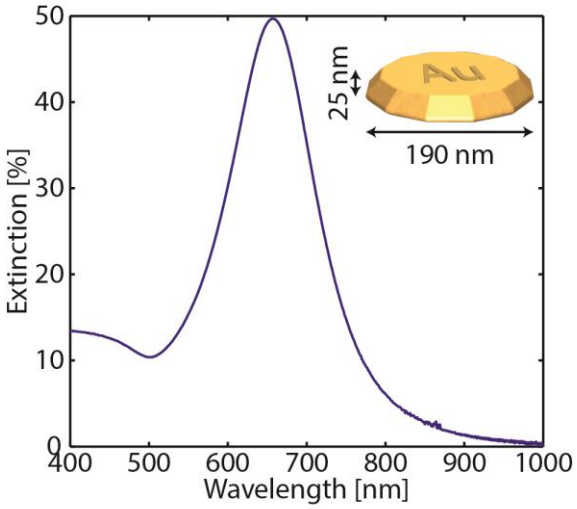

Figure 2.2. Extinction spectrum of a gold nanoparticle array. *A quasi-random array of gold nanodisks with diameter of 190 nm and height of 25 nm, fabricated by hole-mask colloidal lithography (HCL) on glass features a peak-like extinction spectrum. LSPR gives rise to a strong extinction peak due to efficient scattering and absorption by the gold nanoparticles around 650 nm. This particular extinction spectrum corresponds to a bluish color of the nanoparticles.*

2.2.2 LSPR Dependence on Particle Size, Shape and Composition

The discussion of the LSPR phenomenon in **Section 2.2.1** was entirely based on the spherical particle approximation in the quasi-static regime, which is sufficient to give a basic idea about LSPR. However, in reality, various shapes and sizes of nanoparticles can be fabricated and are used for real applications. Therefore, since the polarizability of differently shaped particles is not the same as for a sphere, the scattering and absorption characteristics of such particles are different. It is thus essential to have extended models and approaches to explain the plasmonic

properties of more complex nanostructures. By knowing the factors defining the LSPR, one can freely "design" the resonance to be most suitable for a specific application. Below a short discussion of the role of size/shape and material composition of the nanoparticle on the LSPR is presented.

For a particle larger than the quasi-static approximation range (*i.e.* where $D << \lambda$ no longer applies), retardation effects and radiation damping become very important. Retardation of the applied field arises when the particle size is comparable to the wavelength and the field distribution is no longer homogeneous over the entire particle. A second retardation effect affects the field inside the particle since it takes time for the dipolar field to spread over the particle due to the finite speed of light. This retards the formation of the dipole and leads to a phase shift between the dipolar plasmonic and the exciting field of the irradiated light wave. These retardation effects induce a spectral red shift of the plasmon resonance, as well as peak broadening.[89]

Radiation damping originates from the energy loss of the time-dependent dipole via emission of radiation. This radiative plasmon decay channel thus becomes rapidly more significant for bigger particles since the dipole is proportional to the size of the nanoparticles, and the scattering cross section scales with D^6 (see equation 2.8). Radiation damping also introduces a spectral red-shift, an increase in plasmon line-width and a decrease in the resonance intensity.[90] Larger nanoparticles also feature multipolar modes (see **Figure 2.1**c for the case of nanosphere particles), which means that the resonance band splits into several peaks which appear at shorter wavelength than the dipolar peak in the extinction spectrum.[91]

When addressing the material-dependence of LSPR, let us recall that a plasmon is an electron-based phenomenon. Thus, its properties strongly depend on the electronic structure (as described by the complex dielectric function) of the system within which it is excited. Theoretically, LSPR excitations are possible in any material possessing large negative real part and small imaginary part of the dielectric function. In fact, recent years have seen the emergence of non-metal plasmonics *e.g.* dielectrics[92] and semiconductors.[93–95] Gold and silver are the "classic" nanoplasmonic materials since they are the main systems chosen in LSPR studies due to their low losses in the visible frequency range. Hence, they exhibit strong and reasonably narrow LSPR peaks (**Figure 2.2**). Moreover, they feature LSPR in the visible range and their properties can be reasonably well explained by the Drude model in the vis-NIR range, *i.e.* below the interband transition threshold (2.4 eV for gold and 3.8 eV for silver, respectively[96]).

However, with increasing interest in LSPR and demands for applications in various fields, an increasing number of materials have been studied for their plasmonic properties. Thus, experimental reports on LSPR in, to name a few, Pt, Pd, Cu, Ni, Sn, Y, Mg and Al have become available.[97–105] Furthermore, alloys have also been considered for plasmonics, however only to a very limited extent.[106–109] For example, it has been shown for AuAg alloy nanoparticles that their LSPRs can be tuned to anywhere between that for pure Au nanoparticles to that of Ag nanoparticles by adjusting the alloy composition (also see **Figure 2.3**).[110–112] LSPR characteristics of some other alloy systems have also been demonstrated (*e.g.* AuCu[108,113] and AuFe[107]), however, only in a very limited fashion due to lack of versatile and reliable methods

for fabricating alloy nanoparticles. Lastly, a phase transformation of a material can also induce significant changes to LSPR since the transition changes the electronic structure and/or volume of the nanoparticles significantly. A prominent example, which also is relevant for this thesis, is Pd when it is absorbing hydrogen (and thus phase-transforms to palladium hydride PdHx), which leads to a considerable change in its electronic density of states due to weakened interactions between Pd atoms induced by interstitial hydrogen.[114,115]

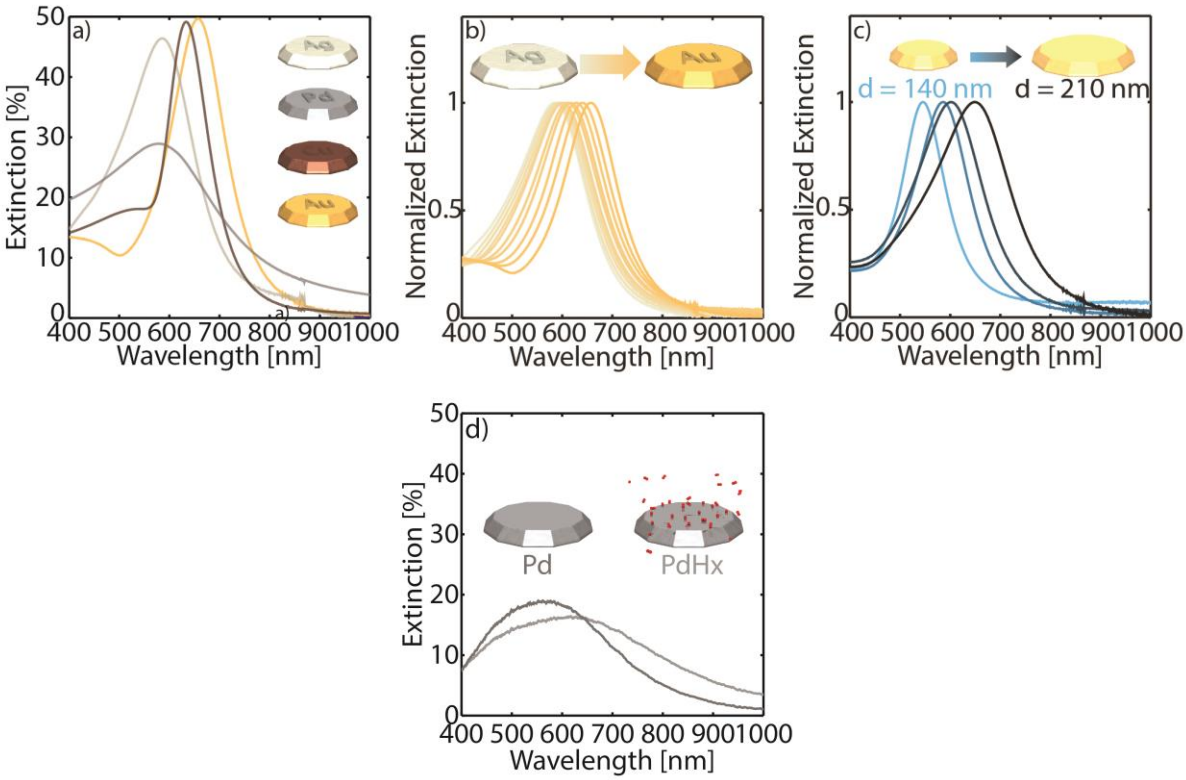

Figure 2.3. The LSPR dependence on material composition and particle dimensions. *(a) The different LSPRs exhibited by pure Ag, Pd, Cu and Au nanodisk arrays with dimensions of 190 nm diameter and 25 nm height. Note that the LSPR of Pd is much weaker and broader compared to the rest. (b) The evolution of LSPR for AuAg alloy nanodisks with different compositions (Au from 0–100 at. %, in 10 at. % steps). The dimensions are 190 nm diameter and 25 nm height. (c) The change in LSPR in 50:50 AuAg alloy nanodisks with increasing diameter of 140 nm, 170 nm, 190 nm and 210 nm. The thicknesses are kept constant at 25 nm. (d) The change in LSPR of Pd nanodisks with dimension of 190 nm diameter and 25 nm height when exposed to hydrogen, resulting in palladium hydride, PdHx formation. Note that in panel (b) and (c) extinction is normalized.*

In addition to particle size and material, the optical properties of plasmonic nanoparticles are also greatly influenced by their shape due to the polarizability's, $\alpha(\omega)$, shape dependency. Many works have been devoted to study the shape-LSPR relation both experimentally and theoretically. One of the fundamental works was done by Mock et al. in which they studied the spectra of silver nanoparticles with different shapes (spheres, triangles, and cubes) but similar

volume.[116] The study concluded that structures with shaper features have higher refractive index sensitivity (*i.e.* sensitivity towards the change in surrounding permittivity). The result was also supported by similar finding in other reports.[117,118] In general, the deviation from spherical shape shifts the resonance towards longer wavelength due to higher concentration of charge and electric field at the sharp features.[119,120] Apart from the general shape of the particles, aspect ratio (*i.e.* ratio of width to height) also affects the resonance. High aspect ratio structures (towards a one-dimensional structure) have longer resonance wavelength and higher LSPR intensity.[119,121] The reason for this is the high charge accumulation in such structures, which leads to higher restoring force and consequently longer resonant wavelength. **Figure 2.3** showcases the wide tunability of LSPRs achieved in this thesis by changing the plasmonic elements' composition (through change of materials, alloying and phase transition) and dimension.

2.3 LSPR Sensors

The LSPRs of nanoparticles are strongly dependent on many factors, as discussed in previous sections, *i.e.* shape,[116] size,[122] material[98] and the dielectric function of the surrounding environment.[123] Using the fact that the refractive index, *n*, of a material is related to its dielectric function through $\varepsilon_d = n^2$, equation 2.14 can be written as

$$\lambda_{LSPR} = \lambda_p \sqrt{1 + 2n^2} \qquad (2.17)$$

We see that the spectral position of the LSPR (λ_{LSPR}) depends approximately linearly on the refractive index of the surrounding medium. This sensitivity, caused by the existence of the enhanced field in the vicinity of the plasmonic nanoparticles, makes it possible for LSPR to be used as a *sensor*; a nanoplasmonic sensor. The enhanced field can be considered to act as a *nanoscale probe* of events taking place very closely to the plasmonic particle surface, within the volume of enhanced field. This constitutes a highly localized *sensing volume* that allows one to observe any change (*e.g.* adsorbate interaction, phase transition, etc.) occurring near the particle surface if such a change results in a modification of the local refractive index. **Figure 2.4** schematically illustrates the sensing volume for the case of a nanodisk in vacuum.

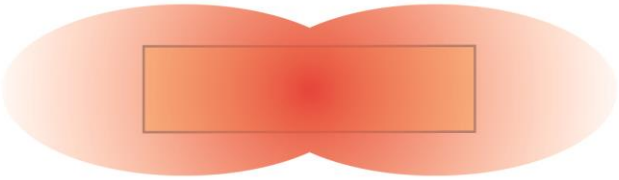

Figure 2.4. A simplified illustration of the sensing volume around a plasmonic nanodisk in vacuum. *The sensing volume (red areas) is created by the enhanced electromagnetic field surrounding a plasmonic entity. Within it, local permittivity changes are detected as a spectral shift of the plasmonic peak.*

The use of a nanoplasmonic sensor to detect changes in the surrounding was first done exactly 20 years ago by Englebienne,[124] who employed Au nanoparticles to detect the occurrence of

antigen binding to ligands attached to the nanoparticles. By following the λ_{LSPR}, the binding process could be followed in real time. **Figure 2.5** illustrates how an LSPR sensor detects the binding of analyte molecules onto the particle. The presence of analytes increases locally the refractive index, which in turn alters the resonance condition of LSPR, causing it to red-shift.

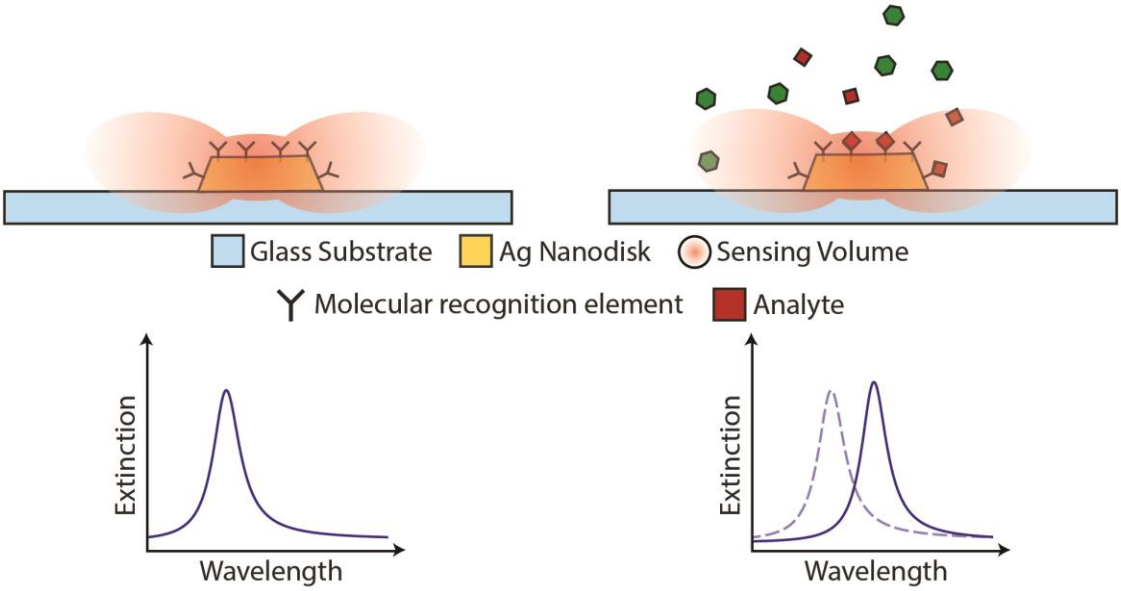

Figure 2.5. Schematic illustration of an LSPR-based local refractive index sensor. *Analyte binding leads locally to higher refractive index in the vicinity of the nanoparticle. The increase in the refractive index is detected as a red-shift of the nanoparticle LSPR. The figure is adapted with modification from ref. 125.*

Figure 2.6 shows the three typical "fingerprints" of LSPR that all can be used as readout parameter in a nanoplasmonic sensing experiment, (i) a change in peak position, λ_{peak}, (ii) extinction at peak (*Ext @ Peak*), and (iii) full width at half maximum, *FWHM*. They all have in common that they are the descriptor of a "physically meaningful" change of the LSPR effect. As described above, λ_{peak} is correlated with the resonance frequency. Furthermore, Ext @ Peak corresponds to the extinction cross section and the FWHM is characteristic for the damping of the LSPR. Most often, all three readouts change simultaneously. However, one cannot say in general which one of these readouts gives the "best result" since they might be more sensitive to different aspects of the sensed process and thus relate to different phenomena. Therefore, the readout parameter should be chosen carefully in order to get as good and as physically relevant signal as possible for the particular system studied. At the same time, the combination of different readout parameters may also provide deeper insight into the studied process at hand, compared to looking at one parameter alone.[126]

The simple yet powerful concept of nanoplasmonic sensing has made it a widely used analysis technique across different fields. So far, biosensors is by far the most exploited application area of nanoplasmonic sensing since it is label-free; thus it is very suitable for biological and biomedical assays.[45,127,128] Ever since the first demonstration by Englebienne,[124] numerous prototypes of LSPR refractive index sensors have been used to detect biological interactions

including, but not limited to, DNA-DNA,[129] carbohydrate-protein,[130,131] lipid-protein,[132] and protein-ligand binding.[133–135] Over the years, a tremendous diversification of applications of nanoplasmonic sensing has taken place. A prominent example is the growing application of nanoplasmonic sensing in catalysis[48,136] and chemical sensing.[49] In the field of catalysis, after a seminal work by Novo et al.,[46] nanoplasmonic sensing has shed light on different catalytic process such as photocatalysis,[137,138] metal-hydrogen interactions,[56,57] redox reactions[139] and spillover effects.[140] For chemical sensing, especially for the gas phase, nanoplasmonic sensing has been explored to detect, just to name a few, CO,[141,142] CO_2[50,51] and H_2.[52,143,144]

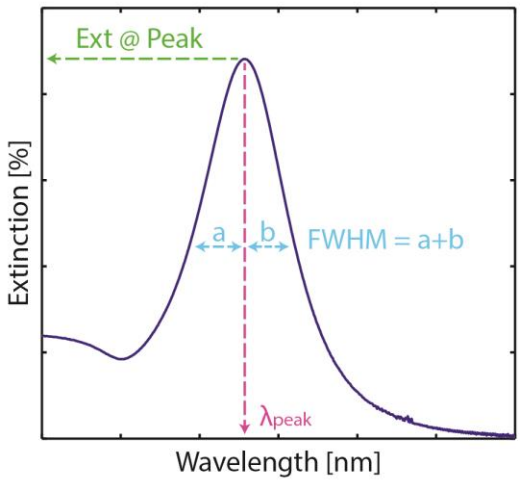

Figure 2.6. The "fingerprints" of LSPR. *The LSPR extinction peak can be characterized by three physically relevant parameters: λ_{peak} (red arrow) denotes the wavelength where the peak occurs and thus denotes the resonance frequency of the plasmon. Extinction @ Peak (green arrow) shows the extinction value at λ_{peak} and denotes the extinction cross section. Lastly, the full width at half maximum (FWHM), depicted by the blue dashed line, characterizes the width of the peak taken at half of the maximum extinction value and corresponds to the lifetime of the plasmon in energy space. It is also common to define FWHM as twice the length of the fraction of the line-width taken from the high energy (HE) and low energy (LE) side to the λ_{peak}, as marked by a and b respectively. Thus $FWHM_{LE} = 2b$ and $FWHM_{HE} = 2a$. $FWHM_{LE}$ is mainly used to avoid convolution with e.g. higher-order plasmonic modes.*

The growing number of applications of nanoplasmonic sensors proves their versatility, which indeed is one of their greatest strengths. One reason is that the strong dependence of the LSPR frequency on size, shape and permittivity of the local surrounding offers practically viable possibilities to actively tune the sensor response to a wavelength of choice by engineering these parameters during the fabrication of the nanoparticles. This feature paired with ultra-high sensitivity makes it possible that very small amounts of analyte (even single molecules[45,145]) or even the tiniest changes in the sensor environment are enough to trigger the plasmonic signal. That said, the quest for "ultimate sensitivity" is still ongoing and many different nanoparticle designs have already been investigated.[31,47] This ranges from the simpler shapes, like spheres[56] and disks,[146,147] to more complicated ones, like rings,[33] cubes,[148,149] stars[150], rice[53,54] etc.

Versatility is paired with additional advantages of nanoplasmonic sensing. For example, the method provides *in situ* measurement compatibility even in harsh environments, real-time and remote readout, and the possibility of massive miniaturization and parallelization. The miniaturization can be forced down to single nanoparticles because even single plasmonic nanoparticles can be used as signal transducers in sensing experiments.[55,56,58,59,145,151,152] The parallelization opportunities come as a consequence of the small size of the signal transducer in nanoplasmonic sensors. A very large number of nanoparticles can be placed on the surface of the sensor chip and each and every one of them can, in principle, be tailored to *e.g.* specifically detect one type of molecule only. These extraordinary properties of nanoplasmonic sensors are universal. Thus, one can take advantage of their abilities and apply them in many different fields, as briefly discussed above.

As any technique, LSPR sensing also has its drawbacks and it is important to be aware of them. One of the main limitations is a direct consequence of one of the main advantages: the high sensitivity. In combination with the non-specificity of the readout (*i.e.* what is measured is a "shift" of a peak), this may lead to data which are complicated to interpret since different processes occurring simultaneously with/in the vicinity of the plasmonic particle all will give rise to a signal. As a consequence, it is very important to design experiments properly so that, ideally, conditions during measurement are such that the measured plasmonic signal originates entirely from the event of interest. Failing to do so results in the convolution of different signals.

As one ingredient for minimizing this problem, gold (and silver, which, however, easily oxidizes) is mainly used as plasmonic nanoparticle in sensing applications since it is, within certain bounds, non-reactive. Thus the possibility of signal stemming from changes of the plasmonic nanoparticles themselves, *i.e.* oxidation, reaction with adsorbate or alloying with other metals, is minimized (though, when intended, this change of the nanoparticles themselves can serve as powerful sensing method, as discussed in the next section). Such effects can otherwise cause severe problems when measuring at elevated temperatures. Hence, in order to use LSPR sensors in more dynamic (*i.e.* under reactive gases and/or elevated temperature) environment, and thus broaden the applicability of LSPR sensors and make them more universal, these limitations must be overcome. Interestingly, one simple alternative has been developed in order to tackle some of those limitations and it will be discussed in a section below.

2.3.1 Direct Nanoplasmonic Sensing

If we recall the discussion above, especially equation 2.17, it is clear that λ_{LSPR} of nanoplasmonic particles depends on their actual state, and thus can be used to study changes in their own intrinsic properties (*i.e.* shape, size, and material of the particles). Thus, any alteration to the plasmonic particles themselves, either physically (*e.g.* shape and size) or chemically (*i.e.* phase change like oxidation, melting, hydride formation, etc.), affects the LSPR spectra, which means that such processes can be qualitatively (and quantitatively) observed by monitoring the corresponding changes in the LSPR spectra (**Figure 2.7**). The approach where the LSPR of the nanoparticle itself is used to monitor changes to the particle is usually called *direct plasmonic sensing* and was coined by our group.[48] In the past few years, this type of sensing has expanded

the applicability of plasmonic sensing to the field of materials science. Examples of such studies include the hydride formation in palladium,[52,56,57,59,153] magnesium,[105] and yttrium nanoparticles,[100] oxidation of aluminum[104] and copper nanoparticles,[102,154] freezing/melting of tin nanoparticles[101] and dealloying of AuAg alloy nanoparticles.[155]

Even though direct nanoplasmonic sensing has facilitated many interesting insights and thus is proven very useful, it is only limited to materials which themselves sustain LSPR. This greatly limits the materials and particle sizes available for study. As one of the ways to circumvent this problem, indirect nanoplasmonic sensing has been proposed.

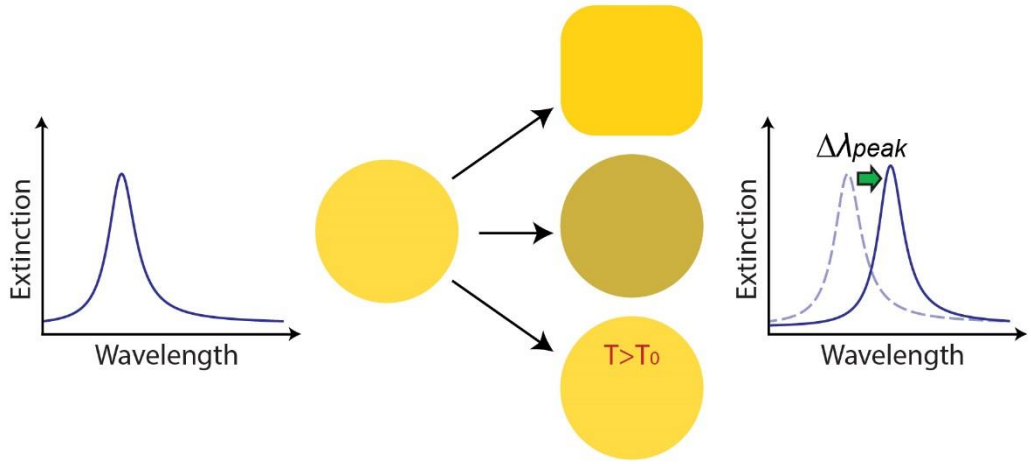

Figure 2.7. Direct plasmonic sensing. *Change in a plasmonic nanoparticle induces a modification of the optical properties and thus can be followed by tracking the λ_{peak}. The change may include shape, phase (e.g. oxidation, hydride formation) and temperature.*

2.3.2 Indirect Nanoplasmonic Sensing (INPS)

A specific type of LSPR sensing is called Indirect Nanoplasmonic Sensing (INPS).[147] The key feature of the method is the use of thin dielectric layers, which can be deposited by either sputtering or chemical vapor deposition (CVD) methods (detailed explanation in **Chapter 5**). In INPS, such layers are applied to cover an array of plasmonic (usually Au or Ag) nanoparticles in order to separate the optically active sensor particles from the materials of interest, which are simply deposited on top of the dielectric layer. Therefore, the active plasmonic nanoparticles are physically separated from and do not interact with the materials deposited onto the dielectric layer; thus the name *indirect* sensing. Despite the separation, the sensing functionality is still accessible since the enhanced LSPR field penetrates through the dielectric layer, which typically is only a few to ten nanometers thin. **Figure 2.8** shows a schematic depiction of the architecture of the INPS platform and its sensing principle.

This simple addition of a dielectric layer provides an efficient solution to some of the LSPR sensor shortcomings described above. For example, it is able to contain the shape of the gold nanodisks even at high temperatures, and prevents contamination, alloying, or reaction of the gold nanodisks with the materials being deposited on the sensor. Furthermore, the spacer layer can provide a tailored and homogeneous surface chemistry of the INPS sensor chip for a specific

experiment, where it either can constitute an inert substrate for the nano- or thin film materials to be studied or participate actively in the process under study (**Figure 2.8**).

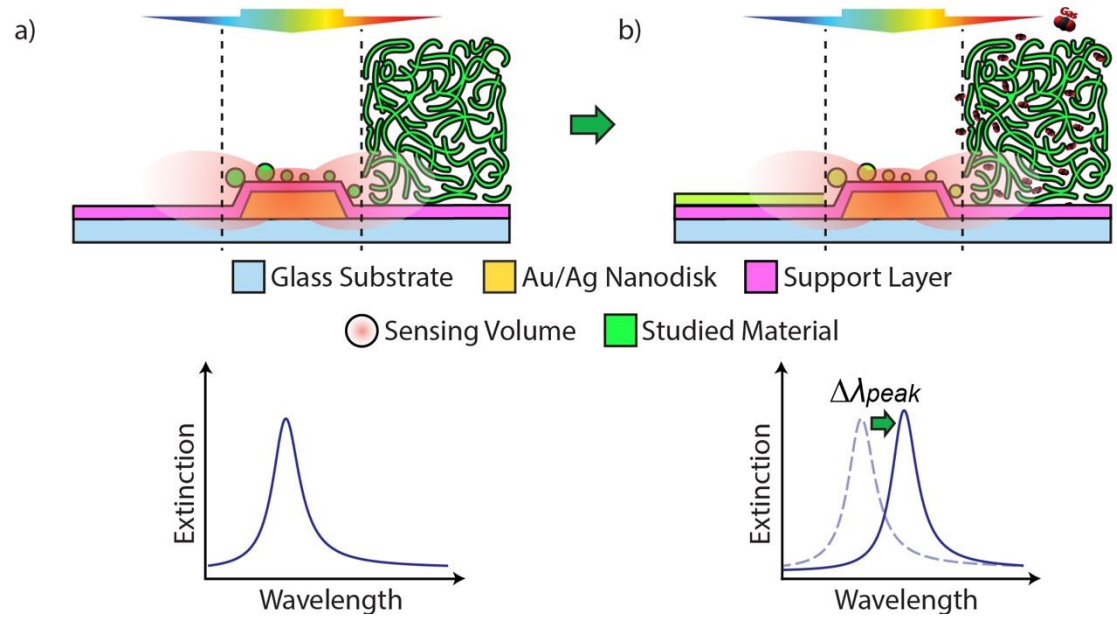

Figure 2.8. Nanoarchitecture and sensing principle of indirect nanoplasmonic sensing. *A thin dielectric layer is deposited on the plasmonic (e.g. Au or Ag) nanoparticle sensors to physically separate them from the nanomaterials to be studied. The latter can be small nanoparticles or thin films (solid or porous) and are simply deposited on top of the dielectric layer. Any change to the studied materials located within the sensing volume of the plasmonic nanoparticles (e.g. phase transition, adsorption of molecules/materials, rearrangement, etc.) is detected as change in the LSPR fingerprint parameters.*

Since its invention nearly a decade ago, INPS has contributed to several important developments towards opening up the applicability of nanoplasmonic sensing to other than biosensing-related areas. In the original paper, three different applications were demonstrated to show the versatility of the platform: the glass transition temperature of confined non-conjugated polymers, the kinetics and thermodynamics of hydrogen storage in small Pd particles (< 5 nm), and optical nanocalorimetry of hydrogen oxidation on a Pt nanocatalyst.[147] Further exploitation of INPS resulted in more focused applications in heterogeneous catalysis and materials science[48,156–160] and renowned interest in biosensing,[127,128,161–164] due to its versatility and stability.

Nowadays, the definition of INPS is no longer limited to plasmonic sensor particles being separated by a spacer layer. A configuration where the two entities are spatially separated (*i.e.* located near each other, given that the distance is close enough so that the enhanced field of the antenna reaches the probed materials) fulfills the definition of INPS.[55,165–168] This is best demonstrated by the work of Syrenova et al.[56] where a single Au nanosphere (100 nm diameter) is placed next to a Pd nanocube (< 60 nm side length). At this size, the Pd nanocube exhibits very weak scattering and thus cannot be tracked optically. When the Pd transitions to PdHx, the optical signal originates from Au change and thus the hydrogenation process can be followed.

3 Nanoalloys

More than 4000 years ago, an important discovery was made by our ancestors by smelting tin and copper together to produce bronze, a "new" metal that was harder and more durable than other metals available at the time. This important discovery, celebrated by assigning it to the period where it happened, the Bronze Age, provided significant advantages that eventually led to better technology and society. The concept of combining two or more different metals to produce a new system, the so-called *alloy*, that possesses better properties, persists to this day. In this Chapter, I will briefly discuss the basics of alloys and describe in more detail the palladium-noble metal alloy system due to its direct relevance for my thesis work. Following that, a discussion about segregation occurring in alloys and how alloy nanoparticles can be produced will be given.

3.1 Alloy Formation and Phase Diagram

Alloys constitute an interesting class of materials due to their unique features exemplified above: the synergistic combination of physical and chemical properties of their constituents or even new functionalities. To be in line with the theme of this thesis, the superior properties of alloys are best demonstrated on the example of AuAg alloy nanoparticles. As we have learnt from the last Chapter, at the nanoscale, neat Au and Ag exhibit localized surface plasmon resonance and both systems are considered to be the main plasmonic metals thanks to their excellent optical properties. Individually, however, these two metals have their own (dis)advantages relative to each other. Ag is considered to be the better plasmonic metal due to lower optical losses, which results in a narrower LSPR peak. However, Ag is known to oxidize, hampering its use in many applications. These characteristics are perfectly complemented by Au, which is highly inert but features slightly worse LSPR properties. When combined together, AuAg alloys may exhibit the inertness of Au while retaining the remarkable optical properties of Ag. The case of the AuAg alloy is just an example. A large number of alloy systems have been exploited to produce diversified hybrid materials that enable innovative applications across fields.[107,169–173]

When mixing two elements together (from this point onwards I will limit the discussion only to two-component, or *binary*, alloys), the atomic ordering in the system can take form into two configurations: alloys and intermetallic compounds (**Figure 3.1**). In alloys, the two different types of atoms are randomly and thoroughly mixed. In contrast, in an intermetallic compound, the atoms are arranged orderly with well-defined stoichiometry. Although both types feature a complete mix of the constituent atoms (and therefore are eligible to be called alloy), the term of "alloy" is only used when one refers to the system with random distribution. This classification is important as both types of systems can have significantly different properties,

even when they share similar elemental composition.[172] The specific ordering is mainly prescribed by factors determining the thermodynamics (*e.g.* lattice constant, atomic radii and interactions) and thus is unique for each different case.

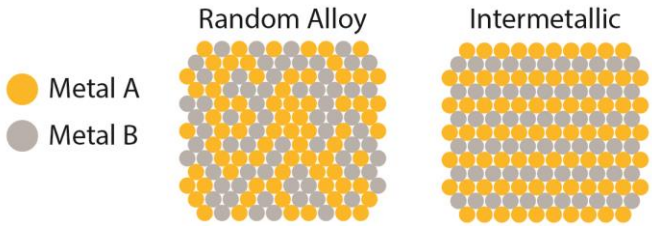

Figure 3.1. Atomic ordering in metal alloys. *In terms of atomic ordering, two major classes of alloys can be distinguished. The term random (or homogeneous) alloy is reserved for systems consisting of metal atoms that are randomly and thoroughly mixed. In contrast, an intermetallic refers to a system that has both long-range atomic order and well-defined stoichiometry. In general, alloys are mainly referred to as systems exhibiting random atomic ordering, the second class is referred to as intermetallic phase.*

In the case of (random) alloys, the degree of mixing and atomic ordering in them depends on a number of factors.[171] In general, the mixing of two metals (A and B) is favoured when the A–B bond is stronger than both the A–A and the B–B bonds. Additionally, similar lattice parameters (*e.g.* crystal structure and lattice constant) and surface energies in both metals will contribute to a more thorough atomic mixing throughout the system. In particular, a large difference in surface energies will lead to a segregated profile, as will be discussed in a later section. Nonetheless, these parameters only define a few attributes of thermodynamically stable alloys, and there is always the possibility of forming a nonequilibrium phase during the alloy formation. As such, it also depends critically on the preparation method and the experimental conditions. For example, at a relatively low reaction temperature the atoms are hindered from reaching their thermodynamically preferred positions through surface and/or bulk diffusion. In such case, additional heating is necessary to accelerate the interdiffusion of atoms, thereby promoting the formation of an alloy.

At equilibrium, for each unique set of experimental parameters (*e.g.* temperature, pressure, alloyant composition) there exist(s) thermodynamically distinct phase(s) of (an) alloy(s). Phase here refers to the state of the material as in gaseous, liquid or solid form. In the solid phase, different characteristics of materials in term of crystallographic structure may also exist. In the case of alloys, the material characteristics also include the mixing state of the constituents, *i.e.* whether alloy formation is achieved or not. This information is summarized in the so-called *phase diagram* chart. In a typical alloy phase diagram, states of the alloy are drawn as function of temperature and alloyant composition. Since each alloy system is unique, the obtained phase at each combination of these two parameters is widely varied. For a complete list of binary and ternary alloy phase diagrams that covers all metallic elements, I refer the reader to the ASM Handbook: Alloy Phase Diagrams.[174] Phase diagrams are of paramount importance in materials science as they provide a "guideline" when designing a material. In the case of alloys, phase diagrams reveal at which conditions and in what system alloys actually form (or not).

Figure 3.2 shows examples of phase diagrams for two different cases of binary systems: AuAg and PdPt. In the former case, the phase diagram shows no features except solid lines that mark the boundary between the liquid and solid phase of the system. Below these lines, Ag and Au form a completely mixed alloy (as indicated in the Figure as (Ag,Au)). From here we learn that Ag and Au basically form an alloy for every composition. In contrast, for the PdPt system there appears an additional dashed line that marks a boundary between different formed phases. As indicated, a separate Pd and Pt phase is formed, which means that they are not mixed. The area where the alloyants are not miscible is called a *miscibility gap*. From the phase diagrams we learn that Pd and Pt are not miscible for a wide range of compositions, ranging from 15 to 95% Pt content at temperatures below 770 °C.

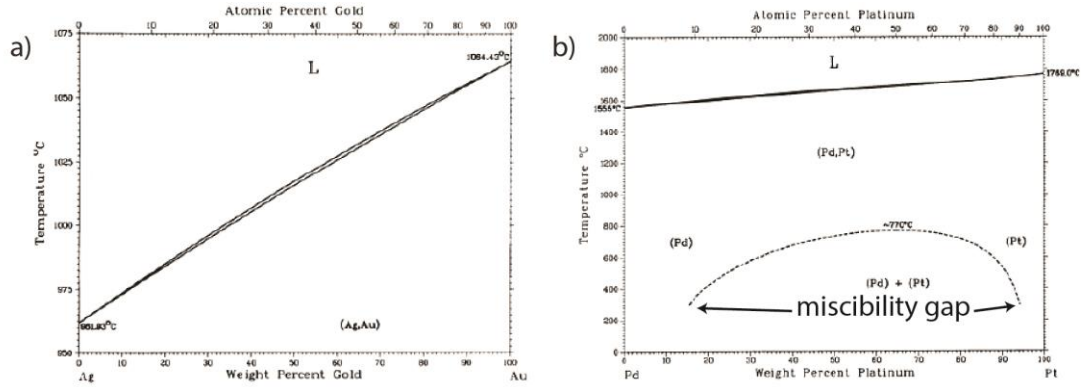

Figure 3.2. AuAg and PdPt phase diagrams. *(a) The AuAg phase diagram features complete miscibility of in the alloy throughout all compositions. (b) The PdPt phase diagram, on the other hand, exhibits a wide miscibility gap (i.e. where a segregated atomic arrangement is instead formed) for temperatures below 770°C and a Pt content of 15–95%. The diagrams are adapted and modified from ref. 174.*

3.2 Pd-based Alloys

Pd is a noble transition metal and belongs to the platinum group in the periodic table. The members of this group, ruthenium, rhodium, palladium, osmium, iridium and platinum, exhibit similar chemical and physical properties: they are resistant to wear, tarnish and chemical attack, and they feature excellent high-temperature characteristics and stable electrical properties. However, the most striking feature of platinum metals is their excellent *catalytic* properties, which means that that they are able to speed up the rate of chemical reactions on their surfaces, without being consumed themselves. Apart from being catalytically active, Pd also has the interesting ability to *spontaneously* absorb large amounts of hydrogen (up to 900 times its volume) at ambient conditions (more will be explained in **Chapter 4**). These properties put Pd a the predicted key material for the successful deployment of the hydrogen economy discussed in **Chapter 1**.[5]

With its status in the two key fields, *i.e.* catalysis and hydrogen economy, studies related to Pd have expanded also to its alloyed form. These efforts are motivated not only by the possibility to conjure other functionalities enabled through synergistic effects but also to gain deeper fundamental understanding of an interesting phenomenon (*e.g.* first order transition in metal

hydride formation) by deliberately changing the system parameters (*e.g.* lattice constant, surface strain) through alloying. The large amount of literature reports related to Pd alloys is also made possible by the fact that Pd is miscible with many other metals.[174] As examples, the phase diagrams of PdAu and PdCu alloys, two systems relevant to this thesis, are shown in **Figure 3.3**. For PdAu, miscible fcc structures are formed at all temperatures and composition except for a narrow range. Specifically, a bcc structure is formed between 8–20% and 55–80% Pd at 600–800°C, while an unknown structure other than fcc is formed for 28–42% Pd at 20–100°C.[174,175] On the other hand, Pd and Cu form continuous fcc solid solutions at temperatures above 600°C, while both bcc and fcc structures are present below 600°C in a very narrow range around 42–48% and 60–70% Pd.[176,177] The different crystalline structures formed at different alloy composition may give rise to different properties such as faster hydrogen diffusion in the bcc structure compared to fcc in PdCu alloys.[176,178–180]

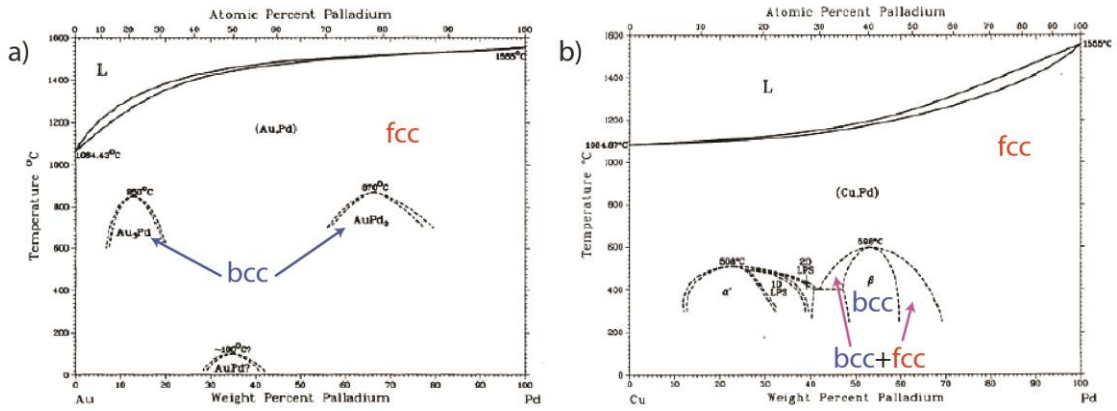

Figure 3.3. PdAu and PdCu phase diagrams. *(a) The PdAu phase diagram features a widely miscible alloy with fcc structrure. Only at a few narrow conditions the formed alloys are bcc. (b) The PdCu phase diagram also exhibits rather widely miscible alloy formation with fcc structure. There are, however, narrow areas where concurrent fcc and bcc structures are formed. The diagrams are adapted and modified from ref. 174.*

To this end, a large number of studies related to Pd alloys have been published. In the field of catalysis where the dependency of activity/selectivity is strongly related to minute details of the catalyst surface (*e.g.* faceting, composition), alloying has flourished as one of the main options for its engineering.[172,173,181] Alloying Pd with various metals, such as Pt, Fe, Ag and Au, has been demonstrated for numerous catalysts in both liquid and gas phase.[169–172,181] In the field of metal hydrides, Pd has been alloyed mainly with noble metals in separation membrane technologies and to eliminate the inherent hysteresis during hydrogen absorption and desorption in pure Pd, as will be discussed in detail in **Chapter 4**. So far, studies related to alloying Pd with Au, Ag, Cu and Ni and their corresponding hysteresis have been conducted.[60,61,182–188] Furthermore, alloying has also been done to engineer the hydrogen permeability and surface chemistry of Pd. As an example for the former, it has been shown that adding higher Au or Ag contents up to 40% leads to higher hydrogen permeability in the Pd lattice.[179,189] In the case of the latter, alloying with Cu results in weaker interaction between Pd surface atoms and CO molecules, poisoning agents that block the Pd surface and consequently hinder hydrogen absorption into Pd.[190–194]

3.3 Surface Segregation in Metallic Alloys

Thermodynamically, segregation of one or more constituents to the surface may occur for all alloy systems regardless of temperature.[195] The tendency of the segregated element (often also identified as impurity) to diffuse to or from a surface may be expressed by its segregation energy, that is the difference between total free energy between a surface site and bulk site.[196] This means that positive segregation energy implies a tendency for an impurity to move into the bulk, while negative segregation energy drives it to the surface. Expectedly, the segregation energy for an element is different for different alloy systems, as well as for the environment they are exposed to (*e.g.* in vacuum or in oxidizing atmosphere). The extent of the segregation also depends on the type of facet of the surface and the size of the system (in the case of nanoparticles), in which segregation features are more apparent with decreasing dimensions.[197–199] Nonetheless, the kinetics of the segregation process are strongly influenced by temperature, that is, it occurs faster at higher temperature. At the end, enrichment of one or more constituents at the surface, and up to a few monolayers underneath, is obtained (**Figure 3.4**).

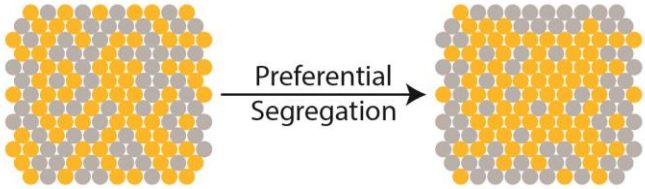

Figure 3.4. Surface segregation. *Over time, one or more elements of an alloy can diffuse and segregate to the surface, creating a different composition at the surface with respect to the bulk. The segregating element depends on the alloy system and the environment it is exposed to. The segregation process is kinetically driven by temperature.*

Segregation creates a different composition at the alloy surface as compared to the bulk and therefore the surface-related properties are expected to be altered. Hence, the functionality of alloy particles enabled by their surface may be enhanced or weakened, depending on the segregated elements. For example, Park et al. observed higher CO oxidation catalytic activity of $Rh_{50}Pt_{50}$ nanoparticles over time and assigned surface segregation of Rh to be the primary cause.[199] On the other hand, Cui et al. used $Pt_{40}Ni_{60}$, $Pt_{50}Ni_{50}$ and $Pt_{60}Ni_{60}$ nanoparticles and studied their oxygen reduction reaction (ORR) activity. They found for all alloys that the activity drops up to 66% when Pt segregates to, and completely dominates, the surface.[200]

As discussed above, Pd-based alloys are one of the most studied systems due to their excellent catalytic properties. Consequently, segregation phenomena in Pd-based alloys are also widely scrutinized both experimentally and theoretically.[201–203] Very recently, Zhao et al. generated an analytical model to predict the surface segregation of 40 binary Pd alloys in vacuum at 600K, whose results are in excellent agreement with the ones available in the literature.[204] Some of the interesting alloys are presented in **Table 3.1**. In the table, different Pd-based alloys are shown together with the segregating element and also their equilibrium composition on the surface with 25 at.% initial composition. Clearly, not only the segregating element varies for different alloys, but also their equilibrium composition on the surface. For PdAu and PdCu alloys, the two alloys of particular interest in this thesis, it is interesting to note that their extent

of segregation is totally different. For PdAu, strong Au segregation to the surface is expected. On the other hand, PdCu has no tendency to segregate as the equilibrium Cu composition at the surface barely changes to 26 at.%, an increase of only 1 at.% from the initial condition. These calculations are in excellent agreement with experimental and theoretical studies and show that indeed Cu and Au atoms segregate to the surface of the corresponding alloys.[195,196,201,203,205] However, the extent of segregation is not as severe for Cu as Au due to its low segregation energy.[196,202]

Table 3.1 Surface segregation for (111) plane of Pd alloys in vacuum at 600K.[204]

Alloy	Segregation Element	x_A^{surf} of $Pd_{75}A_{25}$	Alloy	Segregation Element	x_A^{surf} of $Pd_{75}A_{25}$
PdAg	Ag	52	PdMg	Pd	17
PdAl	Al	37	PdMn	Mn	29
PdAu	Au	71	PdNi	Pd	3
PdCo	Pd	2	PdPt	Pd	1
PdCu	Cu	26	PdY	Pd	0
PdFe	Pd	4	PdZr	Pd	2

Knowing that segregation is an inevitable phenomenon in most of the alloy nanoparticles, and how in many cases it deteriorates their intended functionality, it is thus of great importance to be able to characterize the surface state of alloy nanoparticles. In order to do so, surface-sensitive characterization techniques have been employed. Commonly used techniques include high-resolution electron microscopy, atom probe tomography (APM) and x-ray photoelectron spectroscopy (XPS). Without going into details, electron microscopy and APM are considered to be invasive, in that they actually can interfere and alter the investigated sample due to *i.e.* bombardment with high energy electrons or, in the case of APM, actual removal of materials. Thus, these two techniques are compatible with the characterization of a sample at end of its use, in its final state. In contrast, XPS is non-invasive but quite slow and time-consuming, as will be explained in detail in **Chapter 6**. Finding a novel way to characterize segregation in nanoparticles in situ and in real time to reveals its dynamics is thus highly desirable. Relying on the fact that nanoplasmonic particles are surface sensitive (see **Chapter 2**), in **Paper VII,** I demonstrated using PdAu as model system that the segregation occurring on alloy nanoparticles can actually be tracked by monitoring the LSPR spectra, in particular through the change in peak position λ_{peak}. I found that the change in λ_{peak} is proportional to the change of the PdAu composition on the surface measured by XPS, and that the correlation between the two is in good agreement with the literature.

3.4 Synthesis and Fabrication of Alloy Nanoparticles

The widely interesting and tunable properties of alloy nanoparticles has created a need to establish robust, reproducible and high-yield alloy nanoparticle production methods. Two main methods can be categorized: wet-chemical synthesis and physical deposition methods.

3.4.1 Wet-Chemical Synthesis

Wet-chemical or colloidal synthesis refers to growth of solid metal nanoparticles via chemical reaction in a liquid reaction medium. Wet-chemical synthesis is also called bench chemistry since it is most often performed in lab benches and requires simple setups. This simplicity (however please mind that simplicity of the equipment used here does not necessarily correlate to the simplicity in obtaining the intended products) is also accompanied by other advantages, such as high-yield, scalability and low-cost. Therefore, wet synthesis has been the main technique to produce alloy nanoparticles. There are three distinct methods to produce alloy nanoparticles, that is, co-reduction, thermal decomposition and seed-mediated growth.

3.4.1.1 Co-reduction

Co-reduction is possibly the most straightforward and simplest technique to produce alloy nanoparticles, as it is commonly used as the main technique to synthesize monometallic nanoparticles with different size and shape.[172,206,207] The technique is based on the reduction of metal salts (compounds in which the hydrogen of an acid is replaced by a metal *e.g.* $AuCl_3$) by reducing agents, which later transforms the metallic ions into neutral atoms (*e.g.* $M^{n+} \rightarrow M^0$, $n > 0$). The free metallic atoms quickly nucleate into small metallic clusters, which become the basis for the remaining formed neutral atoms to bind and consequently grow isotropically in size. To synthesize alloy nanoparticles with different composition, simultaneously reducing metal salt precursors with different molar concentration is done. Co-reduction has been largely used to produce AuAg alloy nanoparticles.[107,110,112,172,208–212]

In many cases, one is interested in synthesizing nanoparticles not only with controlled composition, but also shape and crystal orientation to achieve certain properties. In wet synthesis, this can be achieved by employing surface capping agents that selectively bind to specific facets of the nanoparticles, which subsequently block the growth in in corresponding facets. To this end, different types of surface capping agents have employed, such as organic ligands, polymers and surfactants, to produce alloy nanoparticles with different shapes, for example cubes,[213–215] tetrahedra[214,215] and octrahedra.[213,215] However, bound capping agents on nanoparticles may significantly affect their surface properties. For example, in the application of catalysis, capping agents may hinder the catalytic activity by blocking the active surface. It is then important to establish proper cleaning procedures to remove the capping agents while retaining the nanoparticle properties (*e.g.* shape, size and composition).

Despite its simplicity, co-reduction of alloys may not work for arbitrary metal components, as the reduction rate, determined by a parameter called reduction potential, of each metal varies. In short, the bigger the difference between the reduction potential of the metal components, the less likely that the alloy produced has the intended composition, or is formed at all, as one component reduces faster than the other. For example, in a mixture consisting of Au and Cu

(reduction potentials of 1.50 and 0.34 V, respectively), the Au will reduce faster than Cu, resulting in alloys with higher Au content than expected. A way to synchronize the reduction rate of the precursors is by varying their molar concentration.[216] This, however, introduces another complication as the determination of the needed precursor concentration for a certain composition is different for different alloys, reaction temperature, used metal salts and solvents, etc.

3.4.1.2 Thermal Decomposition

In thermal decomposition, reduction of metal precursors is not done by reducing agents but rather, as the name suggests, by high temperature. Thus, thermal decomposition is mainly used to synthesize monometallic or alloy nanoparticles comprising metals with low reduction potentials (*e.g.* Fe, Co and Ni). Additionally, organometallic precursors (*e.g.* acetylacetonates $M(acac)_n$ and carbonyls $M_x(CO)_y$), which are readily decomposed under moderate heating, *i.e.* 150°C, are used instead.[217,218] Thermal decomposition shares similar traits to co-reduction as explained above. In fact, the two methods can be combined, as demonstrated by Sun and co-workers who synthesized FePt nanoparticles by reducing the Pt and decomposing the Fe simultaneously.[219–221] A clear advantage of thermal decomposition compared to co-reduction is the possibility to employ bimetallic precursors. This is made possible especially for carbonyl precursors, by reacting one precursor with another.[222] Thus, during synthesis, both metallic atoms decompose simultaneously to form alloy nanoparticles. This drastically simplifies the reaction mechanism (otherwise careful determination of precursors concentration has to be done in order to match the reduction rates of the alloyants, as explained above) and provides more precise control over the alloy composition, which is defined by the composition of the bimetallic precursors. To this end, alloy nanoparticles comprising $FeCO_3$, FePt, $FeNi_4$ and Fe_4Pt have been successfully synthesized using bimetallic precursors.[222,223]

At this point it is important to discuss one key characteristic of nanoparticles produced by co-reduction and thermal decomposition, that is, their polydispersity. Polydispersity refers to variation in terms of size and shape of the nanoparticles, which might be undesired. In general, during reduction of metallic atoms, they may undergo homogeneous or heterogeneous nucleation. The former occurs when the concentration of atoms reaches a high enough level (also called supersaturation), which leads to clustering and formation of stable seeds. The latter takes place when the atoms are added *directly* to the surface of preformed seeds. The driving force of heterogeneous nucleation is far less than homogeneous nucleation and thus can already take place in the absence of homogeneous nucleation (*i.e.* self-nucleation), provided that the atom concentration is kept below supersaturation, but high enough to overcome the heterogeneous nucleation barrier. When both types of nucleation occur simultaneously, the formed nanoparticles will be generally characterized by polydispersity, in shape and size, whose degree increases as the reaction time extends. This is made worse by the sensitivity of homogeneous nucleation to slight variation in *e.g.* temperatures. For this reason, both coreduction and thermal decomposition have been so far used to synthesize nanoparticles with size less than 30 nm.[110,112,209,210,224–228] Beyond that, large variation in size and shape are unavoidable, which makes utilization of produced nanoparticles in *e.g.* plasmonics, the main theme in this thesis, very limited.

3.4.1.3 Seed-Mediated Growth

To circumvent the size limitation (as direct consequence of polydispersity) above, a more recent technique called seed-mediated growth was developed. The concept behind this method is to have seeds already existing in the solution, onto which atoms deposit, and thus prevent self-nucleation.[229–231] Precise control of the seeds, in particular their internal defect structure and crystallinity, can facilitate growth of monodispersed nanoparticles with defined shapes with relatively large dimensions.[232,233]

Despite this advantage, successful efforts on synthesizing alloy nanoparticles with dimension beyond 50 nm are lacking. Only recently Rioux and Meunier demonstrated controlled synthesis of AuAg alloy nanoparticles with dimensions ranging from 30 to 150 nm.[234] They achieved this by using multistep seeded growth. At the beginning they started with a small Au seed, which later Au and Ag are grown onto. After a specific time they stopped the synthesis and used the produced alloys as seeds for the subsequent step. By doing these steps repeatedly, excellent control of the nanoparticle size with narrow distribution can be obtained. However, the resulting alloys do not feature homogeneous composition over the nanoparticle. Instead, a gradual profile was achieved, in which the Ag (Au) concentration increases (decreases) towards the surface.

All three wet synthesis methods described above has been the key workhorses for the vast advancement in the field of colloidal particles and their applications. However, until today, we rarely see their application in solid state devices, especially for nanoplasmonics-related applications, the main theme of this thesis. One of the main reasons is that the products of wet synthesis come in solution. However, solid state and plasmonic applications often require integration of arrays of nanoparticles on a surface with specified orientation, surface density, coverage uniformity, etc. This is very difficult, if not impossible, to achieve with colloidal nanoparticles. Furthermore, as noted above, reproducibility is always an issue with colloidal synthesis. Since the process is very sensitive and is largely dependent on the human factor, batch-to-batch uncertainties are inevitable, resulting in low reproducibility. As a way to overcome these two limitations, recent years see the wide use of physical deposition methods to produce alloy nanoparticles.

3.4.2 Physical Deposition Method

Physical deposition methods of alloys rely on the transfer of solid material from a target *directly* onto a substrate. This process is explained in detail in **Chapter 5**. In brief, physical deposition methods are usually carried out in *fully automatized* systems, whose deposition accuracy can be on the order of Ångström. Although reports on deposition methods to produce alloy nanoparticles are limited (especially if compared to wet-chemical synthesis), two specific techniques are commonly used: pulsed laser deposition and the dewetting method.

3.4.2.1 Pulsed Laser Deposition

Pulsed laser deposition (PLD) employs a focused high-power pulsed laser beam to strike a material target to be deposited. The pulse usually lasts for a very short time (order of nanoseconds) and thus hundreds, if not thousands, of cycles are necessary to produce nanoparticles with a certain size. To produce alloy nanoparticles, two (or more) pure alloyant

targets are used. Sequential pulses to each of the targets are carried out, for which the relative number of pulses for each target defines the alloy composition. However, the nanoparticle dimension achieved using this technique is very limited, as at a certain critical thicknesses, deposition will lead to formation of a continuous thin film instead of nanoparticles. The critical thickness can be made larger by increasing the substrate temperature. To this end, PLD has been used mainly to produce AuAg alloy nanoparticles with a maximum diameter of 40 nm, obtained by deposition at 300ºC.[235,236]

3.4.2.2 Dewetting Method

Instead of employing pulses of deposition to mix the alloyant materials, one can instead deposit them at the same time or one after the other in its entirety and then heat them at high temperature afterwards. The heating does not only provide the energy to mix the alloyants but also induces transformation of the film to become nanoparticles to minimize the total surface area[237] (**Figure 3.5**). This transformation is also driven by poor "wetting" of metals on commonly used substrates (*i.e.* silica, quartz); hence the dewetting term. Similar to PLD, the wanted alloy composition can be controlled by adjusting the thickness of each alloyant element layer. However, the dewetting method improves PLD in one respect in that the annealing is done after deposition. This enables wider annealing parameters *e.g.* higher temperature, exposure to gases etc. Thus, larger nanoparticles can be obtained by simply depositing thicker thin films and then anneal them at very high temperature. Both co-deposition and subsequent deposition type dewetting methods have been employed in the past years to produce AuAg[109,238–240] and even ternary AuAgPd[241] alloy nanoparticles. Notably, Gong et al. successfully fabricated 250 nm AuAg nanoparticles by depositing a 15 nm precursor film followed by annealing at 600ºC.

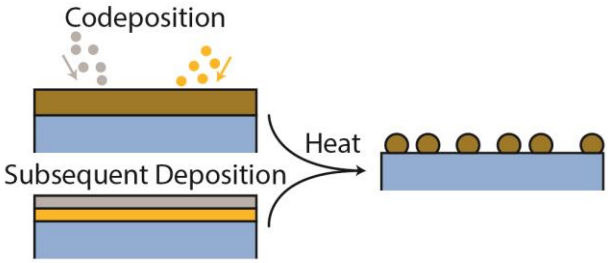

Figure 3.5. Alloy nanoparticle fabrication via dewetting. *Thin film of alloyants, which can be deposited simultaneously (top-left) or subsequently (bottom-left), can be transformed to nanoparticles (right) by heating to high temperature. The formation of nanoparticles is driven by the poor wetting of the metals on the substrate.*

Despite providing direct fabrication of nanoparticles directly on substrates with higher degree of reproducibility, the physical deposition methods presented above are still not good enough in that they do not provide real control of the particle dimensions and shapes. Specifically, for the dewetting method, the different nanoparticle dimensions are achieved by adjusting the initial film thickness. This, however, is not the only parameter defining the final particle dimensions. Other parameters such as heating temperature and environment, as well as the alloyant components, affect the final result. As such, a unique set of thickness libraries must be developed for each set of experiment conditions, hindering its wide use to produce a wide

variety of alloys (as shown by the very limited alloy systems that have been produced this way). Furthermore, nanoparticles formed via dewetting are characterized by very large size distribution, which is undesired in many applications. Finally, as a general characteristic, alloy nanoparticles produced by physical deposition methods are commonly polycrystalline, in contrast to wet chemical methods that generate single crystalline particles.

In order to enable the development of hydrogen sensors employing alloy nanoparticles aimed at in this thesis, it is then imperative to establish a generic method that allows the (facile) fabrication of alloy nanoparticles directly on a surface with excellent control of their size, shape arrangement and composition. In general, such a method will also benefit much wider application fields such as plasmonics and catalysis. Combining the idea from the dewetting method, in which alloy formation is facilitated by annealing, and the fabrication of nanoparticles through a lithography mask, I developed a generic alloy fabrication strategy in **Paper I**, whose details are explained in **Chapter 5**.

4 Hydrogen in Metals

Exactly 152 years ago, Thomas Graham, an English chemist, discovered that palladium could absorb a lot of hydrogen at ambient conditions.[242] With his discovery, the foundation for a wealth of research on the fascinating metal-hydrogen interactions was laid, and many applications of hydrogen in metals have been established and proposed since his pioneering study. In this chapter I will briefly discuss the general behaviour of hydrogen sorption in a metal (with emphasis on the palladium hydride system), followed by the specific application of metal-hydrogen interactions in hydrogen detection systems, with more focus on the nanoplasmonic hydrogen sensors.

4.1 Metal Hydrides

Being the smallest element in the universe, hydrogen atoms can occupy interstitial sites in many metal lattices to form stable compounds *i.e.* so-called hydrides. The phase transformation of a metal to a metal hydride can be classified into different steps. Here I will briefly discuss the physics and phenomena related to the absorption of hydrogen in metals. After starting from bulk systems I will then move on to more specific cases at the nanoscale and involving alloyed hydrides.

4.1.1 Bulk Metal Hydride Systems

4.1.1.1 H-Adsorption on Surfaces

As hydrogen molecules (H_2) approach a metal surface they may adsorb on it via physi- or chemisorption. At ambient conditions, many metals do not dissociate the adsorbed hydrogen molecules (*i.e.* breaking them into hydrogen atoms H) since it is usually an activated process (*i.e.* it requires energy, see the E_{diss} in energy landscape schematic shown in **Figure 4.1**). However, Pd possesses high catalytic activity in that it can *readily* dissociate H_2 on its surface even at ambient conditions (*i.e.* E_{diss} is nearly zero).

Once hydrogen atoms have been formed, they reside not only on the sites on top of the metal surface but also penetrate into interstitial sites (*i.e.* in between metal atoms) in a layer below the surface (so-called subsurface) and further down into the bulk. When diffusing into the bulk, hydrogen atoms face a varying energy landscape, as shown in **Figure 4.1**. Specifically, the subsurface regime in a pure metal is commonly comprised of energetically more favourable sites for hydrogen to occupy as compared to the bulk sites. As a consequence, the subsurface sites will always be filled with hydrogen, regardless of the hydrogen concentration in the bulk. To this end, the extension of the subsurface layer has been proposed to be in between 0.3-1 nm.[56,59,243–245] The presence of hydrogen in the subsurface layer leads to the generation of lattice

strain, which can influence the thermodynamics of the sorption process, especially in a nanoscale system, as discussed in detail later in the Chapter.

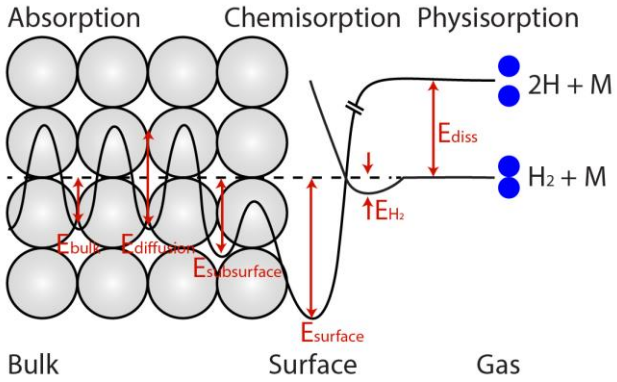

Figure 4.1. Energy landscape encountered by hydrogen when interacting with a metal. *Hydrogen molecules may experience various energy barriers when approaching a metal surface, dissociating into hydrogen atoms and diffusing into the bulk.* E_{diss} *is the dissociation energy of a hydrogen molecule,* E_{H2} *is the binding energy of a physisorbed hydrogen molecule,* $E_{surface}$, $E_{subsurface}$ *and* E_{bulk} *are absorption energies of a hydrogen atom at the surface, subsurface and bulk of the metal, respectively.* E_{diff} *is the activation energy for hydrogen diffusion in the bulk. The schematic is adapted from ref. 246.*

The surface of a metal is literally the first and last contact of hydrogen upon interaction and therefore it plays a key role for its absorption and desorption processes. The kinetics of the sorption process may therefore be expected to be highly influenced by the surface state. In the case of desorption, association of hydrogen atoms to hydrogen molecules facilitated by the metal surface has been demonstrated to be the rate limiting step.[247–249] Modification of the physical and chemical properties of the surface, such as addition of impurities or adsorbed species, and atomic geometrical changes due to *e.g.* different faceting, alloying, etc. can therefore affect the sorption processes and also the overall energy landscape.[246,250–252]

4.1.1.2 Hydride Formation

When a metal is exposed to increasing hydrogen partial pressure, hydrogen sorption will take place via several stages, as sketched in **Figure 4.2**. At low hydrogen partial pressures, a solid solution of hydrogen in the host lattice is formed. This is called the α-phase. In the α-phase, the attractive hydrogen-hydrogen interactions in the lattice are very weak since the amount of hydrogen is very low and thus the hydrogen atoms are far away from each other. Nonetheless, inclusion of hydrogen in interstitial lattice sites induces a long-range strain in the lattice of the host. In this low concentration regime, the system obeys Sieverts' law in which positive correlation between the externally applied hydrogen partial pressure and the equilibrium hydrogen concentration in the metal exists.[253] This law, which now is used to describe gas solubility in solids, can be quantified as

$$\sqrt{p_{H2}} = n_H K_S \qquad (4.1)$$

where p_{H2} is the partial pressure of hydrogen gas, n_H is the hydrogen concentration in the metal (commonly expressed as *H/M i.e.* hydrogen per metal atom ratio) and K_S is the Sieverts constant.

As the hydrogen partial pressure is increased further, the amount of hydrogen in the metal will also increase until a certain point where the metal-mediated attractive hydrogen-hydrogen interactions become appreciable due to more prominent lattice strain and electronic interactions. This causes hydrogen atoms to accumulate and form clusters (since this is energetically more favourable as, for example, the lattice strain is minimised), eventually leading to the formation of domains where all sites are occupied. This is called the β-phase. The transition from α-phase to β-phase is of first order. During the phase transition, the α-phase and β-phase coexist in equilibrium and the growth of the β-phase occurs at the expense of the α-phase. Eventually, the entire system is converted to β-phase and any further increase in hydrogen partial pressure will only result in minor changes in the hydrogen content in the hydride.[254] At the end, the fully hydrided metal will have an expanded lattice structure due to incorporation of hydrogen. In the case of Pd, at its fully hydrided state $PdH_{0.67}$[255] at room temperature a lattice constant increase from 3.89 Å to 4.03 Å is observed. This corresponds to a significant 10% increase in volume.

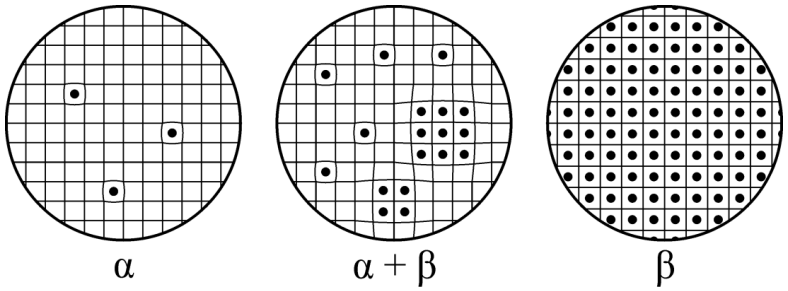

Figure 4.2. Different stages during hydride formation/decomposition. *At low hydrogen partial pressures, few hydrogen atoms sit in interstitial lattice sites in the metal, constituting a solid solution called α-phase. The hydrogen atoms locally strain the host lattice and the strain field created has relatively long range. Further increase of hydrogen pressure results in appreciable hydrogen-hydrogen interactions via these strain fields, which lead to the formation of nuclei of the hydride (β-phase) due to "clustering" of hydrogen atoms to reduce the total energy of the system. The growth of the β-phase continues until the entire metal is transformed to hydride. The figure is reproduced from ref. 256 with permission.*

A standard procedure to study the hydrogenation process in a metal is to map the hydrogen content in the host as a function of the hydrogen partial pressure at constant temperature; the so-called *p-C* (pressure-composition) isotherms (**Figure 4.3**a). In the α-phase, the hydrogen content changes slowly with increasing hydrogen pressure. As the β-phase formation is started, there is a dramatic change in the hydrogen content in the metal over a very narrow pressure range. This region, where α-phase and β-phase coexist, appears as plateau in the isotherm and is characterized by the "plateau pressure" in the middle of the plateau.

If one reverses the process by reducing the hydrogen pressure to induce hydride decomposition, a similar process will occur with the only difference that the plateau pressure (*i.e.* when the β-

phase starts to decompose into the α-phase) will usually be at lower hydrogen pressure compared to the one during hydride formation (see the dashed lines in **Figure 4.3**a). This constitutes a *hysteresis* between hydrogen formation and decomposition, whose details will be discussed in a later section.

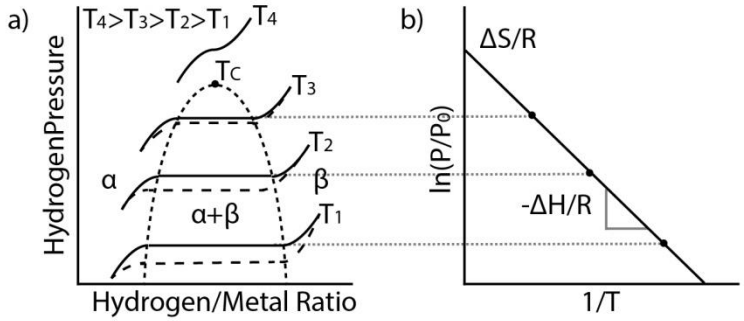

Figure 4.3. Sketch of p-C isotherms and the metal-hydrogen phase diagram. *(a) At constant temperature, in the simplest case of a binary hydride, there are three different phases; α-phase at low hydrogen pressure, mixed α-phase and β-phase region that occurs in a very narrow hydrogen pressure range ("plateau") and the β-phase at the highest pressures. The equilibrium plateau pressure is temperature dependent and different equilibrium plateau pressures are exhibited for hydride formation and decomposition due to hysteresis. The width of the plateau and the width of the hysteresis shrink for higher temperatures until they eventually vanish at the critical temperature T_C. (b) Via van' t Hoff analysis, ΔH* and *ΔS can be derived from the temperature dependence of the plateau pressure.*

The equilibrium plateau pressures of a metal hydride system depend on the temperature. Thus, by carrying out the *p-C* measurements at different temperatures, one is able to construct the phase diagram for the considered metal-hydrogen system, as shown in **Figure 4.3**a As the temperature increases, the plateau region (*i.e.* where α-phase and β-phase coexist) and the hysteresis between hydride formation and decomposition continuously shrink until both features completely disappear above the so-called critical temperature (T_C). Thus, for a temperature higher than T_C, the transition from α-phase to β-phase takes place continuously and reversibly when going the other way.

At the plateau pressure, equilibrium between the hydrogen in the gas phase and the hydride phase is achieved and thus the chemical potentials of hydrogen in the two phases are equal. From this equality arises the van' t Hoff equation:

$$\ln\left(\frac{P}{P_0}\right) = \frac{-\Delta H}{RT} + \frac{\Delta S}{R} \qquad (4.2)$$

where P is the plateau pressure, P_0 is the atmospheric pressure (*i.e.* 1013 mbar) T is the temperature, R is the gas constant and ΔH and ΔS are the changes in enthalpy and entropy during the hydride formation, respectively. By plotting $\ln(P/P_0)$ vs. $1/T$, if a straight line is obtained, ΔH and ΔS can be determined from the slope and intersection with the y-axis, respectively

(**Figure 4.3**b). These parameters indicate the thermodynamic stability of the metal hydride and the change of entropy compared to hydrogen molecules in the gas phase.

4.1.1.3 Hysteresis

The hysteresis feature during hydride formation and decomposition (see **Figure 4.4**a) in metals implies that different mechanisms are involved. This hysteresis is a consequence of the lattice strain induced by the hydrogen presence in the metal lattice that causes volume expansion. The strain creates an energy barrier between the two phases that is different for hydride formation and decomposition and that thermally cannot be surmounted.[27] Hydride formation or decomposition can then occur by applying additional (higher or lower) pressure compared to the ideal strain-free lattice, in which no hysteresis would occur. During absorption, this mechanism is energetically valid only for an open system (*i.e.* α- and β-phase are in dynamic equilibrium with a large reservoir of solute, *i.e.* hydrogen molecules) with coherent phase transformation from metal to hydride. A coherent phase transformation indicates that the interface beween the α- and β-phase is not disrupted (**Figure 4.4**b) despite significant stress imposed by the hydrogen, which leads to an elastic energy contribution to the enthalpy. This additional energy barrier cannot be surmounted by thermal fluctuations and is proportional to the system volume up to a critical size, as discussed later in the Chapter. In contrast, an incoherent transformation occurs during hydride decomposition. This means that the interface between β- and α-phase is discontinuous and dislocations are generated to minimize the elastic stress (**Figure 4.4**b). The precipitates (α-phase in this case) nucleate and grow in the corresponding β-phase matrix.

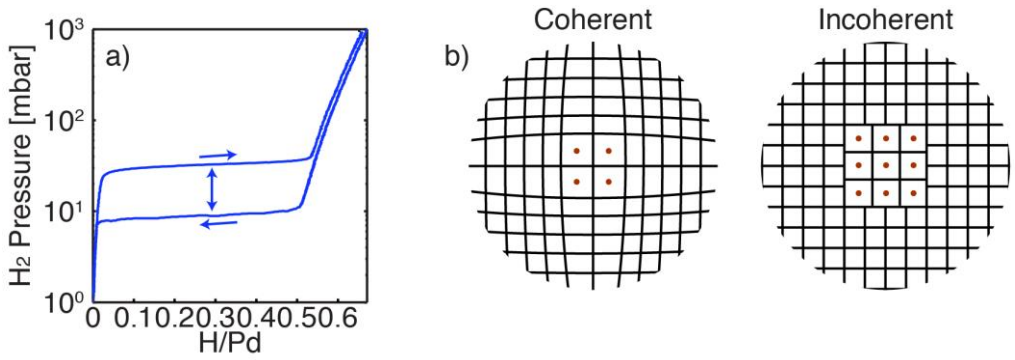

Figure 4.4. Hysteresis and related lattice expansions. *(a) A typical p-C isotherm of Pd exhibiting a plateau for hydride formation (right-pointing arrow) and decomposition (left-pointing arrow) that occur at different pressures. This corresponds to hysteresis, as marked by the double-headed arrow. (b) Sketch of coherent and incoherent phase nucleation. The dots indicate sub-volumes with interstitial hydrogen atoms. In the coherent process, there is a continuous variation in the lattice spacing that gives rise to coherency strain. In the incoherent process, dislocations are readily generated to release the stress which results in a discontinuous lattice interface between α- and β-phase.*

The extent of the hysteresis in a metal hydride system can be assessed by examining its critical temperature, T_C, which marks the point where the two-phase coexistence region disappears (see **Figure 4.3**). In principle T_C can be engineered by material design addressing the main factor

behind hysteresis, that is, strain. Thus, for example by pre-straining the host lattice, *e.g.* by size reduction to the nanoscale (thereby increasing the importance of the subsurface sites described above) or by alloying with other elements with different lattice constant than the host, it is possible to engineer the position of the plateau pressure along the pressure axis and thus engineer both hysteresis and thermodynamics of the hydride, as will be discussed later in this Chapter.

4.1.2 Role of Microstructure

Microstructural details in materials are expected to affect the material properties. In the case of polycrystalline materials, the microstructure is characterized by defects such as vacancies, dislocations and grain boundaries in the polycrystals. In this section I will briefly discuss how microstructure is important to understand some of the findings obtained in my thesis.

4.1.2.1 Grain Boundaries and Crystallites

A grain boundary is an interface between two grains, or *crystallites*, in a polycrystalline material. Grain boundaries are categorized as defects in crystalline solids as they mark a "disturbance" in the periodicity of the crystal structure. Since grain boundaries serve as conjugation interface between two grains, the grain boundary regions are subject to high strain, resulting in energy states that are different from the crystal interior. Depending on the misorientation degree of the crystallites, grain boundaries can be categorized as low-angle grain boundaries (LAGBs), for misorientation angle of less than 15^{o}, and high angle grain boundaries (HAGBs) for misorientation angle of more than 15^{o}. There is also a type called twin boundaries which separate crystals in a symmetrical manner.[257]

Due to their energetics, grain boundaries act as sinks for the accumulation of impurities, as well as species like hydrogen.[258,259] Furthermore, as has been shown for the case of Pd, grain boundaries can serve as a "highway" for hydrogen, which improves the hydrogen diffusion in the crystal.[260] Preferential accumulation of hydrogen on grain boundaries also give rise to large stress in the crystal interior and consequently thermodynamics of hydride formation may be affected. In a recent work, Alekseeva et al. identified that the lattice stress generated in polycrystalline Pd nanoparticles (reflected in the hydride formation plateau pressure) is proportional to the total grain boundary length and the abundance of HAGB type.[57]

In polycrystalline materials, the individual crystallites may possess different characteristics (*i.e.* size, crystallographic orientation, lattice strain). In some nanocrystal systems this also holds true, for example in the case of icosahedra nanoparticles, a geometry consisting of 20 tetrahedrons. As such, a question may arise whether each of this individual building block acts on its own during the hydrogenation process or if they act collectively as an indistinguishable unit. Two very recent studies on Pd answer this question. In the similar work mentioned above, Alekseeva et al. also studied a particle consisting of two differently sized crystallites. The corresponding isotherm for the sample features two distinct plateau pressures, which can be assigned to each crystallite.[57] Along the same lines, using icosahedra nanocrystals, Narayan et al. beautifully demonstrated that each tetrahedron in the crystal actually hydrogenated at a different hydrogen pressure *individually*.[261] The plateau pressure for each tetrahedron is found

to correlate with the stress state in each of the crystallites. These two studies reveal that materials comprising different crystallites can be considered as a collection of single crystallites that exhibit characteristics similar to those of "free" crystallites. It also shows that the characteristics of a polycrystalline system will be defined mainly by the details in the microstructure instead of its overall dimension. Therefore one may expect that *e.g.* a polycrystalline system consisting of smaller crystallites will absorb hydrogen faster than the one with bigger crystallites, even if the their overall system size is similar.

4.1.3 Metal Hydrides at the Nanoscale

A major motivation to downsize a system to the nanoscale is to exploit different (sometimes new, like the case of the optical properties discussed in **Chapter 2**) material properties. Similarly in metal hydrides, nanosizing is mainly done to provide *e.g.* faster and more efficient hydrogen storage materials.[262] Nanosized storage entities provide short diffusion length (thus faster kinetics[247,262]) and their thermodynamics may differ from bulk materials. For example, the hydride can be destabilized, *i.e.* lower energy is required to decompose the hydride, related to ΔH discussed above.

As the volume of a system decreases, its surface-to-volume ratio increases. Thus, for nanoparticles, their microstructural components such as subsurface sites and grain boundaries are expected to play an increasingly important role. This is because their number becomes comparable with the total number of sites in the system.

At least two main mechanisms are responsible for some of the different behaviours observed in this size regime. First is the abundance of atoms residing on corners or edges (especially for nanoparticles smaller than 10 nm), which gives rise to higher reactivity to hydrogen.[262] Secondly, a more prominent role of surface strain, mainly imposed by subsurface hydrogen and defects such as grain boundaries, has been identified.[243,263] As discussed above, the appearance of hysteresis is mainly attributed to lattice stress generation upon hydrogen absorption. Thus, when surface strain plays a greater role in small nanoparticles, hysteresis is also affected. In the case of Pd, inherent stress existing in small nanoparticles reduces the barrier that has to be surmounted by the system, which consequently results in a lower hydride formation plateau pressure (therefore reduction in the hysteresis width and T_C).[263–268] Why, as observed in several studies,[56,57,269] the dehydrogenation plateau pressure is unaffected remains an open question to this date.

Another behaviour observed in small nanoparticles is increased and decreased solubility in the α- and β-phase, respectively. Together, these two effects give rise to a narrowing of the coexistence plateau. An explanation for both observations has been proposed to be the increasing subsurface-to-bulk site ratio, as well as the abundance of grain boundaries for nanocrystalline systems. Regardless of external pressure, the subsurface (and grain boundaries) are likely to be fully occupied (thus form hydride) due to their favourable energetics (see **Figure 4.1**). Hence, for smaller nanoparticles, the hydrogen concentration in the α-phase "appears" to be higher due to a larger contribution of subsurface sites and grain boundaries.[263] At higher

external hydrogen pressure, consequently, only the core transforms to hydride. Since the core shrinks in size as the nanoparticles get smaller, the relative solubility in the β-phase reduces.

For nanoparticles with dimensions larger than 10 nm, two regimes exist. Up to a critical dimension, the trend in thermodynamics follows the one describe above in that plateau pressure and hysteresis width are proportional to the volume.[56,59,270] As recently put forward by Baldi et al.,[59] which was later confirmed by Syrenova et al.[56] and Griessen et al.,[269] Pd nanocrystals with size beyond 30 nm do not follow this trend anymore, and instead behave uniformly more like a bulk system. The reason is that at that sizes the nanocrystal can initiate dislocations to release the strain imposed by the subsurface layer, and thus enough energy is obtained to form the hydride. These results are in good agreement with available studies reporting Pd nanodisks with diameter larger than 100 nm (including the work in this thesis). In all of these reports, the thermodynamic properties of the Pd nanodisk structures are bulk-like with respect to their hydrogen solubility in both α- and β-phase, as well as the extent and width of the hysteresis.[52,55,58,151]

Finally, it is also important to mention that, at the nanoscale, the consequences of crystal expansion when the system is hydrogenated are not as severe as for bulk, where it is the main cause for embrittlement, cracking and peeling when bound to a substrate. For applications, this means that nanoscale hydrides promise potential improvement in durability. Recent work by Ulvestad and Yau also showed that Pd nanoparticles have the ability to self-heal induced defects during hydrogenation.[271]

4.1.4 Metal-Alloy Hydrides

Efforts to mix hydride-forming metals with other elements into an alloy have been done as early as in the 1970s with the aim to mainly engineer the hydrogen permeability, as well as to reduce hydrogen embrittlement.[272–274] In most of the cases, alloying was done by mixing *e.g.* Pd with other noble metals with different lattice constant (smaller or larger) such as Au, Ag, Cu, Ni. The resulting alloys will then possess a lattice constant in between the ones of the two alloyants. The absolute value linearly depends on the composition, as described by Vegard's law.[275] Accordingly, the host metal lattice may be expanded or contracted, depending on the metal it is alloyed with. This change in the lattice state will affect both thermodynamics and kinetics of the hydride formation.[276,277] To provide a brief explanation of such phenomena without unnecessary complication, the discussion below will be limited to the cases where the hydride-forming metal is alloyed with metals that do not interact strongly with hydrogen.

When the host metal is expanded, such as in the case of PdAu and PdAg (a_{Pd} = 3.89 Å, a_{Au} = 4.08 Å, a_{Ag} = 4.09 Å, the barrier that has to be surmounted for the hydride formation phase transition to happen lowers and, hence, hydrogenation can occur at lower pressure.[185–187,278] In contrary, when the host metal is contracted, higher energy is required to initiate the hydrogenation and therefore the plateau pressure increases as compared to pure host metal. This is best exemplified by the system of PdCu and PdNi alloys (a_{Cu} = 3.61 Å, a_{Ni} = 3.54 Å).[182–184,279] The degree of the expansion/contraction is proportional to the alloyant content. Thus, the higher the concentration of the alloyants, the further the plateau pressure shifts from the one of

pure system. In **Figure 4.5** isotherms of PdCu and PdAu alloy nanoparticles used in this thesis are shown. In the case of PdCu, for higher Cu content, the plateau pressure increases until eventually at 30 at.% of Cu the α-phase is extended up to 1000 mbar H_2 pressure.

From **Figure 4.5** it is also clear that for both the PdCu and PdAu system, the hysteresis shrinks for an alloy with higher alloyant content. Since hysteresis relates to the strain properties of the system, as described before, its extent depends on the degree of the strain difference between the pure metal and metal hydride states. Because alloy systems can be considered to be pre-strained (expanded or contracted), the additional strain generated by the incorporation of hydrogen into the lattice will be less severe compared to the "relaxed" pure system.[280] Thus, the hysteresis corresponding to the hydride formation and decomposition decreases as the alloy content increases. It has been shown both theoretically and experimentally that alloying Pd with the coinage metals Au, Ag and Cu to > 25% lowers the T_C to below room temperature, resulting in hysteresis-free isotherms.[61,144,185–187,278,281] As discussed later in the Chapter, this feature is highly desired for sensing applications.

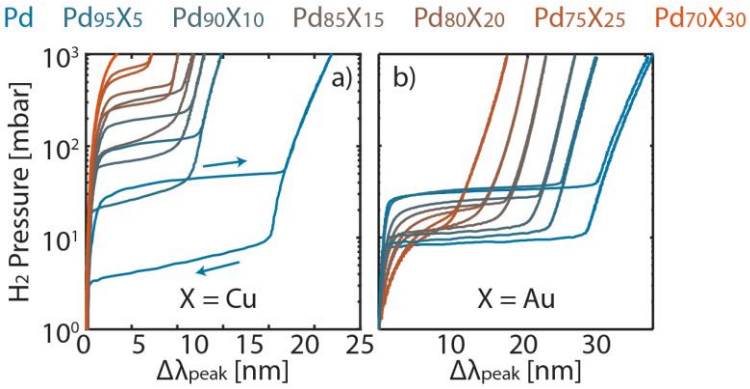

Figure 4.5. Hydride formation and decomposition isotherms for alloyed Pd. *(a) Isotherms of (a) PdCu and (b) PdAu alloy nanoparticles. In the case of PdCu where the lattice is contracted, higher Cu contents leads to higher plateau pressure. This is in stark contrast to PdAu, where the lattice is expanded. Upon adding more Au in the alloy, the plateau actually is shifted to lower pressure. Interestingly for both systems, the hysteresis shrinks and the plateau width narrows. Right- and left-pointing arrows in panel (a) denote the absorption and desorption branch, respectively.*

Another property that is affected by alloying is the hydrogen solubility. In the α-phase, both decrease and increase in solubility is observed for different alloyant types. Specifically, reduction of hydrogen solubility in the α-phase occurs in contracted alloy systems, while the opposite takes place for expanded ones. This can be rationalized by different energetics exhibited by the two different alloys.[179,282,283] For contracted alloys, the interstitial sites are less favourable for the hydrogen as the sites are more "restricted". In contrary, an already expanded lattice lowers the barrier for interstitial sites to be occupied by hydrogen. In the β-phase, however, both types of alloys behave similarly in that they have lower solubility compared to the pure system. This has been rationalized by the fact that hydrogen atoms exclusively interact with Pd and therefore, in the alloyed system, the number of sites that hydrogen can occupy

reduces.[284] To this end, a linear relationship between the reduction of hydrogen solubility and alloyant content has been established.[185,284] Interestingly, the hydrogen solubility in the alloy is found to be exclusively dependent of the amount of Pd, regardless of the alloyant metal (for the coinage metals), even if several different alloyants are present (*e.g.* in the case of ternary alloys).[284]

4.2 Hydrogen Sensors

The ability of hydride-forming metals to dissociate and absorb hydrogen into their lattice makes them the central class of materials used for various applications such as hydrogen storage,[285] smart[286] and switchable windows,[287] metal hydride batteries[288] and hydrogen sensors.[8,26] Specifically for hydrogen sensors, their application is made possible by the dramatic changes in the physical and chemical properties (*i.e.* mechanical, electrical, magnetic, and optical) of the host metals under exposure to hydrogen.[289,290] For example, in the case of Pd, its resistivity increases when the hydride is formed, due to intensified electron scattering.[291,292] The electronic states of the hydride are also modified, as manifested for example via changes in the bulk dielectric function, where the absolute value of the real (ε_1) and imaginary (ε_2) parts reduces and increases, respectively (**Figure 4.6**). This modification translates to a change in optical properties (see **Chapter 2**), which, as of interest here, leads to a decrease and broadening of the LSPR frequency and line-width, respectively, for the case of Pd nanoparticles (see **Figure 2.3**).[26]

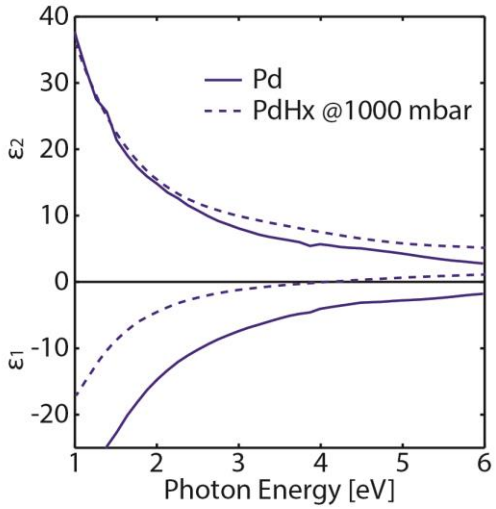

Figure 4.6. Real and imaginary parts of the complex dielectric function of Pd and Pd hydride. *Upon exposure to hydrogen, Pd transforms to Pd hydride. This process is followed by a change in its dielectric function in which the absolute value of the real (ε_1) and imaginary (ε_2) parts decrease and increase, respectively. The Pd and PdHx data are adapted from ref. 293 and 294 respectively.*

As one of the key enablers for the successful deployment of a hydrogen economy previously discussed in **Chapter 1**, hydrogen sensors using diverse transducing techniques have seen tremendous progress throughout the years.[8,20,25,26,29,30] Out of these, the two most popular transducing methods (both in lab-scale and commercial) are electrical and optical.[16] Both methods are relatively simple, easy to integrate into devices and low cost. Although in the case

of optical sensors, they offer a distinct benefit in that they do not pose any risk of spark generation, in contrast to electrical sensors, and thus they are considered to be safer. In such applications, Pd is the most common choice among the hydride-forming metals since it allows spontaneous dissociation of hydrogen molecules on its surface at ambient conditions, and because it absorbs large amounts hydrogen.[295] This makes Pd (and other hydride-forming metals) superior to sensors based on *e.g.* metal oxides that require operation temperatures of 300–500ºC.[8]

In the following sections I will discuss the development and current state-of-the-art of hydrogen sensors. To be in line with the theme of the thesis, and also motivated by the outlined advantages above, I will limit the discussion to hydrogen sensors based on hydride-forming metals. Even so, it is impossible to summarize all of the works available in the literature. Hence please consider the following section as my best effort to familiarize the reader with the topic, specifically with the strengths and limitations of present hydride-based hydrogen sensors.

4.2.1 State-of-the-Art in Hydrogen Sensors

The first demonstration of using hydride forming metals for hydrogen sensors dates back to 1972 when Maclntyr and Marshall used a Pd film and detected a change in the resistance upon exposure to hydrogen.[296] Not long after that, in 1975 Lundström et al. managed to fabricate a MOS transistor using Pd as the gate and showed that the threshold voltage correlates to hydrogen partial pressure. Impressively, already at this stage, a detection limit of 10 ppm was achieved.[297] These promising results led on to diverse hydrogen sensing architectures being developed in the 1980ies with highlights including the work of Butler et al. where they produced optical hydrogen sensors by coating a fiber and tracking the change in the fringe-patterns upon exposure to hydrogen.[298,299] However, due to the nature of *thick* Pd films being used, problems related to peeling and blistering (induced by volume expansion of Pd during hydrogenation) were very severe and invoked durability issues.[300]

As a response, in the 1990ies, a new hydrogen sensor family based on *thin* Pd films emerged. Upon hydrogenation, the film reflectance or transmittance changed accordingly, and were assumed to correlate linearly with the hydrogen concentration in the film, thus obeying the Beer-Lambert law (*i.e.* attenuation of light to the properties of material through which light is travelling). The development of fiber optic hydrogen sensors flourished in this decade as shown by the number of works published.[301–306] An interesting advance occurred in this period in that the surface plasmon resonance of the thin film started to be used as the readout.[303] This gave rise to better sensitivity compared to when a simple change in transmission or reflection was used.

In 2001, Penner and co-workers successfully fabricated Pd nanowires using electrodeposition.[307] They showed that such wires can be used as electrical hydrogen sensors that responded to 2% H_2 in outstanding 75 µs. The measured change in nanowire resistance occurred due to closing of microscopic gaps in the wires by the expanding Pd lattice during hydrogenation.[307,308] This impressive result (which now is still difficult to match) catalysed a new era of nanowire-based hydrogen sensors.[25] Notably, the key advances in nanowire hydrogen sensors have been mainly carried out by the same group, with the main goal of achieving fast sensors. To this end, efforts towards this goal include size engineering[309] and

heating of the nanowires,[310] as well as the utilization of hybrid materials such as Pd nanoparticles@carbon nanotubes,[311] Pd@Pt nanowires[312] and Pd nanowires coated by a metal organic framework (MOF).[313] The last two examples were done mainly to remove the competition from O_2 in air that reduces the sensor speed via consumption of hydrogen to form water in a catalytic reaction on the Pd surface.

The last decade has witnessed resurgence in the development of thin film optical hydrogen sensors mostly driven by the Griessen and Dam groups in The Netherlands. This development was facilitated by the establishment of the hydrogenography method[314] that allows the rapid optical screening of (complex) hydride materials for hydrogen detection.[60,315,316] Throughout the years, different classes of materials have been investigated, ranging from pure metals such as Mg,[280,317] Y[316] and Hf,[318] to alloys.[60,186,315,319–321] Notably, the response speed achieved in thin film optical sensors is still far slower compared to nanowire sensors due to size-dependent kinetics of the hydrogenation process. However, optical sensors offer unique readout capabilities in that the response to hydrogen can be translated into a change in sensor color that can be seen by the naked eye.[315,316,322,323] These sensors are attractive since they do not require electronics that otherwise are needed to convert and communicate the transduction signal. Hence, low-cost applications become possible.

Despite the extensive number of works related to the development of hydrogen sensors, meeting the performance targets presented previously in **Table 1.1** is still a huge and unsolved challenge. To illustrate this, **Table 4.1** shows the hydrogen sensing performance metrics of selected hydrogen sensors with various sensing mechanisms and architectures. I intentionally included vastly different sensors to demonstrate the extent of research and engineering that has been done in the quest to meet the strict requirements. While none of these sensors (and other sensors available in the literature, as recently pointed out by Penner[25]) meet all of the targets, some of them are able to reach individual or a few targets separately. Notably in the case of PdNi nanogap sensors, they achieve impressive 0.5 s for both response and recovery time at 2% H_2.[324] However its limit of detection (LoD) is somewhat high at 1000 ppm. On the other hand, a LoD of 20 ppm is reached by a hybrid Pd nanoparticle graphene hydrogen sensor. However, only with a long response time where the sensor reacted to 0.1% H_2 for as long as 1 minute.[325] Also commercial sensors available the market, which is dominated by electrical sensors, still fell short on the key performance targets by 2014.[29]

Apart from response time, there are at least two additional very important sensing properties that, however, are rarely discussed, or even addressed: hysteresis (and dynamic range) and assessment of performance in realistic environment including gases that may "poison"/deactivate the sensors. From the previous discussion, we have learned that pure Pd-based (and most of other hydride forming metals) hydrogen sensors features inherent hysteresis during hydride formation and decomposition (**Figure 4.5)**. This renders the sensor signal to not only depend on the current hydrogen pressure (as desired), but also on the *history* of the hydrogen pressure, *i.e.* on which branch of the hysteresis loop the sensor is. For an accurate hydrogen sensor with wide operating range, a one-to-one relation between the hydrogen pressure and the sensor readout is critical. Furthermore, Pd only shows a large response to a change in hydrogen pressure in its surrounding in a very narrow pressure range (*i,e.* around hydride formation and decomposition pressures) whereas at pressure ranges outside this narrow

Table 4.1 Hydrogen sensing performance metrics for selected Pd-based sensors from the literature.

Active Element[a]	Transducing Method	t_{90}[b] (s)	t_{10}[c] (s)	P[d] (mbar)	T[e] (^oC)	LoD[f] (ppm)	Background Gas	Ref
Pd@Pt NW	Electrical	2	2.5	40	103	4000	Air	312
Fractured Pd NW	Electrical	0.07	-	40	25	10000	N_2	307-308
Pd NP / Nanogap	Electrical	0.07	-	20	RT	25	N_2	326
Pd NR	Electrical	4	9	100	RT	20000	Air	327
PdNi Film	Electrical	20	100	40	22	-	Air	328
ZnO@Pd NW	Electrical	6.4	7.4	1	RT	100	Air	329
Pd NW	Electrical	12	-	40	RT	27	N_2	330
PdNi Nanogap	Electrical	0.5	0.5	20	RT	1000	N_2	324
Graphene @ Pd NP	Electrical	60[g]	20[g]	1	22	20	N_2	325
Pd NW @ ZIF-8	Electrical	13	6	1	RT	1000	Air	313
Pd Film on Fiber	Optical	10	-	40	RT	-	N_2	31
Au/SiO2/ Pd Film on Fiber	Optical	3	10	40	RT	5000	Ar	319
PdAu Film on Fiber	Optical	4.5	13	40	RT	-	N_2	332

[a]NP = nanoparticles, NR = nanoribbons, NW = nanowires. [b]Response time. [c]Recovery time. [d]Starting/end pressure for response and recovery time measurements. [e]Temperature at response and recovery time measurements. RT = room temperature. [f]LoD = limit of detection. [g]Measured as t_{50}.

region, the sensitivity is rather low. This is an unfortunate situation as, *e.g.*, the sensitivity at low pressure is most crucial when considering hydrogen leak sensors, since hydrogen becomes flammable at 4 vol. % (*i.e.* 40 mbar). Thus, pure Pd hydrogen sensors work well only if one needs to know if the hydrogen pressure has surpassed a certain pressure *threshold* (*i.e.* the plateau pressure). It is thus more suitable to be used as hydrogen *detector* rather than hydrogen sensor for continuous and real time monitoring of hydrogen concentration (**Figure 4.7**). When a "real sensor" is considered, the most ideal case would be to have a hysteresis-free system. Such a sensor will not only offer capabilities for dynamic sensing but also allows easy calibration by simple extrapolation.

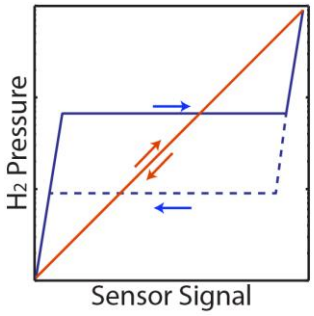

Figure 4.7. Hydrogen sensor response characteristics. *Typical pure metal hydride hydrogen sensors feature only large response at a certain hydrogen pressure across the hydride formation/decomposition plateau (blue lines). They also exhibit hysteresis, which is unwanted as it decreases the accuracy of the sensor readout and hampers their usage in a dynamic environment. Ideal sensor characteristics would be high sensitivity throughout a wide pressure range (red line) without hysteresis. Note that the relation between the pressure and the signal in a sensor can be of any form, although a linear relation is the most ideal.*

Since the above-mentioned problems are caused by the inherent properties of *pure* metal hydrides, a viable solution to circumvent these issues is the alloying of the hydride-forming metals with other elements to shrink the hysteresis. In fact, alloy thin film optical sensors using PdAu, PdAg and PdNi alloys have been demonstrated.[186–188,328,333] These sensors exhibit a complete suppression of hysteresis for alloy compositions above a critical value (typically > 25 at. %) and for the case of PdAu and PdAg also showcase higher sensitivities at low hydrogen pressures. Furthermore, these sensors also display faster response and recovery times. Beyond alloying with noble metals, recently Victoria et al. reached up to four-fold increased sensitivity in the low pressure regime by alloying MgNi with 28 at.% zirconium (Zr).[320] Finally, finding a new class of materials is also a viable option. Recently Boelsma et al. established the use of hafnium (Hf) as transducer for optical hydrogen sensors.[318] In their work, they showed that Hf responds linearly to hydrogen pressure spanning six orders of magnitude. Interestingly, the change in response towards hydrogen is constant regardless of temperature, promising a universal calibration curve. However, it requires high operational temperature of at least 90°C to reach the phase transformation that gives rise to the optical contrast used for the readout. Moreover, even at this temperature, the achieved response times are on the order of 20 s.

The second important aspect that is rarely addressed in the literature on hydrogen sensors is their performance in more realistic conditions that contain *e.g.* humidity and trace gases that may poison/deactivate the sensor. This factor is important as Pd (either used as main

transducing material or as catalytic agent to dissociate the hydrogen in "capping layers") can be readily deactivated (*i.e.* loss of functionality) when exposed to gases such as carbon monoxide (CO), sulfuric compounds, hydrocarbons and nitrogen dioxide (NO_2), even at trace amounts.[19,20] This may prevent Pd-based sensor application not only when the presence of a poisoning gas, such as CO, is inevitable, *e.g.* during syngas production,[334] but also at ambient conditions due to its natural occurrence in air (*ca.* 0.2 ppm), and at higher concentrations close to large point sources or in urban areas.[28]

From the few attempts to overcome these problems available in the literature, two main strategies can be categorized. The first solution again is related to material design, while the second solution employs the use of a coating layer to act as a "molecular sieve" that, ideally, only is permeable to hydrogen gas. Interestingly, these two solutions are rather commonly used in the field of hydrogen purification systems, but somehow still rarely adapted in hydrogen sensors.[176,335] For the first solution, alloying Pd has been shown to reduce the poisoning degree, especially towards CO. This can be understood by modification of the surface that leads to weaker interactions between the poisoning gas molecules and the Pd surface atoms.[190–194,336] This effect was demonstrated by Zhao et al. who used a PdAu alloy thin film as optical sensor.[333] They showed that an increased Au content in the film reduces the extent of deactivation towards 100 ppm CO. Although the readout signal was fully retained, even at 40 at.% Au content, the response speed was 10 times slower. For this purpose, Cu is actually a better alloyant than Au. As has been shown experimentally for hydrogen purification systems and also theoretically, Cu weakens the Pd-CO interactions even at relatively low amount.[194,336] However, to the best of my knowledge, there is no report on using PdCu alloys as hydrogen sensors.

Applying coating layers has also been shown to hinder unwanted molecules from adsorbing on the Pd surface. A prominent example stems from Hong et al., who coated 200 nm PMMA polymer onto a hybrid Pd nanoparticle/graphene sensor and showed that CO, NO_2 and CH_4 are completely blocked from interacting with the nanoparticles.[337] Prior to that, PMMA has also been employed to protect Mg nanoparticles from oxidation by effectively sieving O_2 from air.[338] Very recently, MOFs have also been used as O_2 sieving layer by Koo et al.[313] Specifically they used ZIF-8 and achieved significant increase in sensor response speed. They rationalized the speed-gain by efficient O_2 sieving, which otherwise would block the Pd surface and scavenge the hydrogen to form water.[339] Lastly, a hydrophobic PTFE (*i.e.* teflon, the same material used in non-stick frying pans) coating has also been used, mainly to repel water for intended sensor use in humid environment.[278,315,316]

Interestingly, another common benefit can be seen in these different works, which employ different types of coating materials. For all cases, an enhancement in absorption and desorption kinetics is observed, regardless of measurements being carried out in air, N_2 or *pure* H_2 environment (see work by Li et al. where they coated Pd nanocubes with HKUST-1, a type of MOF).[313,340–342] Thus there seems to be a generic effect taking place at the interface of the sensing and coating materials, which gives rise to faster sorption processes. So far, a few explanations have been offered, such as the modification of surface electronic states,[342,343] physical force/stress imposed by the coating layer,[343] chemical modification of the surface[340,341] and, as mentioned above, the removal of competing molecules reacting on the surface.[313]

To conclude this section, it is clear that development in hydrogen sensors has vastly advanced throughout the last decades. The emergence of novel sensing platforms and materials has brought hydrogen sensors to the performance they can achieve today, that is, being safer, faster, more sensitive, durable and efficient. Nonetheless, none of the existing solutions meet all of the performance targets and a breakthrough is needed. Ideally, a platform that can combine all of the strategies discussed above should be developed, such that the "ultimate hydrogen sensor" can be realized.

4.2.2 Nanoplasmonic Hydrogen Sensors

As discussed in **Chapter 2**, nanoplasmonic sensors[31] are characterized by high sensitivity, possible miniaturization down to the single nanoparticle level and fast response. Owing to these promising properties, nanoplasmonic sensors have expanded their territory in many different research fields, including hydrogen detection.[26] To this day, 10 years since the first seminal work based on Pd nanodisks,[52] nearly 100 publications related to nanoplasmonic hydrogen sensors have been published. However, since the field is still relatively young, only very few works, if any, actually perform a meaningful and complete characterization related to the key hydrogen sensing metrics (*i.e.* speed, sensitivity etc). Many of the works can be considered either as fundamental in nature or exploratory work.

In the first case, nanoplasmonic sensing has been widely used to gain deeper understanding of the hydrogen storage properties in metal nanoparticles. Efforts on this direction include scrutiny of size- and shape-dependent kinetics and thermodynamics in small Pd nanoparticles.[147,153,243,247,266,344] Recent advances have pushed the ability of nanoplasmonic sensing further in the direction of single particle studies. The first successful experiment was done by Liu et al. where they followed the hydrogenation process of small Pd particles by placing a Au antenna nearby (the indirect plasmonic sensing method, as described in **Chapter 2**).[55] Almost at the same time, Shegai and Langhammer also studied in rather similar fashion the hydrogenation process in single Pd and Mg nanoparticles.[151] To this end, several other works have reported successful studies on single Pd nanoparticles and are considered to contribute significantly towards the fundamental understanding of hydride formation in nanoscale systems.[56–59]

On the other hand, there are also a lot of exploratory studies reported for nanoplasmonic hydrogen sensors with more of an application focus. This is a natural step for a new field and is an important one in order for the field to grow. This aspect of work covers many different directions. There is a significant effort to find novel hydride plasmonic elements in terms of materials such as Mg[105] and Y[100], as well as in terms of nanoparticle sizes and shapes. To this end, differently shaped nanoparticles such as nanodisks,[52] nanorings,[153] bipyramids,[53] nanocubes,[342,345] and core-shell structures[54,58] have been utilized as plasmonic hydrogen sensors.

Another direction taken by many researchers is to enhance the sensor sensitivity. In this regards, nanoplasmonic sensors exhibit quite unique capabilities in that their sensitivity is tunable. Since their readout, the LSPR peak (see **Chapter 2**), is basically a far-field optical "effect", it can be "manipulated" in several ways. One of the straightforward ways is to utilize nanoparticles that give rise to an LSPR peak at longer wavelengths, as it correlates with sensitivity. As discussed

in **Chapter 2**, this can be done by having bigger particles or particles with sharp features. This was recently demonstrated by Yip et al. where their bipyramid Pd nanocrystals feature a LSPR shift up to 90 nm upon hydrogenation.[53] Another way to engineer the optical response is by controlling the arrangements of the nanoparticles. This is nicely shown by Yang et al. by putting active Pd nanoparticles close to an arrangement of Au nanoantenna.[346] In this way, coupling between particles occurs, which leads to up to 5 times higher signal change upon hydrogenation. Recently, Matuscheck et al. showed that following the light polarity change in chiral nanostructures resulted in higher sensitivity compared to the common change in extinction or reflection.[61]

At this point it is clear that nanoplasmonic sensors have provided glimpses of their potential capability that can be exploited for the realization of high-performance hydrogen sensors. Learning from previous discussions, one of the keys towards achieving this goal is to implement alloy particles as transducing materials. This is the contribution made by this thesis, where I have developed nanoplasmonic alloy hydrogen sensors and characterized their sensing metrics.

5 Nanofabrication

With *"nano"* preceding the word fabrication one should expect an unconventional and fascinating way of how nanofabrication works. After all, the end products are expected to have a dimension nearly a millionth time smaller than an eye of a needle. In the past few decades we have seen the establishment of nanofabrication that relies on various unique physical and/or chemical principles. It is these nanofabrication capabilities (and the corresponding characterization) that have enabled the unprecedented progress in nanoscience and nanotechnology. The work presented in this thesis is a direct consequence of and has been facilitated by state-of-the-art nanofabrication. All the sensors comprising plasmonic nanostructures developed and studied in my project were fabricated using a method called Hole-mask Colloidal Lithography (HCL).[347] There is a number of different thin film deposition and etching techniques involved in the HCL process. This Chapter deals with the physics and concepts behind each of the used techniques (some of them are surprisingly simple!), their utilization, and their specific usage for the work included in this thesis. The Chapter ends with a detailed discussion of the HCL process, how it can be used to produce various nanostructures and a method to transfer the fabricated nanoparticle arrays onto arbitrary surface.

5.1 Spin Coating

Spin coating is one of the most common procedures for applying thin films to a flat surface and is used in a wide range of industries and technology sectors. The advantage of spin coating is its ability to rapidly and easily produce uniform films from a few nanometers to a few micrometers in thickness over a surface. Spin coating is mostly utilized to cast thin films of polymers from a solution.

Spin coating involves the rapid acceleration of a liquid "puddle" deposited on the substrate of choice, followed by high-speed rotation. The rotation spreads the solution/suspension evenly over the substrate to eventually form a uniform thin film on the entire substrate. The balance between the centrifugal force introduced by the rotation and the viscous force of the polymer solution, which is determined by the solution concentration, dictates the achieved film thickness. Of the many factors that seem to affect the obtained film thickness, only the spinning speed and solution viscosity actually do.[348] This promises a highly reproducible technique to deposit thin polymer films. Spin coating is commonly followed by baking of the sample, *i.e.* the sample is heated on a hot plate or inside an oven to evaporate the excess solvent and thereby solidify the thin film. A schematic illustration of the general spin coating steps is depicted in **Figure 5.1**.

For the purpose of this thesis, spin coating is used as the first step of the HCL process to deposit a thin (~280 nm) poly(methyl methacrylate) (PMMA) polymer film. Moreover, I also used spin coating to deposit a PMMA film as coating layer for the plastic-plasmonic hydrogen sensors developed in **Paper V**.

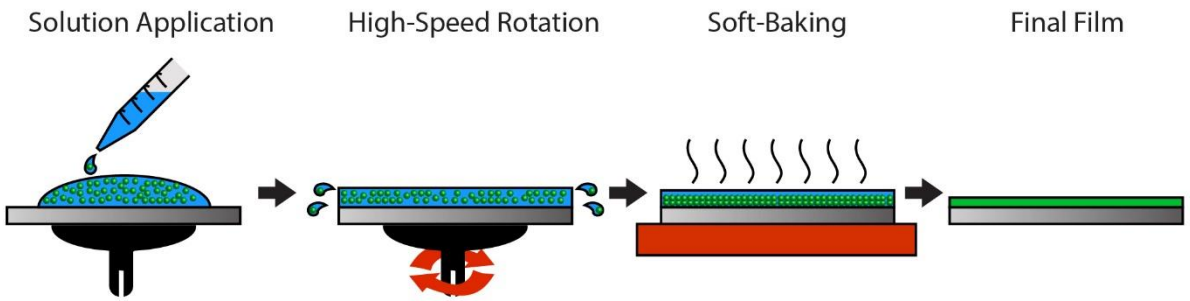

Figure 5.1. Spin coating. *An excess of polymer solution is pipetted onto the substrate followed by high-speed rotation, which induces centrifugal forces that throw excess solution off the edges to achieve a homogeneous film thickness. Soft baking is done to evaporate excess solvent to obtain a solid polymer film as the end result.*

5.2 Plasma Etching

Plasma is one of the (rather unfamiliar) states of matter along with gas, liquid, and solid. A plasma has very similar characteristics with gas (*i.e.* it does not hold any shape or volume unless contained) except that it consists of a *mixture* of electrons, ions, neutral atoms and molecules. The number of charge carriers in the plasma makes it electrically conductive and hence it is strongly influenced by the presence of electromagnetic fields. These unique properties of plasma are what define it as one of the states of matter. In short, plasma is an *ionized gas*.

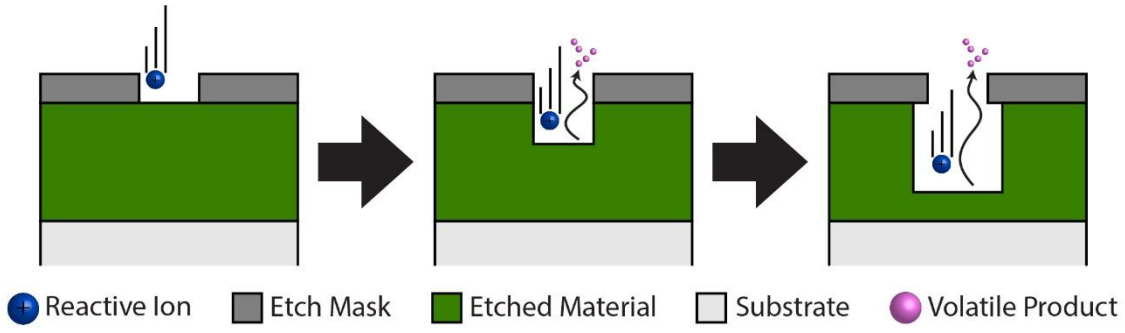

Figure 5.2. Chemical plasma etching. *In a chemical etching process reactive-ions created in the plasma are accelerated towards a material and form volatile products. The process is highly one-directional and thus creates a high degree of anisotropic etching. However, prolonged etching creates undercuts below the etch masks and thus the chosen etching duration should be carefully adjusted.*

When building nanostructures, both addition and removal of material are mandatory steps required to achieve the desired designs. Interestingly, in nanofabrication, plasma can act as both

agents. A term called *etching* is commonly used for the removal of material in nanofabrication. When high-energy ions in a plasma hit a surface a transfer of energy occurs between the impinging ions and the atoms on the surface, causing the atoms to be "kicked out"; a purely physical process defined as *sputter etching*.[349] On the other hand, one can also use a gas that chemically reacts with the materials and forms volatile products; a *chemical reactive ion etching* procedure,[349] see **Figure 5.2**. In this thesis, chemical reactive ion etching is used to etch through the PMMA mask anisotropically during the HCL process. PMMA consists predominantly of carbon and hydrogen and it can therefore be reactively etched using oxygen plasma (*i.e.* O_2^+) forming volatile CO, CO_2, and H_2O. Additionally, short-time interaction of the plasma with the polymer surface has been reported to increase its hydrophilicity by changing its surface[350,351] and thus it has been utilized to PMMA at the beginning of the HCL process as well as to PTFE in order to enable PMMA spincoating on it for the tandem configuration explored in **Paper V**.

5.3 Thin Film Deposition

Deposition of thin films is one of the central processes in nanofabrication and a number of different methods exist for this purpose. In general, the techniques can be divided into physical or chemical deposition methods. Below, I give a brief overview of the deposition methods employed in this thesis.

5.3.1 Physical Vapor Deposition

Physical vapor deposition (*PVD*) is based on the evaporation of the intended film materials by means of, as the name suggests, purely physical processes such as sputtering and thermal evaporation, and is carried out in vacuum. The vapor of the desired material will condensate upon reaching the sample surface, which is placed on the opposite side of the evaporation source, and form a thin film (or small islands of particles, depending on the amount of material evaporated) while retaining its original composition. The vacuum environment used in the process is critical for the quality of the deposited films, as well as for the deposition process to occur at all. High vacuum provides a longer mean free path for the vapor constituents. This is necessary to enable them to travel the long distance to the sample, as well as to reduce the probability of contamination of the grown film.

In this thesis I have used two types of PVD namely sputtering and evaporation. In sputtering, atoms of a target material are displaced *via* "physical force", that is, by bombarding them with high energy ions (**Figure 5.3**a). In this case argon ions (Ar^+) are widely used due to their large mass and inertness. The latter ensures pure materials to be deposited on the substrate. Sputtering is done using plasma in a similar way as described above for the plasma etching.

On the other hand, evaporation uses a simple trick to create a material vapor: heating to high temperature in vacuum. In fact, thermal evaporation of a solid offers a much higher vaporization rate as compared to sputtering.[352] The way to heat the target material varies but the common methods are resistive and electron beam heating. In this work, electron beam heating has been used.

In the electron beam method, the target material is heated by bombarding it with a beam of high-energy electrons discharged from a tungsten filament, as shown in **Figure 5.3**b. The transfer of momentum from the electrons of the beam directed onto the source material creates thermal energy, which vaporizes the target. The electron beam heating approach possesses an ability to focus on a small spot to provide high local heating. This provides both an extreme range of evaporation rate and the ability to vaporize materials with very high melting or sublimation temperature (*e.g.* tungsten, carbon, etc.).

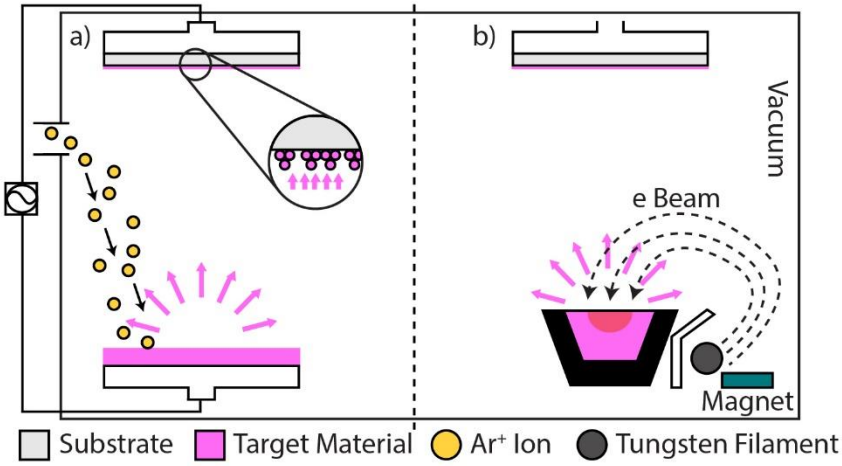

Figure 5.3. Sputtering and electron beam evaporation. *(a) Thin film deposition via sputtering relies on bombardment of the target material by high energy ions e.g. Ar^+. The atoms leaving the target travel towards a sample surface where they condensate into films. (b) In electron beam evaporation, a high DC voltage is applied to a tungsten filament that causes electrons to be emitted. These are then directed by the magnetic field towards the target material. The stream of electrons heats and in turn vaporizes the target. In both cases vacuum conditions are required to minimize contamination and guarantee long enough mean free paths for the species to be able to reach the substrate, as well as for the vapor pressure above the source to be high enough for evaporation.*

In both sputtering and evaporation methods, the rate of deposition and the final film thickness is monitored using a quartz crystal microbalance (QCM) crystal. Current state-of-the-art evaporation systems allow control of the deposition at the sub-Ångström level. This assures a reliable and reproducible deposition at a very high level of accuracy and is thus an important feature when designing nanostructures with demanding precision on dimensions and composition (see for example **Paper I**). In this thesis, electron beam evaporation was used to deposit various metals (*i.e.* C, Cr, Au, Ag, Cu, Pd) during the HCL process including deposition of the plasmonic nanostructures. Sputtering was used to grow the thin polytetrafluoroethylene (PTFE) film studied in **Paper V** and was done by our collaborator at Delft University of Technology in the Netherlands.

5.3.2 Chemical Vapor Deposition

Chemical vapor deposition (*CVD*) relies on reactions of volatile compounds of materials to be deposited to produce a "new" solid (*i.e.* the reaction product) that condensates on the (usually) heated surface of a substrate. Naturally, the CVD process is subjected to thermodynamic and kinetic limitations, which makes it a generally a more complex process than PVD. There are many factors that have to be precisely controlled in order to achieve the desired thin films, such as temperature and reactants. The process is also constrained by the flow of gaseous reactants and products. A simple schematic illustration generally describing the CVD process is shown in **Figure 5.4**.

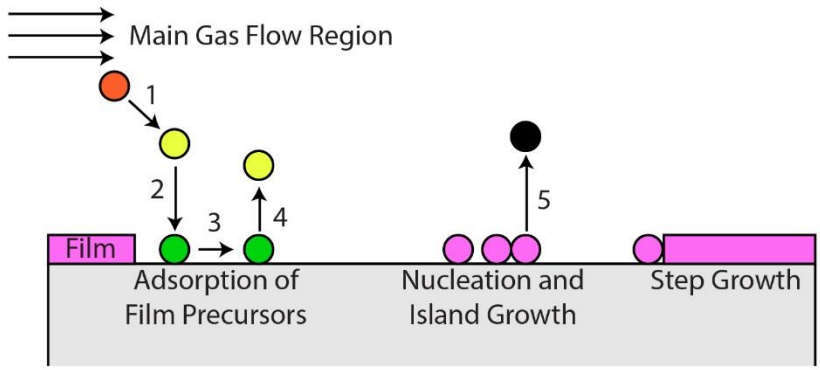

***Figure 5.4. Sequence of gas transport and reaction processes contributing to CVD film growth**. In CVD, the gas reactants are transported via diffusion to the reaction zone where they react chemically to produce new reactive species and by-products (1). Both types of species are then transported towards the surface (2) at which they chemi- or physisorb and diffuse (3) until a heterogeneous reaction, catalyzed by the surface, initiates and leads to the formation of the desired film. During the process, there is also desorption of species (4) and by-products (5) which are transported away from the surface by the flow from the reaction zone. The figure is adapted from* [353].

As PVD is a directional deposition method, it is not able to cover surfaces that are not facing the source. In contrast, for CVD, the film is deposited wherever the gas reactants can get adsorbed on the surface. This particular distinctive signature outweighs the PVD process. A comparison between PVD and CVD is shown in **Figure 5.5**.

In this project, I used plasma-enhanced CVD (PE-CVD), a variant of CVD, which employs a plasma, along with the reactive gas, whose ions provide extra energy to initiate the endothermic process so that less heating is required. Specifically, I deposited dense silicon dioxide (SiO_2) on QCM crystals in the experiments to quantify the amount of hydrogen absorbed by our nanoparticles (details in **Chapter 6**). The SiO_2 film acts as a spacer layer to control the optical coupling between the Au electrode on the crystal and the fabricated nanoparticles. Moreover, I also used silicon nitride (Si_3N_4) as coating material for the INPS sensors used in **Paper VIII**, as a means to achieve homogeneous surface chemistry.

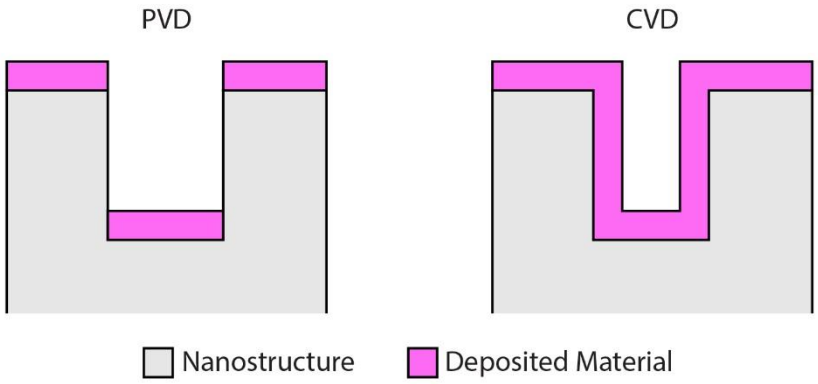

Figure 5.5. The difference of achievable step-coverage between the PVD and CVD methods. *PVD (left) is a directional deposition process. Surfaces parallel to the vapor trajectory cannot be covered, resulting in deposition only on surfaces facing the evaporation source. Hence PVD is a perfect choice whenever one wants to fabricate a structure based on mask-pattern transfer. On the other hand, CVD (right) depends on the volatile compound's diffusion (which ideally can go anywhere) so that the deposition covers all surfaces, creating very conformal coverage. Thus, CVD is suitable for coating purpose.*

To achieve these, silane (SiH_4) gas is used as precursor for both SiO_2 and Si_3N_4 deposition following these reactions:

$$SiH_4 + O_2 \rightarrow SiO_2 + 2\,H_2 \quad (4.1)$$

$$3\,SiH_4 + 4\,NH_3 \rightarrow Si_3N_4 + 12\,H_2 \quad (4.2)$$

5.4 Hole-Mask Colloidal Lithography

Colloidal Lithography (CL) is a self-assembly-based nanofabrication technique, which uses nanoparticles synthesized via wet chemistry (*i.e.* emulsion polymerization or sol-gel synthesis) as building blocks for the self-assembly of a template for further nanofabrication.[354,355] Upon the deposition of, typically, nanospheres onto a substrate of choice, a pattern will be formed due to the self-assembly, in most of the cases controlled by electrostatic forces. The gaps in between or even the nanospheres themselves are then used as an etch- or evaporation mask. The method allows precise control of the final structures parameters (*i.e.* size, distribution, separation) by simply adjusting the colloidal particle size, separation and processing conditions.[356,357] The nature of the self-assembly process also allows the method to be able to produce 2D or 3D arrays on large surface areas. Despite its versatility, CL does not require complicated methods and tools; a very cost-effective nanofabrication method. These astonishing advantages are the reason why colloidal lithography is widely used, especially in the nanoplasmonics field, to fabricate arrays of plasmonic structures.[168,355,357,358]

With the background of some basic processes used in nanofabrication in place, we can now discuss the main fabrication technique I used to produce all plasmonic samples developed and utilized in this thesis, *i.e.* Hole-mask Colloidal Lithography (HCL).[347] HCL is a variant of colloidal lithography and thus is capable of creating amorphous arrays of nanostructures on

large surface areas (cm^2 scale). The key feature of HCL is the usage of a sacrificial polymer layer as deposition hole-mask. This simple addition proves to be a very powerful aspect since HCL is able to produce a wealth of different types of (multicomponent) nanostructures by simply depositing the desired materials through the mask as is or by tilting and/or rotating the sample stage.[168,357–360]

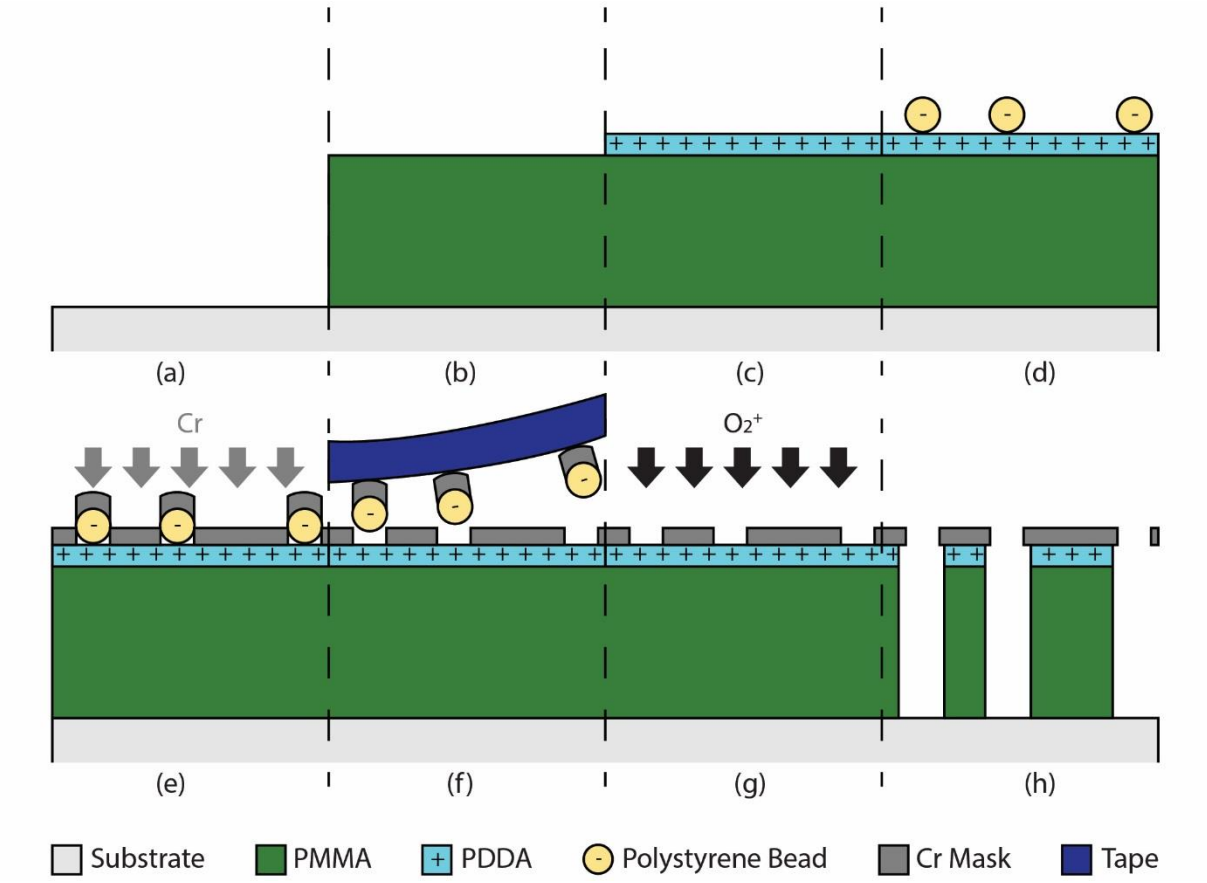

Figure 5.6. Schematic depiction of the fabrication steps in Hole-mask Colloidal Lithography nanofabrication. *(a) A cleaned substrate, e.g. glass, silicon, QCM crystal or TEM window, depending on the intended use, is the starting point. In steps (b) to (d) PMMA is spin-coated onto the substrate, followed by positively charged PDDA and negatively charged polystyrene particles, respectively. (e) Illustrates the chromium deposition to form the mask from the electrostatically self-assembled PS particles on the PMMA. Prior to the plasma etching in (g), the chromium-mask-covered PS particles are stripped away using tape (f), leaving an "unprotected" area of the PMMA, which later is etched all the way down to the substrate as shown in (h). At this step, a deposition mask is created, which can be used to produce multiple nanostructure arrangements depending on the specifics of the final evaporation step.*

Figure 5.6 displays a schematic of the HCL process. Unless stated otherwise, later in the appended papers, all parameters in the HCL fabrication are kept the same throughout the whole thesis as follows: Flat substrates, either borofloat glass, silicon wafers, QCM cyrstals or TEM windows, depending on the intended use, are cleaned (by sonication agitation for the case of glass and silicon substrate and only by rinsing for TEM windows in order not to break the membrane) in acetone, isopropyl alcohol (IPA), and deionized (DI) water, respectively, for

three minutes each to remove organic contaminants. Prior to the self-assembly step, PMMA is spin coated (2000 rpm, 30 s, produces thickness of roughly 280 nm) and soft-baked (170 ^{o}C, 5 min) (**Figure 5.6**b), and then ashed for 5 s in oxygen plasma (50 W, 250 Torr, 10 sccm) to increase hydrophilicity. This step is done in order to avoid spontaneous de-wetting during subsequent application of polyelectrolyte and colloidal particles. Subsequently, a thin layer of poly (diallyldimethylammonium chloride) (PDDA) is applied onto the surface for 40 s and thereafter rinsed with DI water for 20 s, and blown dry with N_2. After this step, a monolayer of positively charged PDDA is adsorbed (**Figure 5.6**c). An aqueous suspension of oppositely charged polystyrene (PS) nanobeads is then pipetted onto the substrate and incubated for three minutes. The PS particles will adsorb on the PDDA due to electrostatic forces at *ca*. 10-15% of a monolayer surface coverage. Electrostatic repulsion is also responsible for the self-assembled arrangement of PS particles. It prevents their aggregation and results in a pattern of particles with edge-to-edge distances on the order of one PS particle diameter or larger with no long-range order (**Figure 5.6**d). This step is followed by careful rinsing under DI water to remove the excess solution and then by N_2 blow-drying. The rinsing helps to avoid rearrangement of the particles, which otherwise can be induced by capillary forces during drying. Fifteen nanometers of Cr are then thermally evaporated by electron beam evaporation (5 x E10^{-7} Torr base pressure, 1 Å/s deposition rate) as a mask (**Figure 5.6**e). In this state, the sample can be kept for long periods without any deterioration. The chromium-covered PS particles are then stripped away resulting in "holey" Cr films with the hole diameter being defined by the PS particle size (**Figure 5.6**f). Subsequently, the samples are exposed to oxygen plasma etching (50 W, 250 Torr, 5 minutes, 10 sccm) (**Figure 5.6**g) leading to the creation of the final hole-mask, which can be used to produce the desired nanostructures by simply depositing materials through it (**Figure 5.6**h).

An important feature of this method is that the evaporated materials will build up on top of the mask and at the rim of the holes in the mask, eventually causing the hole to shrink. This effect generates a tapered structure of the nanoparticles grown on the substrate through the hole of the mask. However, with clever strategy, this feature can be utilized to create various complex arrangements of nanoparticles.[168,359]

5.4.1 Nanodisk Structures

Once the evaporation mask has been produced by HCL, it is straightforward to fabricate an array of nanodisks on a surface. The sample is loaded in an electron beam evaporation system and the material of choice is deposited through the hole-mask (**Figure 5.7**a). After the evaporation, the sample is dipped in acetone to dissolve the PMMA layer and remove the mask from the sample. After this process, commonly known as "lift-off", only the nanostructures remain on the sample surface (**Figure 5.7**b).

As discussed before, the successive closing of the hole-mask during material deposition will create tapered structures with a specific closing angle. This angle depends on the deposited material *e.g.* for Au, a closing angle of 60^{o} has been reported.[144,347] An example of an array of Au nanodisks with diameter and height of 190 nm and 20 nm, respectively, fabricated by HCL is shown in **Figure 5.7**c and d. Note that a minor size variation exists for the fabricated

nanodisks, which is caused by the intrinsic polydispersity of the PS beads used during the HCL process (**Figure 5.7**e). In this thesis, Au nanodisks are used as plasmonic entities in **Paper VIII**.

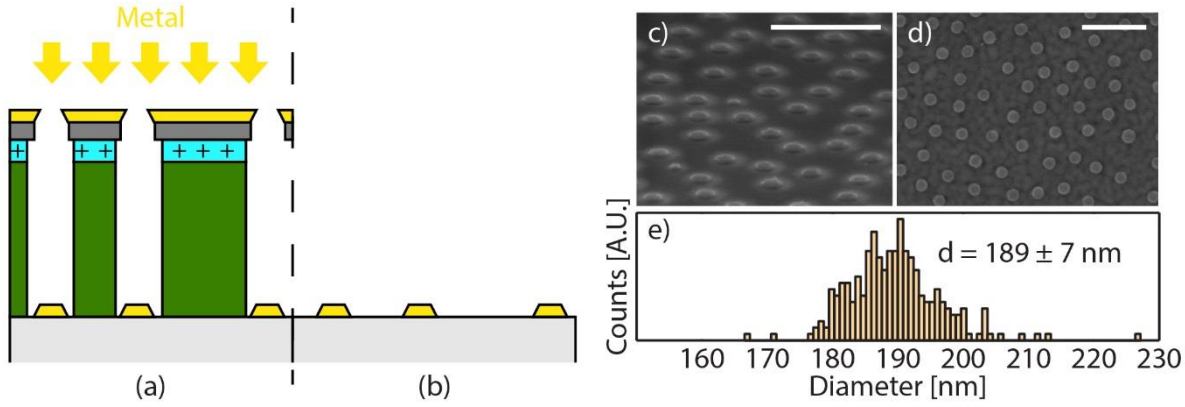

Figure 5.7. Fabrication of nanodisk structures using HCL. *(a) PVD-deposition of the material through the mask. Due to the successive build-up of material on top of the mask and at the rim of the hole, the diameter of the hole shrinks gradually, creating a tapered structure inside the hole. (b) Removal of the PMMA mask is done by dissolving the PMMA resist layer in acetone, leaving only the nanodisks on the sample surface. (c) 70º tilt angle and (d) top-view SEM images of an array of gold nanodisks with mean diameter of 190 nm and height of 20 nm. Note the quasi-random arrangement of the nanodisks. (e) Diameter distribution of fabricated nanodisks. Note that the polydispersity in size is "inherited" from the polystyrene beads used during the fabrication to create the hole-mask.*

5.4.2 Layered Nanodisk Structures

In **Paper I** we established a bottom-up fabrication strategy for arrays of metallic alloy nanodisks for use in nanoplasmonics and in plasmonic hydrogen sensing, the main subject of this thesis. The central idea behind the fabrication is to deposit layers of alloy constituents and anneal them at high temperature to induce alloying. Fabrication of multilayer nanodisks is as straightforward as the fabrication of nanodisks comprised of a single element discussed previously. The sample is loaded into an electron beam evaporation system with *different* sources. This allows successive deposition of the materials without taking the sample out. The procedure makes the whole process more effective and also eliminates the risk of contamination between the layers. As discussed before, the hole-closing of the HCL mask during deposition means that the diameter of the disk on top will be smaller than the one below. This should be considered when calculating the amount of material needed when designing certain alloy compositions. To this end, simple geometric considerations concerning the nominal diameter, height and taper angle of the nanodisk is sufficient to achieve the targeted alloy compositions with excellent accuracy.[106]

Another critical aspect to be considered is the gas environment during annealing. If the alloy includes elements prone to oxidation, annealing in inert or even reducing atmosphere is necessary to retain the metallic state of the nanoparticles. **Figure 5.9**a shows an example of what happens when alloy formation of PdAu is induced by annealing in air. During annealing,

the Pd was oxidized and formed a thin PdO shell. This shell was maintained throughout the process and consequently core@shell PdAu@PdO nanoparticles were produced at the end. Although the PdO shells can be quickly reduced back to Pd by flushing with hydrogen gas (**Figure 5.9**b), the core@shell nanoparticle configuration remains and therefore a homogeneous alloy formation is not accomplished. For all the work reported in this thesis, all samples were thus annealed under constant 4% H_2 flow and therefore they formed fully homogeneous alloys.

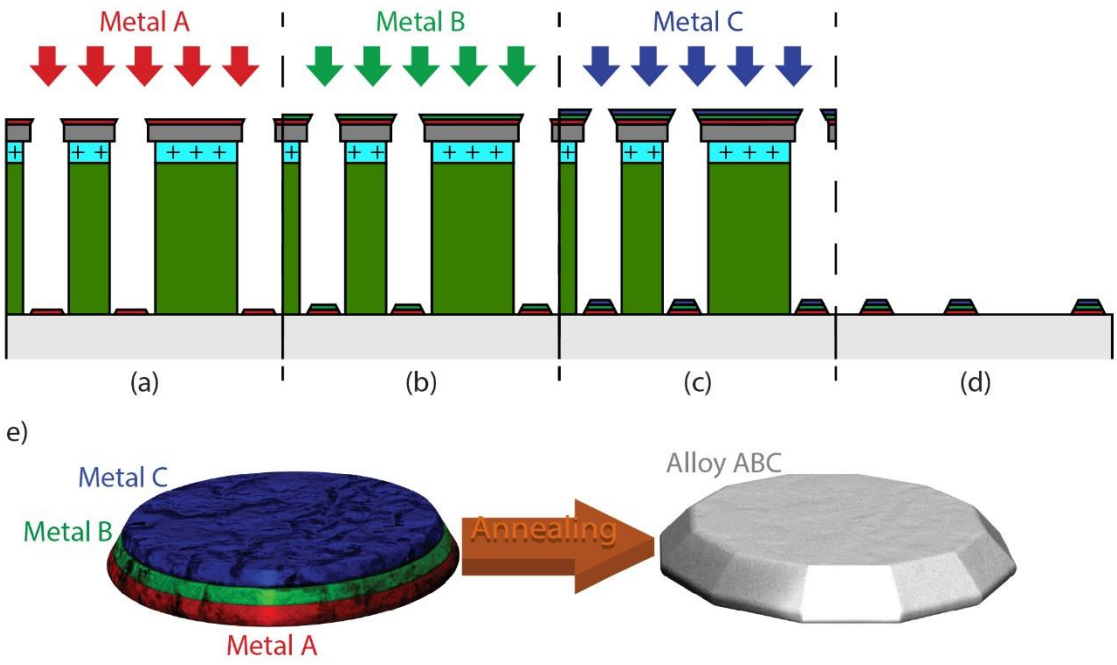

Figure 5.8. Fabrication of stacked nanodisks with multiple metals using HCL. *(a) to (c) show the successive deposition of different metals to form the layered nanodisks. The diameter of sequentially deposited disks shrinks due to the closing of the mask. (d) Removal of the PMMA mask leaves layered nanodisks on the substrate. (e) Schematic depiction of the alloy formation process where the layered nanodisk is annealed at high temperature for a certain duration dictated by the specific alloy to be formed. The schematic is adapted with permission from ref. 106. Copyright 2016 American Chemical Society.*

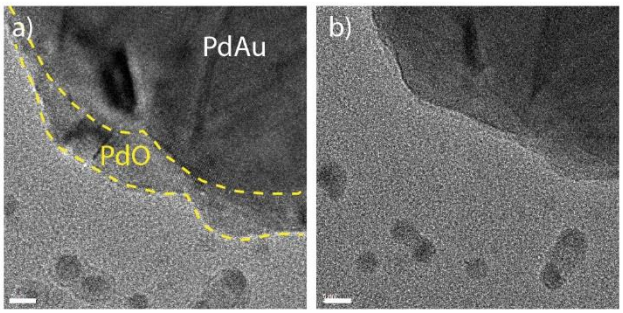

Figure 5.9. Palladium oxide shell formation during annealing in non-reducing gas environment. *(a) A PdO shell (yellow dashed lines) was formed during PdAu alloy fabrication when the annealing step was done in air. (b) Similar nanoparticle after exposure to 5 mbar hydrogen, which effectively reduces the oxide shell to metallic Pd.*

5.4.3 Pattern Transfer via Sacrificial Etch Layer

Up to this point, the HCL process described above was done directly on the target substrate. In some cases, *e.g.*, where the substrate is small and fragile (*e.g.* TEM windows) or not flat, the fabrication process can be really challenging if not impossible. A clever strategy was recently developed by Lodewijks et al.[361] to seamlessly transfer lithographic nanostructures onto another arbitrary substrate of choice (even if it is not flat). The idea is to employ a subsequent sacrificial and a thin (~10 nm) carbon (C) layers as support for the nanostructures (**Figure 5.10**a). The sacrificial layer should be chosen so that it can be removed exclusively without affecting the fabricated nanoparticles and other present elements. On the other hand, C is used as support layer since it provides structural integrity while being flexible; so it can fully adapt to a curved surface. Furthermore, C can be efficiently removed by *e.g.* oxygen plasma. The general steps for the pattern transfer are shown in **Figure 5.10**. In one specific example of using Cr as the sacrificial layer, the parent substrate is dipped in Cr etchant, detaching the C film with the nanostructures (**Figure 5.10**b). Next, the substrate is transferred to DI water. Since C is hydrophobic, it will readily float up to the water-air interface (**Figure 5.10**c). The host substrate can then be used to pick up the floating C film and complete the transfer process. Once dried in a N_2 stream, the C can be easily removed by oxygen plasma (**Figure 5.10**d), leaving the nanostructures in direct contact with the host substrate (**Figure 5.10**e).

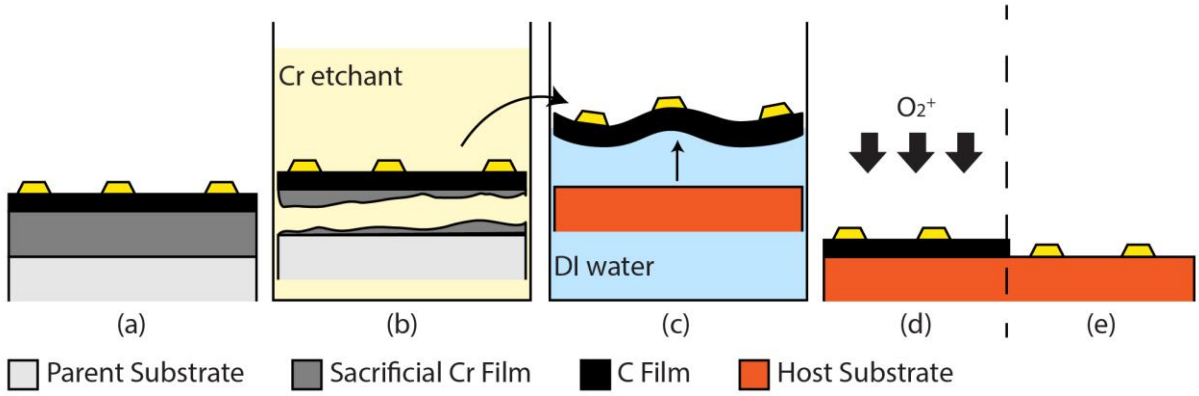

Figure 5.10. Pattern transfer of HCL-fabricated nanostructures to a host support. *(a) To facilitate pattern transfer, a sacrificial Cr and transfer C layer are deposited before fabrication of nanostructures. (b) Removal of the Cr layer by submerging it in Cr etchant. Once removed, the C layer is transferred to DI water where it will reside at the water-air interface due to its hydrophobicity (c). The free-floating C layer can then be picked up by a host substrate. (d) To remove the C layer, oxygen plasma is utilized, leaving nanostructures placed directly on the host substrate (e).*

In this thesis, HCL-fabricated nanodisk arrays were transported to a fiber to realize the integrated fiber-optic nanoplasmonic hydrogen sensors discussed in **Paper VI**. The transfer process of fabricated alloy nanoparticles to a fiber is relatively straightforward. However, one of the challenges that often occurs is the problem with "crumpling" in which the transferred C layer folds on itself and wrinkles. It is worth noting that imperfect transfer does not affect the sensing functionality of the fiber. Nonetheless, to avoid this problem, properly adjusting the overall dimension of the fabricated nanoparticle array is important. Often, during removal of

the Cr sacrificial layer, the C film breaks into a few small pieces and thus convenient flake sizes are available. In the case of a successful transfer process, a conformal film is obtained (**Figure 5.11**c and d). All of the fabrication related to the fiber-optic sensors included in this thesis were performed by my colleague Robin Eklund, who I supervised during his master thesis.

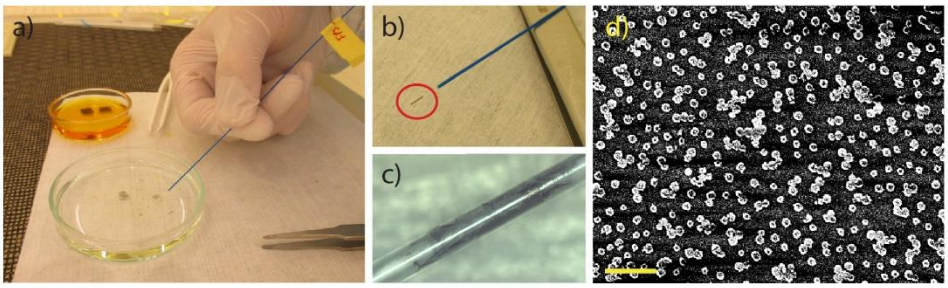

Figure 5.11. Transfer of a nanodisk array onto an optical fiber. *(a) The C layer is picked up by a fiber. (b) C layer with the nanodisks, which resides conformally on the fiber (red circle) after drying. (c) Optical microscope image of the fiber decorated with the nanodisks array after C layer removal by oxygen plasma. (d) SEM image of the nanodisk array on the fiber. The scale bar is 1 µm.*

5.4.4 Indirect Nanoplasmonic Sensing Chips

Indirect nanoplasmonic sensing (INPS) samples are used in **Paper VIII**. The fabrication of this type of sample adds only one more step to the fabrication of the nanodisk structures previously described. As mentioned before, INPS features a support layer to separate its active plasmonic sensing elements and the systems being probed. This is achieved by depositing a thin dielectric layer onto the plasmonic nanostructure arrays to form homogeneous "sensor chips".

To provide a highly uniform and thus good protective layer I used a 10 nm Si_3N_4 film grown by PE-CVD to coat the nanodisks (**Figure 5.12**a). This results in a conformal and uniform coating over the entire sample surface (typically 1 cm^2), as shown schematically in **Figure 5.12**b and in the SEM images shown in **Figure 5.12**c.

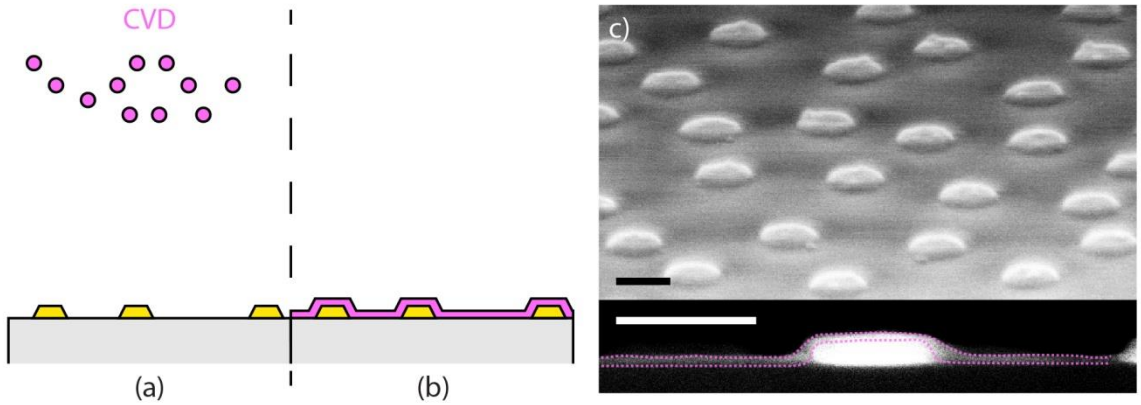

Figure 5.12. Fabrication of Indirect Nanoplasmonic Sensing (INPS) chips using HCL. *(a) The homogeneous support layer is an essential part of the INPS chip and is obtained by deposition of a thin dielectric layer onto the plasmonic structures. PE-CVD is usually the method chosen due to its high quality and conformal coating ability. (b) Schematic depiction of an INPS sensor where the plasmonic nanoparticles are covered by a dielectric layer. (c) 70^{o} (top) and 90^{o} (bottom) tilt-angle SEM images of an INPS chip consisting of an array of gold nanodisks with 190 nm diameter and 20 nm height, coated by a 10 nm Si_3N_4 protective layer. Note the conformity of the coating (pink dashed lines). The scale bars are 200 nm.*

6 Characterization Techniques

We never know how good something is until we see it and/or know what it is capable of. The same applies in science. Every material/sample should pass the process of characterization and this work is no exception. Naturally, in nanofabrication-related work, "appearance" is important. Thus, the Chapter begins with detailed information on how we can "see" nanoscale objects (even beyond what is on the surface) by two common electron microscopy methods, namely scanning electron microscopy and transmission electron microscopy. This is followed by characterization techniques that allow us to "touch" and reveal the state of nanoscale surface, that is, atomic force microscopy and x-ray photoelectron spectroscopy, respectively. Later on in the Chapter, I will introduce one of the main characterization techniques used in plasmonics-related studies, that is spectrophotometry. Basic spectrophomotery, as well as specific and detailed descriptions of the measurement setups used throughout the project are given. This includes a in-house-built vacuum chamber and a quartz tube flow reactor to assess the hydrogen sensing performance of the alloy nanoparticles in vacuum and in more realistic conditions, respectively. The Chapter concludes with a discussion of my attempt to combine gravimetric and optical characterization of hydrogen sorption in the nanoparticles.

6.1 Electron Microscopy

In the frame of nanoscale studies, the usage of *conventional* optical microscopy is limited. It is traditionally unable to image anything smaller than 100 nm (*i.e.* smaller than wavelength of light) as the diffraction limit comes into play, in which light is diffracted and thus cannot be focused to a point[362,363] (however, a new methodology called near-field optical microscopy is able to break the far-field diffraction limit and has successfully imaged a single molecule[364]).

To overcome this problem, one needs to use radiation with substantially shorter wavelength. Electrons are the perfect choice. The wave-particle duality exhibited by electrons enables their usage as "light" in microscopy. There are two basic types of electron microscopy: transmission electron microscopy (TEM) and scanning electron microscopy (SEM).

6.1.1 Scanning Electron Microsopy

A scanning electron microscope (SEM) is a type of electron microscope that images a sample by scanning it with a beam of electrons in a raster scan pattern. Upon the bombardment, the electron beam-solid interactions produce various kinds of excitations, as shown in **Figure 6.1**:

secondary electrons, backscattered electrons, Auger electrons, as well as X-rays. These different excitations, which can be detected by a state-of-the-art SEM's different types of detectors and analyzers, stem from different processes and thus carry *different* information about the sample, *e.g.* topography, composition and electrical conductivity. As imaging modes are concerned, only secondary electron and backscattered electron signals contain information about topography. The two, however, originate from different process and have different energies. Thus, they are captured using different detectors and carry slightly different information.

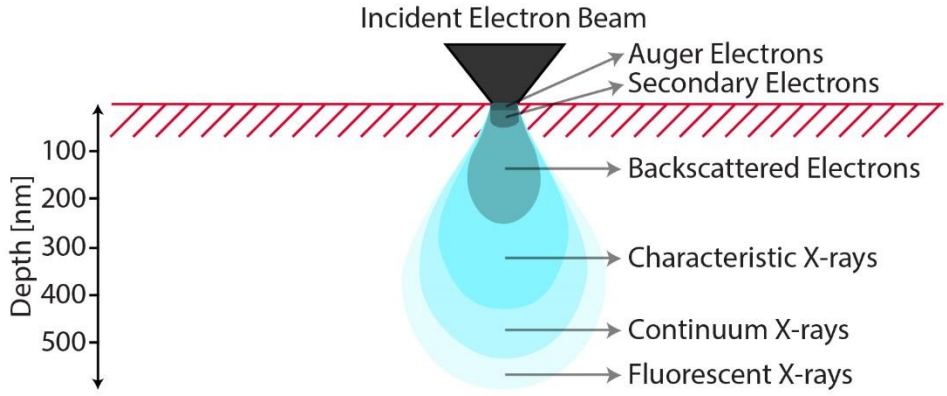

Figure 6.1. Electron beam-solid interactions. *The electron beam penetrates into a solid in a teardrop-shaped feature creating various kinds of excitations. The depth where the excitations originate from depends on their energy; the shallowest (less than 5 nm), Auger electrons, have the lowest energy and the deepest (up to more than half micron), fluorescent x-rays, have highest energy. However, note that the penetration depth also depends proportionally on the primary electron beam energy. Secondary and backscattered electrons are commonly used for imaging, whereas characteristic X-rays are used to analyze the composition of a specimen.*

Primary electrons, the electrons bombarding the sample, may lose some of their energy upon colliding and interacting with the sample. This process is known as inelastic scattering and occurs by interaction with electrons of the sample. From the principle of conservation of energy, the energy lost by the primary electrons will be compensated as a "gain" in energy of the electrons of the sample. If these are the outer-shell electrons, weakly bound to an atomic nucleus, most of the energy will be retained as kinetic energy, allowing the electrons to escape and travel through the solid as secondary electrons (SE). SE typically have kinetic energies of less than 100 eV and the average distance they can travel in the solid is limited to just one or two nm. This property provides excellent information about the surface structure as the secondary electrons that can be detected have to be created very close to the surface. Secondary electrons are thus able to produce the so-called topographical contrast of the samples studied.

Backscattered electrons (BSE), on the other hand, are elastically scattered primary electrons. Hence, BSE escape from the sample with energies only slightly smaller than the primary electron energy (*i.e.* higher energy than SE). Since elastic scattering is strongly dependent on the details of atoms the electrons collide with (*e.g.* atomic mass, crystal orientation, defects etc), BSE can provide information about microstructural parameters of materials. For typical use of

SEM, BSE offer good composition contrast if different chemical elements are present in a sample. Together, BSE and SE can be used interchangeably in an SEM to obtain topographical information complemented with some compositional information.

As mentioned before, the interaction of primary electrons and the sample also creates the emission of X-rays resulting from electronic shell transitions in the sample (**Figure 6.1**). The emitted X-rays, which may originate from several microns deep within the sample, carry energy characteristics of the element emitted from (*i.e.* every element has its own set of characteristic peaks in its X-ray emission spectrum). Thus, detection and measurement of these energies permits quantitative elemental analysis known as energy dispersive X-ray spectroscopy (EDS).

SEM has been an instrumental tool for the work presented in this thesis. All samples used for SEM studies were fabricated on silicon substrate (rather than glass as used for all optical characterization) to minimize the effect of charging during imaging, which is heavily occurring on dielectric substrates. While the charging effect by itself is not damaging the sample, it nonetheless creates distorted and poor resolution images due to the built-up of electrons on the surface, creating an electric field, which in turn deflects the incoming electron beam in undesirable ways.

6.1.2 Transmission Kikuchi Diffraction

Rich information provided by BSE outlined above spurred a class of techniques called electron backscatter diffraction (EBSD).[365] Specifically, EBSD is employed to characterize microstructural-crystallographic parameters in *bulk* materials such as crystal orientation, grain morphology and defects. That it is a bulk material is crucial for EBSD to provide a high enough number of scattered electrons to be detected. In EBDS, a tilted sample is irradiated with a beam of electrons which interact with the atoms in the crystal lattice. Some of the BSE leave at the Bragg condition from the sample crystal planes and form the so-called Kikuchi patterns.[366] These patterns relate to each of the diffracting planes in the lattice and thus a crystal orientation map can be constructed. This map provides essential information of the crystalline state of the sample, such as grain orientation and grain boundaries.

To do such measurements in *nanoparticles*, however, can be really difficult since the number of BSEs significantly decreases with volume. Additionally, nanoparticles feature a topographical profile which may introduce shadowing effects or deflect the BSE away from the detector. Only recently, a new method called Transmission Kikuchi Diffraction (TKD), or also commonly referred to as transmission EBSD, was developed to address this problem.[367] As the name suggests, instead, transmitted electrons are used to form the Kikuchi patterns and thus the studied nanoparticles have to be fabricated on a thin, electron transparent substrate (**Figure 6.2**). In this configuration, the detector is placed below the sample and thus is in line with the beam source. Doing so, the electron intensity greatly increases and hence the beam current can be reduced, which leads to further improvement in spatial resolution. To this end, spatial resolution of 5 nm or even less can be achieved. Furthermore, TKD features full automatization that allows analysis over large areas at very high speed so that quantification of nanoparticle

ensembles to derive the statistics of their crystallinity parameters can be accomplished conveniently.

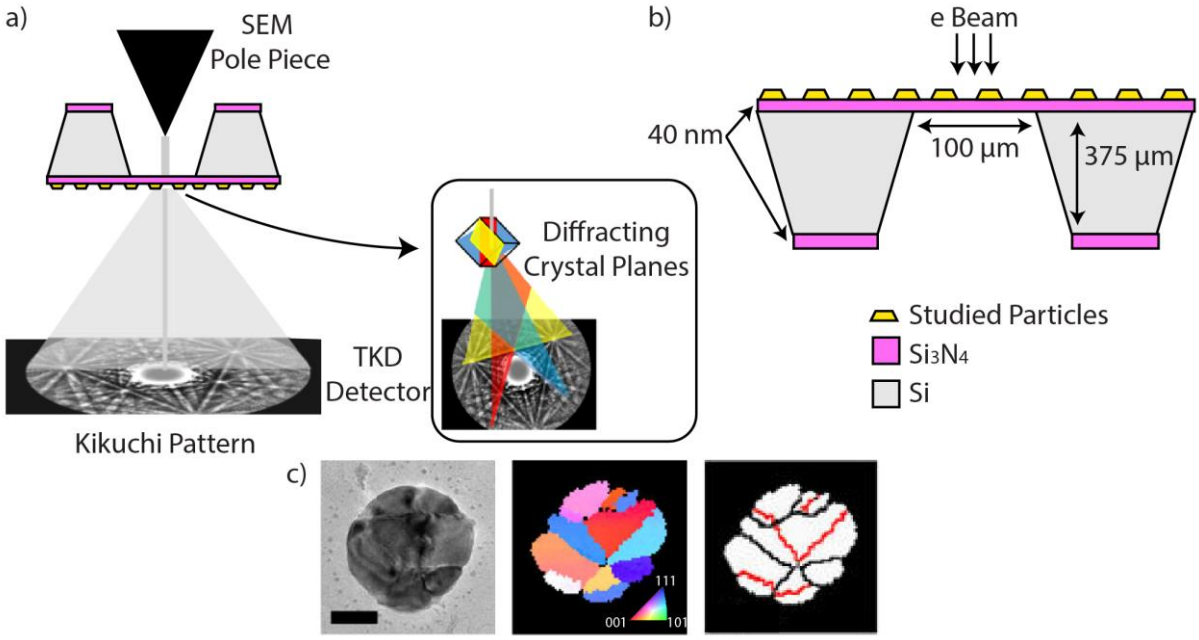

Figure 6.2. TKD schematics and analysis. *(a) Schematic of a TKD setup where the studied nanoparticles are placed facing away from the SEM pole piece. A detector is located below it and is able to capture the pattern that is unique for each crystallographic plane of the crystal in the nanoparticles. (b) Schematic of an electron-transparent window used in this thesis. The in-house made windows consist of a 40 nm Si_3N_4 thin film with 100 µm x 100 µm electron-transparent area. Note that the dimensions are not to scale. (c) Example of information provided by TKD. Left: an electron microscopy image of a single polycrystalline Pd nanodisk. Scale bar is 50 nm. Middle: TKD map showing grains differently colored according to their crystallographic orientation. Right: The grain boundaries separating each grain shown in the middle figure. Two types of grain boundaries can be distinguished: high-angle grain boundaries (HAGB, black) and twin boundaries (red). Figure (a) and (c) are adapted with permission from ref. 368. Copyright 2017 Macmillan Publishers Ltd.*

In this thesis, TKD is employed to reveal the microstructural details of the (polycrystalline) alloy nanoparticles studied in **Paper V**. Specifically, determination of the grain size, orientation and grain boundary length was conducted (see **Figure 6.2**c for example of such analysis). To allow such characterization on the nanoparticles, I fabricated them on thin Si_3N_4 windows made in-house following the procedure by Grant et al.[368]. The window consists of a 40 nm Si_3N_4 thin film with 100 µm x 100 µm electron-transparent area (**Figure 6.2**b). All TKD measurements and analysis included in this thesis were carried out by our collaborators at the Center for Electron Nanoscopy at the Technical University of Denmark.

6.1.3 Transmission Electron Microscopy

In contrast to the SEM, the transmission electron microscope (TEM) shoots electrons through a very thin sample and is thus conceptually similar to a conventional optical microscope

(although electrons are used instead of photons). Interactions of the electrons and the sample are reflected in the detected transmitted electrons, as well as in other emitted radiation such as X-rays. Similar to SEM, different types of information can be obtained depending on the sampled energy range and the type of analyzed radiation/electrons created upon interaction of the primary electrons with the specimen. In SEM, however, the resolution is mainly limited by the spot size of the scanning beam while in TEM it is not. Hence, a far better resolution can be achieved in TEM (even to a single atomic column). This can provide powerful analysis (*e.g.* elemental mapping via the EDS method described above) of a single nanoparticle. Similar to TKD described above, TEM requires samples to be prepared in a special way since they have to be thin enough to allow electrons to be transmitted (~50 nm or ideally less). Thus, a similar sample condition as the one used in TKD is required.

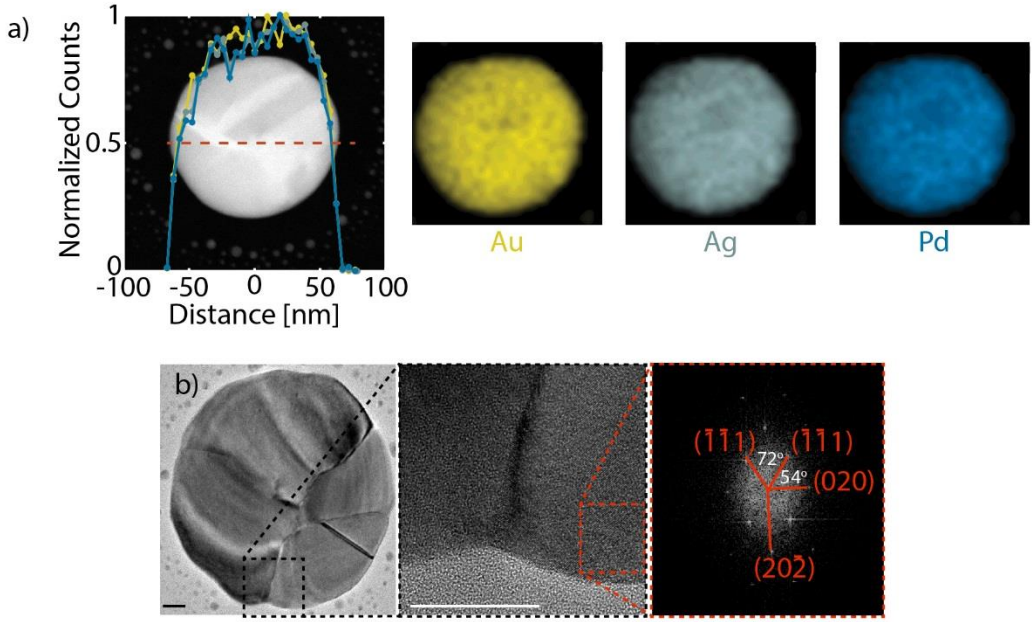

Figure 6.3. TEM characterization of nanofabricated alloy nanoparticles. *(a) The elemental distribution in a single ternary 33:34:33 AuAgPd alloy nanodisk is unveiled by an elemental linescan across a nanoparticle (left) and the corresponding elemental maps depicting the spatial distribution of elements in the nanoparticle (right), using scanning TEM (STEM) EDS analysis. STEM analysis allows elemental scanning/mapping with 5 nm resolution and reveals homogeneous alloy distribution throughout the nanoparticle. (b) High resolution bright field TEM image that reveals impressive details on a single binary 70:30 AuPd alloy nanoparticle. For example, the polycrystallinity of the particle is clearly seen. Using electron diffraction and fast Fourier transformation (FFT), the crystallinity of different grains in the nanoparticle can be analyzed and lattice parameters/atomic spacing can be extracted (right). The figures are adapted with permission from ref. 106. Copyright 2016 American Chemical Society.*

For the purpose of the work presented in this thesis, TEM was used to characterize the elemental distribution and crystallinity of the alloy nanoparticles fabricated and applied in **Paper I**, **III, IV, V** and **VII**. **Figure 6.3** shows a collage of different types of TEM-based analysis used for

characterization of the samples. The TEM analysis was carried out by our collaborators at the Center for Electron Nanoscopy at the Technical University of Denmark.

6.2 Surface Characterization

The three methods described above excellently provide images (and beyond that) of the studied nanoparticles. However, for certain purposes, these are not enough. Often I am interested to see the three-dimensional image of my samples and extract its corresponding height profile. In the case of alloys, it is also interesting to investigate "only" their surface and see how they are composed in atomic concentration with respect to the bulk. This is motivated by the fact that, due to the different energetics of a surface and bulk sites, different equilibrium concentrations of elements may appear at the surface and in the bulk, respectively, as discussed in **Chapter 3**.

6.2.1 Atomic Force Microscopy

Apart from the microscopy that utilizes beams of light or electrons, there is also a known family of microscopy called scanning probe microscopy (SPM). SPM uses interaction forces between a very sharp physical probe (thus it can be easily imagined as a "finger") and a surface. An image of the surface can be obtained by mechanically moving the probe in a raster scan pattern to "feel" the surface throughout the area of interest. The absence of a beam-dependent concept thus eliminates the diffraction limit problem.

Atomic force microscopy (AFM) is one of the SPM-family members. It operates by scanning a sharp probe connected to a microscale cantilever, which bends specifically depending on the interaction between the tip and the surface. The bending can be quantified by reflecting a laser beam from the back of the cantilever onto a photodiode which detects the offset of the signal from the center reference. A computer then evaluates the signal and sends back the response to the attached piezoelectric device controlling the cantilever. A simple schematic of AFM is shown in **Figure 6.4**a.

Based on the interactions, AFM is classified into two different imaging modes: contact and non-contact. The former yields very good resolution, however, with high risk, if not always, of sample surface modifications (especially for soft samples *e.g.* polymers) due to constant physical contact. The latter mode excludes such problems but at the cost of poorer resolution. A combination of the two modes exists: intermittent contact mode (also known as tapping mode). Instead of constantly touching the samples, tapping mode, as the name suggests, moves the tip back and forth. This is very advantageous for soft samples as the forces acting on them are very small. Thus no damage is induced. A simple depiction of the tapping mode is shown in **Figure 6.4**b.

In this thesis, tapping-mode AFM is used to examine the conformality of PTFE polymer deposited on the sensors in **Paper V**. The task is impossible to be done in SEM since a high energy electron beam will readily burn the polymer. Furthermore, in general, AFM provides extraordinary topographic contrast and unobscured views of surface features as compared to SEM. It also generates 3D images, which allow linescan analysis. This makes quantification of the profile height at an arbitrary position possible.

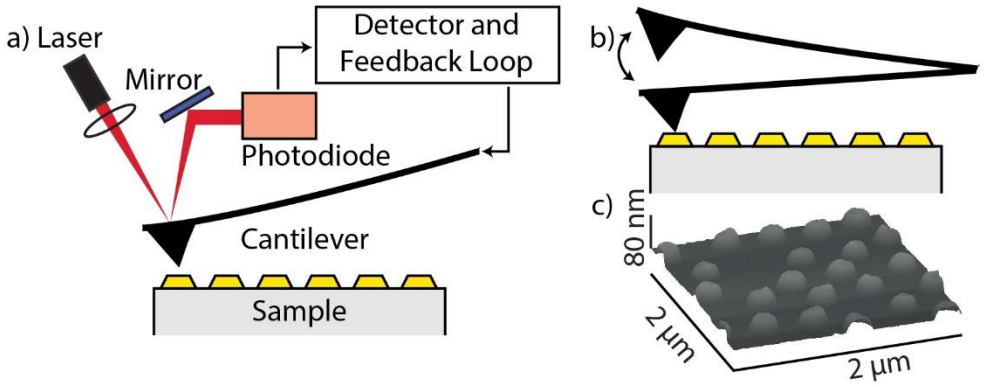

Figure 6.4. AFM schematics and analysis. *(a) AFM uses a cantilever with a very sharp tip that is scanned across the surface while a photodiode detector acquires the change in position of a reflected laser beam from the top of the cantilever. The signal is then processed in a computer and sent back to the cantilever to change and monitor the probe-surface distance. (b) Tapping mode is done by oscillating the tip while scanning the surface. Interaction with surface changes the oscillation frequency as well as the deflection which then is measured. (c) Typical 3D AFM image of a nanoparticle array made by Hole-Mask Colloidal Lithography.*

6.2.2 X-ray Photoelectron Spectroscopy

X-ray photoelectron spectroscopy (XPS) relies on the photoelectric effect to reveal the surface chemistry of a sample. The photoelectric effect occurs when electrons are emitted by a material that is irradiated by photons, and it was actually the theory that won Albert Einstein his Nobel Prize (not the famous relativity theory!). In a typical experiment, X-rays with specific energy (*e.g.* Mg Kα with energy of 1253.6 eV) are used to irradiate the sample. As the photons interact with the material, energy is transferred from the photons to the electrons in the material. If the energy is sufficient to overcome the binding energy, electrons will be emitted from the material. These electrons are called photoelectrons (**Figure 6.5**a), whose kinetic energies can be described by:

$$E_{kin} = hv - E_{bind} - \emptyset_s \qquad (6.1)$$

Where hv is the energy of the photon, E_{bind} is the binding energy of the photoelectrons and $\emptyset_s$ is the spectrometer work function which is defined by the spectrometer used.

As the mean free path of photoelectrons is very short, only a small portion of them, *i.e.* the ones originating from the top-most layer of the material being analyzed, can exit the material and reach the detector without further energy loss. Thus, XPS is a very surface sensitive technique. XPS spectra can then be constructed by plotting the energy and number of electrons emitted from the material (**Figure 6.5**b). Since each element possesses its own unique set of binding energies, XPS spectra can be used to identify elements present on the surface of a material. Furthermore, the chemical state of the elements (*e.g.* oxidized state) can also be determined since depending on whether an element is bound to another species or not, it will possess slightly different binding energies of its electrons. This difference in energies is due to electon transfer between the different species, which depends on their relative electron affinities.

Finally, a relative elemental quantification can also be obtained by integrating the area of different peaks in the spectrum.

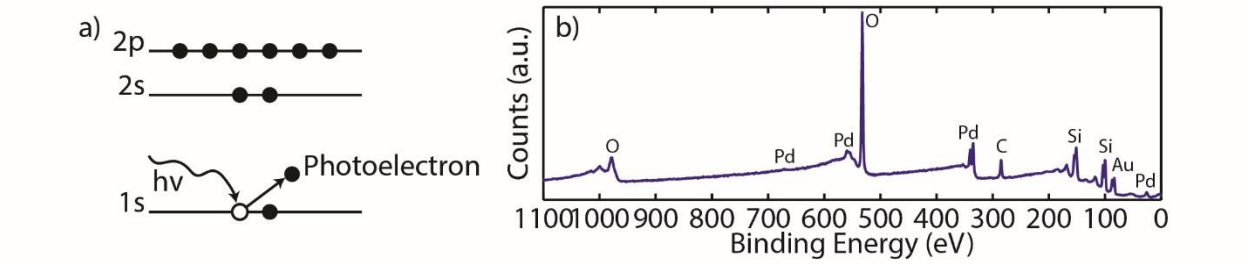

Figure 6.5. XPS photoelectron mechanism and a typical XPS spectrum. *(a) Principle of the photoemission of an electron. The schematic is adapted from ref. 369. (b) XPS spectra of a sample consisting of arrays of PdAu alloy nanoparticles. Different elemental components give rise to distinct peaks at various binding energies.*

The unique surface elemental information provided by XPS is valuable especially for the alloy systems, the main materials studied in this thesis, since alloy components tend to segregate to the surface over time[195] (see **Chapter 3**). Hence, XPS is the main analysis technique I have used to assess the surface stability of the PdAu (**Paper VII**) and PdAuCu (**Paper IV**) alloys. The XPS analysis presented in this thesis was carried by my colleagues Iwan Darmadi and Arturo Susarrey-Arce.

6.3 Optical Measurements of Hydrogen Sorption in Metal Nanoparticles

Since the sensors developed in this thesis rely on plasmonic effects, it is clear that the main characterization technique should be one that is able to provide information about the optical properties of the samples. Throughout my project, I relied mainly on spectrophotometry for this purpose. The basics of spectrophotometry and the instrument used to investigate the optical properties of my plasmonic samples at room temperature in air is explained first and followed by a discussion of the instruments that allow spectrophotometry in special conditions, *e.g.*, at elevated temperature and controlled exposure of the sample to gases.

6.3.1 Spectrophotometry

Spectrophotometry is a quantitative measurement of the optical properties of materials as a function of wavelength in the spectral region spanning from the ultraviolet (UV) to the visible (vis) and near-infrared (NIR) regions of the electromagnetic spectrum. In spectrophotometry the samples are irradiated by a beam of light, which is either made monochromatic and scanned using a motorized grating or polychromatic upon irradiation and then analyzed using a fixed grating. The optical properties of the sample can be analyzed as a function of wavelength using both approaches.

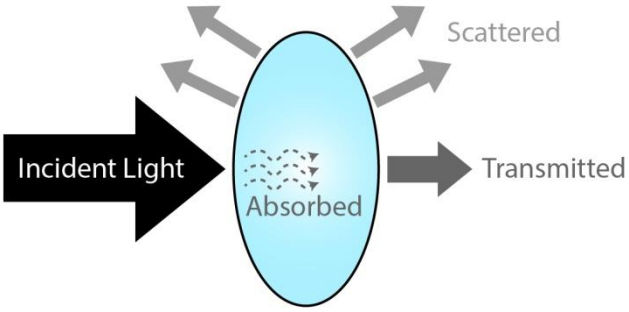

Figure 6.6. Interaction of a material with an incoming plane wave. *When light is irradiated on a material it is transmitted, scattered, or absorbed. Transmitted light is defined as photons exiting the material in forward direction, whereas scattered light is elastically or inelastically deflected in other spatial directions. Absorbed light, however, "vanishes" as it is converted to other forms of energy in the material such as electronic excitations and, ultimately, heat.*

When light is irradiated on an object it can be absorbed, scattered, or transmitted; as depicted in **Figure 6.6**. Transmittance (*T*) is defined as the transmitted intensity in forward direction (*I*) compared to the incident light intensity (I_o)

$$T = \frac{I}{I_o} \tag{6.2}$$

Absorbance (*Abs*) is related to transmittance as

$$Abs = log\frac{1}{T} = log\frac{I_o}{I} \tag{6.3}$$

Scattering (*S*), on the other hand, is the part of the light emerging in different directions from the incident light and, together with absorption (*A*), related to the extinction (*E*), as described by the optical theorem, as

$$E = A + S \tag{6.4}$$

while

$$E = 1 - T \tag{6.5}$$

Hence, from equation 6.4

$$A + S + T = 1 \tag{6.6}$$

which makes up the total incident light intensity (**Figure 6.6**).

The wavelength-dependent extinction *E* of a sample can thus be determined by measuring the transmittance *T* and by comparing the difference between light that passes through the sample and a suitable reference (*e.g.* the bare substrate in my case).

In this thesis, a Varian Cary 5000 double-beam spectrophotometer has been used to measure the extinction *E* of all my samples under ambient conditions, *i.e.* no external heating or gas flow. It was mainly used for evaluating optical properties such as the effect of composition on the bulk and surface to the optical properties of plasmonic alloy nanodisk arrays in **Paper I** and **VII**, respectively.

6.3.2 Optical Measurements in a Temperature-Controlled Vacuum Chamber

For the purpose of thoroughly characterizing our alloy hydrogen sensors in idealised conditions (*i.e.* in vacuum/pure H_2 environment) presented in **Paper I**, **III**, **IV**, **V** and **VII**, a custom-built chamber was used (**Figure 6.7**). The setup is vacuum compatible and allows heating up to 200°C. The chamber, which consists of stainless steel, is also equipped with two sapphire glass windows to enable optical access to the sample. A fiber coupled from the window to a fixed-grating CMOS spectrophotometer measures the transmission through the sample, which is illuminated via a second fiber attached to the other side of the chamber.

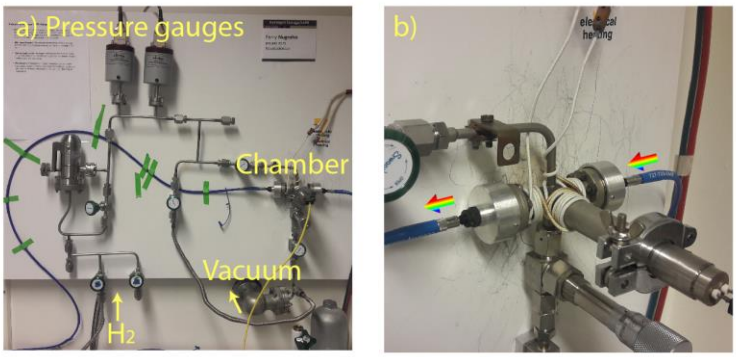

Figure 6.7. Vacuum chamber used for hydrogen sensing measurements. *(a) Overview of the setup consisting of a measurement chamber where the plasmonic sensor is placed and various pressure gauges and a vacuum pump to control the hydrogen pressure in the chamber. (b) Close-up of the chamber. There are two fibers attached. One is coupled to a light source while the other is coupled to a spectrophotometer.*

The setup is able to control the hydrogen pressure from a few microbar up to 1 bar, both quickly and (very) slowly. The former is important when assessing the kinetics of the studied system under hydrogen absorption/desorption. The latter allows careful study of the system under equilibrium conditions (*i.e.* sorption isotherms) at varying hydrogen pressure and is enabled by a UHV-compatible leak valve. The pressure inside the chamber is measured using a capacitance pressure gauge. The temperature is monitored using a thermocouple in direct contact with the sample, and it is controlled via a feedback mechanism by a Eurotherm controller and an external power supply used to control the heating via a resistive heating coil around the chamber. A Matlab program continuously records the sample temperature, the hydrogen pressure inside the chamber and the optical transmission through the sample.

6.3.3 Optical Measurements at Elevated Temperature under Gas Flow

To study the hydrogen sensing performance of the sensors developed in this thesis in more realistic conditions, a setup where multiple gases with different partial pressures can be controlled is required. To perform this task, a commercial Insplorion X1 mass flow reactor system (Insplorion AB, Göteborg, Sweden) was utilized. The general layout of the system is sketched in **Figure 6.8**. The reactor comprises a quartz tube equipped with a resistive heating coil. There are two thermocouples inside the tube; one to measure the upstream gas temperature and another one, touching the sample, to measure the actual temperature of the sample. The gas temperature reading is used in a feedback loop to control the temperature in the reactor. Temperatures up to 600°C can be achieved. The sample is located in the middle of the tube, mounted on a stainless steel rod sample holder. To measure the optical properties of the samples, a fiber-coupled halogen lamp is used. A fixed-grating CMOS spectrometer then collects the transmitted light and yields the wavelength-resolved extinction spectrum. Technically, the spectrometer is able to process the spectra as fast as every 1 ms. However, averaging is often employed to reduce noise. The gas composition and flow in the reactor are controlled by mass flow controllers, which are able to accurately supply sequences of different reactant flows and concentrations to the reactor tube and thus the sample. The setup maintains a total pressure of 1 atm. It is also important to note that since the gases are supplied into a rather large volume, apparent kinetics are convoluted by the time it takes for the gases to reach the sensors, as well as by "smeared-out" interfaces between gas pulses of different composition. To this end, a variety of gases are available such as H_2, O_2, Ar, synthetic air, CO, NO_2, CO_2, and CH_4.

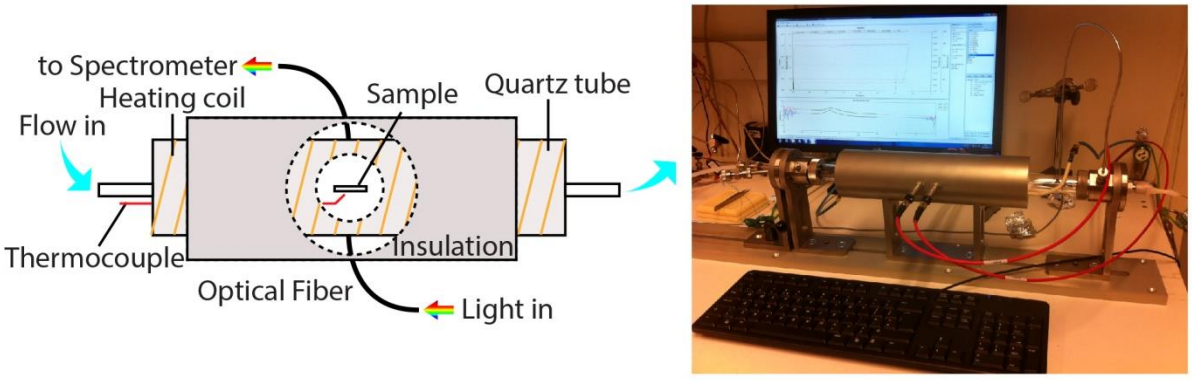

Figure 6.8. Insplorion X1 flow reactor with optical access. *Left: A sketch of the reactor and optical readout. The sample is placed inside the quartz tube equipped with a resistive heating coil. Light is irradiated onto the sample via fiber optics and detected by a fiber-coupled fixed-grating CMOS spectrometer. The mass flow controllers allow accurate control of gas flow and composition. Right: Photo of the reactor. The sketch of the reactor is reproduced with permission from ref. 159. Copyright 2017 American Chemical Society.*

6.3.4 Data Analysis

Once the spectra are acquired, the characteristic plasmonic readout parameters λ_{peak}, *Ext @ Peak*, and *FWHM* are extracted using a MATLAB code, which fits a Lorenztian function to the spectra. λ_{peak} can be determined by finding the wavelength where the first derivative of the fit is zero. In the case where experiments are done in the Inplorion X1 reactor system, the spectra are fitted to a 20th order polynomial function. With careful setting of fitting range, both fitting methods result in very similar λ_{peak} values - however with the Lorenztian fit featuring better signal to noise ratio (SNR) due to its insensitivity to minute features of the spectra (*e.g.* noise). Nonetheless *Ext @ Peak* can be defined as the extinction value at the corresponding λ_{peak}. *FWHM* is determined by finding the point on the wavelength axis (on the long wavelength side of the peak, to avoid convolution with *i.e.* interband absorption contributions or higher plasmonic modes) corresponding to the value of *E = Ext @ Peak / 2*. From this point, the spectral distance to the λ_{max} is calculated and multiplied by two to obtain the *FWHM*.

6.4 Gravimetric Measurements of Hydrogen in Metal Nanoparticles

A natural question to appear when one studies absorbing materials is: "how much do they actually absorb?" The answer, obviously, will be more meaningful if expressed in terms that are common to describe this *e.g.* amount or mass. For the Pd system studied in this thesis, none of all characterization techniques described above is able to provide us with quantitative information about the amount of hydrogen being absorbed (although technically TEM can serve such purpose by examining in detail the atomic lattice spacing of Pd when exposed to hydrogen.[261,370] But this requires a special kind of TEM and includes other complications, so let us leave it at that). A technique that has been universally used to measure tiny changes in mass of a material is Quartz Crystal Microbalance (QCM). Here, I will describe this technique and discuss a few optimization steps that were undertaken to be able to capture the mass of hydrogen, the lightest element in the universe, as it is absorbed in an array of nanoparticles.

6.4.1 Quartz Crystal Microbalance

QCM measures a mass change (Δm) on its surface by observing the change in its resonance frequency (Δf). The quartz crystal is piezoelectrically excited by applying an AC pulse through the Au electrodes grown on each side. (**Figure 6.9**a).[371] The AC pulse drives an in-plane shear oscillation of the quartz crystal (**Figure 6.9**b). The mass change, Δm, can be calculated by the Sauerbrey equation:[372]

$$\Delta m = -C\Delta f \tag{6.7}$$

where C is the mass sensitivity constant of the quartz crystal and thus depends on its type (*e.g.* C = -17.7 ng cm^{-2} Hz^{-1} for 5 MHz AT-cut crystal and C = -4.4 ng cm^{-2} Hz^{-1} for 10 MHz AT-cut crystal).

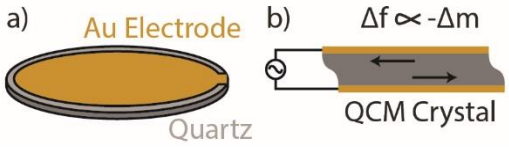

Figure 6.9. Quartz crystal for QCM experiments. *(a) Quartz crystal disk with Au electrodes on each side. (b) Shear oscillation at the piezoelectric quartz crystal's resonance frequency, induced by an AC pulse. The absolute change in the resonance frequency is proportional to the mass change on the crystal surface.*

QCM is a well-established technique and was first applied to measurements in UHV and in the gas phase (*i.e.* it is the way to determine the thickness of films deposited by PVD or CVD methods described in **Chapter 5**). However, the past couple of decades have seen QCM also as an invaluable experimental tool for studies in liquid phase *e.g.* biomolecular interactions at surfaces and biointerfaces.[373–376] Other than its high sensitivity, the popularity of QCM in the bio-related fields partly owes to its unique ability to reveal the viscoelastic properties of the adsorbed molecules (provided by the dissipation parameter of the crystal, which was developed here in our own Department[371]) and also its flexibility in terms of possibility to be combined with a vast variety of other analytical techniques *e.g.*, just to name a few, ellipsometry,[376,377] surface plasmon resonance[378,379] and reflectometry.[380,381]

Utilization of QCM for measurements of hydrogen storage properties in hydrides has started many decades ago. As early as the 1970-80s period, studies on Pd-H thin films using QCM were conducted, which gave us the well-known hydrogen concentration in fully hydrided Pd, that is 0.67 *H/Pd*.[382–389] Moving forward, as the interest to scrutinize *nanoparticulate* materials increased, QCM was also employed to study the hydrogen storage in Pd nanoparticles. It is my own supervisor, Christoph Langhammer, who first did QCM measurements on Pd nanodisks and nanorings[344] and later on clusters (radius < 5 nm).[147]

Measuring hydrogen absorbed in nanostructures is not at all a trivial task. As the volume of the material (significantly) decreases, so does the absolute amount of the absorbed hydrogen. This is further complicated by the inherent drift in QCM systems over time which can be on the order, if not higher, of the expected *Δf* induced by hydrogen absorption.[390] QCM crystals also typically suffer from sudden drift induced by thermal and mechanical stress. Hence, slight fluctuations in temperature, as well as stress caused by the lattice-expanding Pd during hydrogenation, give rise to *Δf*. Added with the fact that typical measurements take hours to complete, this results in a very low yield of successful experiments. To quote my own supervisor, *"One successful measurement often meant 5, 10, 20 unsuccessful ones. It is not exaggerated to say that.. ..calibration experiments with QCM took one month or even longer."*[391]

There are at least two strategies to alleviate the above problems. To minimize the risk of having unwanted *Δf* caused by thermal and mechanical stress, I used *SC-cut* quartz crystals. The "cut" reflects the cut angles with respect to the main crystallographic axes of the quartz. Without going into too much details, the particular SC-cut results in less shift due to mechanical stress. It also features superior temperature characteristics due to reduced sensitivity to temperature

change. Nonetheless, this one strategy alone is not enough to have a fully reliable measurement protocol that enables the measurement of full pressure-composition isotherms by exposing the sample to gradually changing hydrogen partial pressure (see left panels of **Figure 6.10**). The raw data obtained in this way still features unexpected drifts that occur randomly, creating at the end a somewhat indiscernible isotherm. In this thesis, instead, I developed a protocol that consists of "pulses" of hydrogen partial pressure. This way, a clear baseline is formed for each pressure step and thus it is self-referenced and in this way eliminates the drift problem (**Figure 6.10).** Employing this protocol, I have reached a 100% yield for isothem measurements in which details of Δf < 1 Hz can be resolved (see **Paper V**).

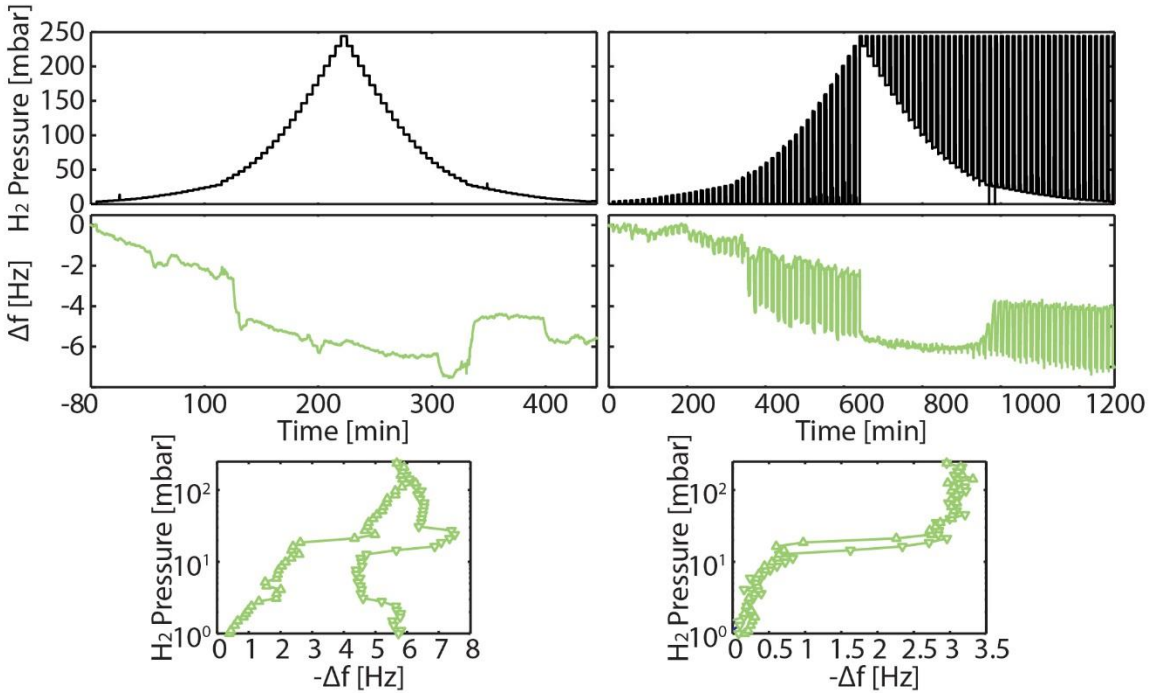

Figure 6.10. QCM response of two different gas pressure change protocols. *Top row: The panel on the left shows the common gradual hydrogen partial pressure change over time to measure an isotherm, while the right panel shows the pulsed gas change approach. For the rigth panel, the change in the hydrogen partial pressure always starts from a baseline (0% H_2 for absorption and 25% H_2 for desorption) and thus is self-referenced. Middle row: The raw QCM data of $Pd_{85}Au_{15}$ alloy nanoparticles obtained by the two different gas-exchange protocols. Bottom row: Hydrogen absorption and desorption isotherm plot as extracted from the raw data for the two protocols. For the conventional protocol, the drift dominates the result and renders the isotherm irreversible. For the pulse-protocol, a smooth and perfectly reversible isotherm is obtained.*

To obtain data that corresponds solely to the mass change due to hydrogen absorption in the nanoparticles, however, one more critical step has to be done. It has been shown for Pd thin films that numerous factors contribute to Δf: absorbed hydrogen, temperature variation, change in gas viscosity and crystal surface roughness. In my case, Δf due to temperature variation is considered to be negligible due to the fact that I used SC-cut crystals and the attained temperature in my experiments was very stable. Particularly for my case, surface roughness of

the crystal has also been shown to be negligible.[391] This leaves only the gas viscosity change for different hydrogen partial pressures. To account for this contribution, measurements on a blank crystal (*i.e.* without any nanoparticles) were conducted. As shown in **Figure 6.11**, indeed, *Δf* is observed as function of hydrogen partial pressure on a blank sensor due to a change in viscosity of the H_2/Ar gas mixture. With this at hand, the true response of the nanoparticles can be extracted by simple addition of the two data sets.

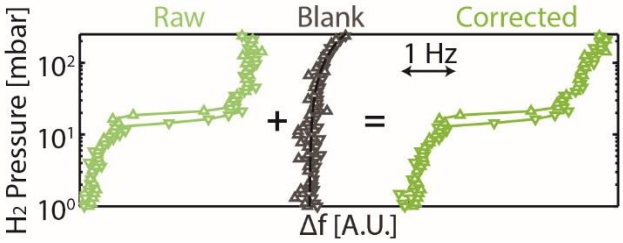

Figure 6.11. Correction of Δf due to gas viscosity. *To obtain the true QCM response for hydrogen absorption/desorption in the nanoparticles, the Δf contribution from the gas viscosity change during the isotherm measurement measured on a blank crystal (black) must be considered. Simple addition of the reference to the raw data (dark green) results in the corrected data (dark green).*

6.4.2 Combined QCM-Nanoplasmonic Sensing

Despite the wide interest in optical hydrogen sensors,[26] there are only very few attempts reported to directly correlate the optical properties of hydride forming materials and the hydrogen concentration inside them.[318,344,392] This is actually interesting and important not only from the fundamental point of view but also from the practical side as a means to further verify and quantify the signal change in the sensors to the hydrogen concentration. To this end, Beer-Lambert law has generally been assumed to hold for thin film hydride systems.[314] As my contribution to shed light on this issue, I have developed an experimental setup combining QCM and nanoplasmonic sensing using *exclusively* commercial components in **Paper II.** This contrast earlier attempts[393–395] of combining these two techniques in that no significant alterations to either the measurement chamber or the used crystal and its electrode configuration have to be made. Specifically, by utilizing the Au electrode of the quartz crystals as mirror, optical readout in reflection mode can realized in a straightforward way by using a fiber-optic reflectance probe. In order to do so, a dielectric spacer layer to separate the electrode and the studied nanoparticles has to be grown. Ideally, a thick spacer layer is used to avoid coupling between the plasmonically active nanoparticles and the Au electrode.[396] In my case, 100 nm dense SiO_2 is used as spacer layer. On it, straighforward fabrication of (alloy) nanoparticles can be carried out. When annealing is necessary, like for the case to achieve alloy formation, it is important to note that quartz crystals exhibit an α to β phase transition at 450°C, which is accompanied by cracking of the crystal.

The setup realized for the work carried out in this thesis is shown in **Figure 6.12**. I used a commercial QCM module equipped with a window (QSense E1). Above the window, a fiber-optic reflectance probe is positioned and connected to a light source and a spectrometer. The

in- and outlets of the module are then connected to a set of mass flow controllers regulating the hydrogen partial pressure in flow mode.

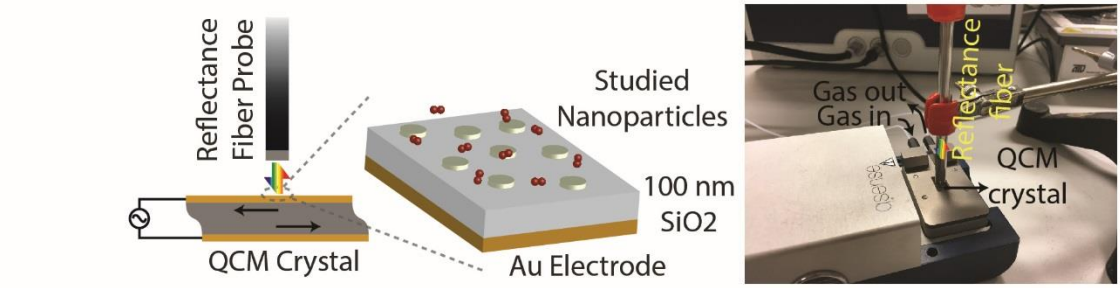

Figure 6.12. Combined QCM-nanoplasmonic sensing setup. *Left: Schematic of combined QCM and nanoplasmonic sensing used in this thesis. A fiber-optic reflectance probe is positioned above the QCM crystal and is connected to a white light source and a fixed-grating spectrometer. To minimize coupling of the LSPR modes in the investigated nanoparticles with the Au electrode of the QCM crystal, a 100-nm thick SiO_2 spacer layer is grown on the QCM electrode, onto which the nanoparticles subsequently are fabricated. Right: Realization of the setup.*

7 Summary and Outlook

At this point, I hope the reader has acquired the necessary (and hopefully interesting) knowledge to understand the work presented in the appended papers of this thesis. In this Chapter, I will give a brief summary for each of the papers, followed by a short outlook.

7.1 Summary of Appended Papers

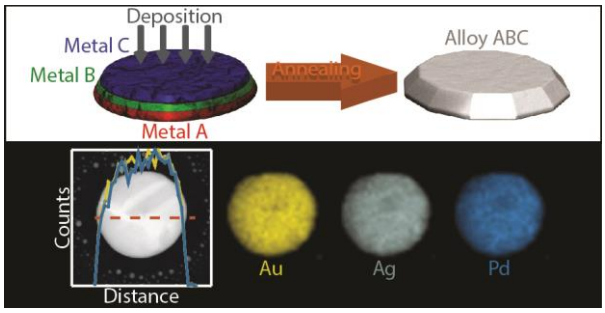

Paper I serves as the enabler for nearly all papers in this thesis. In this work, we established a bottom-up nanofabrication strategy to create arrays of metallic alloy nanoparticles on a support with excellent control on size and composition. This strategy is based on successive deposition of alloy element layers through a nanofabricated mask (HCL mask in our case) followed by annealing to induce the alloy formation. The method is generic as it allows an arbitrary number of alloy elements to be mixed (as long as they are miscible) and is compatible with different types of nanolithography methods. We demonstrated this approach by fabricating Au-based binary alloy nanoparticles of AuAg, AuCu and AuPd and a ternary alloy of AuAgPd. We characterized the formed alloys using different electron microscopy techniques and reveal excellent control of alloy composition, as well as homogeneous alloy formation throughout the fabricated nanoparticles. Flexibility in fabricating nanoparticles with different sizes and shapes was also demonstrated. We also characterized the optical properties of the alloys and scrutinized the dependence of the LSPR characteristics on alloy composition. Finally, we demonstrated the anticipated application of alloy nanoparticles for plasmonic hydrogen sensing. Here we used a binary PdAu alloy with 70:30 at.% composition that shows complete suppression of hysteresis during hydrogen sorption.

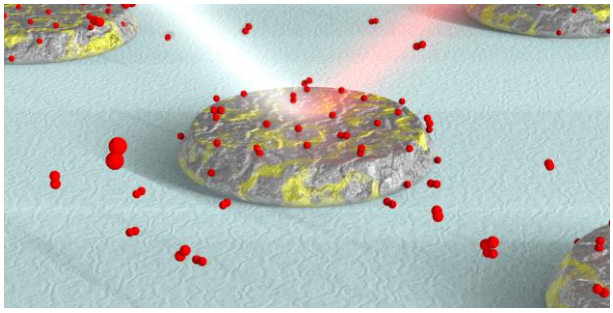

Paper II deals with an important question regarding optical hydrogen sensors: how does the optical properties correlate with the hydrogen concentration? Even in established sensors based on hydride-forming metal (alloy) thin films, this question was never explicitly addressed,[314] let alone for nanoplasmonic sensors. To shed light on the correlation between hydrogen concentration in the nanoparticles and their optical properties, in

this Paper we established an experimental setup comprising exclusively commercial components that allows simultaneous gravimetric and optical measurements. We systematically studied PdAu alloy nanoparticles (Au concentration 0–25 at.%, in 5 at.% steps) as model systems and found that the optical response, manifested in the LSPR, to hydrogen concentration in the nanoparticles is linear and, very interestingly, that the corresponding proportionality is universal for all of the investigated alloys. Examining PdAu nanoparticles with wide variety of dimensions also revealed that the sensitivity (*i.e.* the amplitude of optical response to hydrogen content) of a plasmonic hydrogen sensor is solely defined by the spectral LSPR position of the nanoparticles in the non-hydrogenated state, that is, that systems with LSPR at longer wavelength exhibit higher sensitivity. This opens a wide possibility to engineer the sensor sensitivity, as the LSPR of nanoplasmonic particles can be adjusted *via* tailoring of particle size, shape and arrangement. To rationalize the found universal scaling we also executed a theoretical analysis which implies that it is applicable not only for the PdAu system studied here but also to other Pd alloys as long as the alloyants are weakly interacting with hydrogen. All of the findings above constitute universal design rules for metal-hydride-based plasmonic hydrogen sensors.

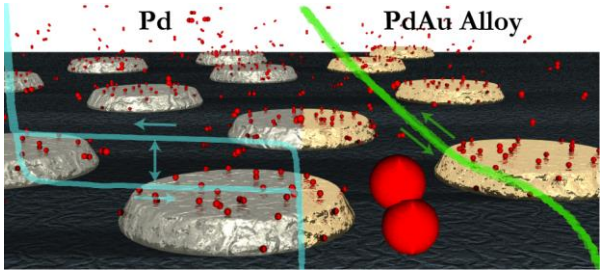

Paper III constitutes a first systematic assessment and demonstration of alloy nanoparticles as plasmonic hydrogen sensors. Specifically, we fabricated PdAu alloy sensor nanostructures with Au concentrations ranging from 0–25 at. % (5 at. % steps) and investigated their hydrogen sensing properties. Similar to results from alloy thin films of the same system, we find a continuous decrease of hysteresis upon increasing Au concentration until it completely disappears at 25 at.% Au. Consequently, this yields a plasmonic hydrogen sensor with readout uncertainty less than 5% throughout the investigated hydrogen pressure range of 1–1000 mbar. Moreover, we find an 8-fold sensitivity enhancement at low hydrogen pressure (*i.e.* 1–10 mbar) for sensors with 25 at.% Au compared to the one made of pure Pd, as well as reduced response time when exposed to 40 mbar hydrogen (*i.e.* the flammability limit). We also demonstrate a route to further improve the response time to below 1 second by tailoring the sensor nanoparticle size. All of the aforementioned results meet the performance targets for automotive hydrogen sensors previously presented in **Table 1.1**. Finally, we also find and report a distinct wavelength-independence of the qualitative sensor response to hydrogen pressure. This opens the possibility to use single-wavelength plasmonic hydrogen sensing, which promises the use of low-cost optical components such as cheap LED light sources and a simple photodiode detectors for implementation in real devices.

In **Paper IV**, we explored another type of Pd alloy using Cu as nanoplasmonic hydrogen sensor. This is motivated by the potential of efficient CO deactivation resistance provided by Cu as has been widely documented and

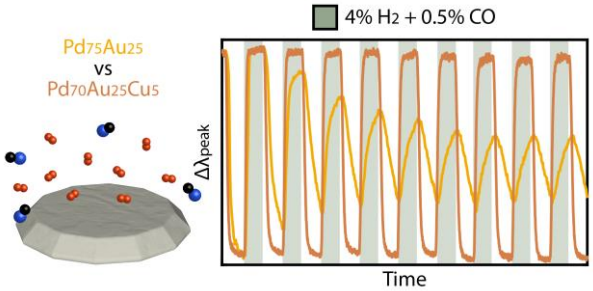

utilized in the field of hydrogen separation membranes.[190,192,194,336] Thus, capitalizing on such effects promises a sensing platform to be used in conditions where CO is abundant and/or present in trace amounts such as in ambient air. In the first part of the Paper we fabricated the alloy sensor nanostructures with Cu concentrations ranging from 0–30 at.% (5 at.% steps) and investigated their hydrogen sensing properties. Following the procedure established in **Paper II** we found that the optical response to hydrogen pressure is a linear function of the hydrogen concentration in the Pd host, with a scaling factor that is independent of the Cu concentration in the alloy, in excellent agreement with the hypothesis previously put forward. Similar to PdAu systems, hysteresis in the optical response to applied hydrogen partial pressure can be engineered and completely eliminated at a 30 at.% Cu content in the alloy. Furthermore, increasing the Cu content in the alloy also significantly decreases the sensor response and recovery times by a factor of 15 and 8, respectively, compared to neat Pd, which we pinned out due to a reduction of the apparent activation energy of the rate limiting steps. However, in contrast to the PdAu system, there is a decreased of the overall sensitivity of the PdCu alloy sensors for increasing Cu content in the alloy. Finally, we confirmed the anticipated resistance towards CO poisoning even with Cu content as low as 5 at.%. Building on this promising result, in the second part of the Paper, we rationally designed a plasmonic hydrogen sensor by combining the synergistic effects between the CO-poisoning resistant PdCu alloy system and the highly hydrogen sensitive PdAu alloy system. Choosing the champion system in **Paper III**, we fabricated a $Pd_{70}Au_{25}Cu_5$ ternary alloy plasmonic hydrogen sensor which exhibits excellent sensing metrics, that, is hysteresis-free response over 5 orders of magnitude hydrogen pressure with detection limit in the ppm range, sub-second response time at room temperature, CO, CO_2 and CH_4 poisoning resistance in synthetic air and excellent stability over time. All of these metrics meet or even exceed the corresponding strict hydrogen sensor performance targets presented in **Table 1.1**.

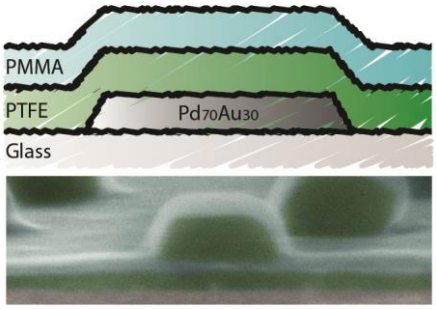

Another powerful strategy to prevent deactivation of palladium-based hydrogen sensing nanoparticles is by employing a molecular sieving layer.[313,337] Exploring this route, in **Paper V** we develop a nanoparticle-polymer hybrid plasmonic sensor where the alloy nanoparticles are coated by tailored thin polymeric films. Specifically, we employed $Pd_{70}Au_{30}$ alloy nanoparticles, together with a pure Pd control, as the hydrogen sensor and in the first part of the work encapsulated it in a 30 nm thick polytetrafluoroethylene (PTFE) coating. Characterizing the hydrogen sorption characteristics of the coated system, we noted two key effects facilitated by the PTFE film: (i) an enhanced optical response to hydrogen by up to a factor of two, and (ii) enhanced ab- and desorption kinetics. Specifically, we achieved (i) an extrapolated limit of detection of < 5 ppm H_2, establishing our sensor as one of the most sensitive hydrogen sensors reported to date, and (ii) sub-second response time to 1 mbar H_2 at room temperature, therefore being the first reported sensor to meet this strict requirement.[24] Through Arrhenius analysis we found that the enhancement of the kinetics is the consequence of a reduction in the apparent activation energy of the rate limiting steps for hydrogen absorption and desorption in the nanoparticles. Unfortunately, however, the PTFE-coated

sensors are readily deactivated when exposed to 0.5% CO and 0.05% NO_2 in synthetic air. To address this issue we then explored a second type of polymer, that is, poly(methyl methacrylate) – PMMA, for which excellent resistance against CO and NO_2 had been reported[337] and also manifested itself in our experiments. Interestingly, enhanced sensitivity and kinetics, as obtained from the PTFE coating, were also enabled by PMMA. However, the kinetics enhancement we found for the PMMA system was smaller than the one for PTFE, due to, as we show, a smaller reduction of apparent sorption activation energies for hydrogen absorption and desorption. Finally, to capitalize on the complementing benefits of the two polymers, *i.e.* maximal kinetics enhancement by PTFE and excellent molecular sieving by PMMA, we realized a heterostructure sensing platform comprising a tandem PTFE@PMMA layer on top of the $Pd_{70}Au_{30}$ alloy plasmonic nanoparticle sensor. This heterostructure design provides impressive protection against deactivating gases CO_2, CO and NO_2, while the unprecedented sub-second response time to hydrogen pressure in the range of 1–100 mbar provided by PTFE is retained. In this way, the platform developed in this Paper enables a new mechanism by which next generation hydrogen sensors featuring high sensitivity, fast response and excellent stability in poisoning environments can be realized.

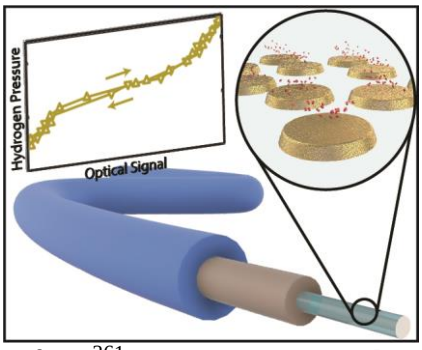

With all the promises shown by the nanoplasmonic hydrogen sensors in **Paper III**-**V**, it will be highly desirable if they can be adapted into a platform that is more scalable and closer to real application. In this regard, a fiber optic platform is very attractive due to its small footprint and mass-production potential and also, more importantly, due to its effective remote readout that reduces the risk of spark generation at flammable hydrogen concentrations. Modifying a recent method of transferring nanofabricated structures onto another surface,[361] in **Paper VI** we realize a fiber optic nanoplasmonic alloy hydrogen sensor. In a more general perspective, this Paper also constitutes the first successful attempt in transferring nanofabricated structures on an optical fiber. In detail, we utilized thin Cr and C films as sacrificial and transfer layer, respectively, on which PdAu nanoparticle arrays were fabricated. These nanoparticles were then transferred onto an unclad end of a commercial fiber. Depositing a thin Al mirror at the tip of the fiber allows wavelength-resolved optical readout in a reflection mode whose intensity depends proportionally to the hydrogen concentration in the environment. This method also permits the usage of monochromatic readout using cheap components like LEDs and photodiodes. To demonstrate the functionality of the transferred arrays of PdAu nanoparticles, we characterized its absorption and desorption isotherms and kinetics. As anticipated, the fiber alloy sensor retains the hysteresis-free response with kinetics faster than the one of pure Pd.

One of the inevitable consequences when using alloy materials is the fact that segregation of alloy elements is inherent in them. As such, this dynamic change of an alloy surface composition may influence its functionality, especially when facilitated by the surface itself or when the generated mismatch between the segregated surface layer and the layers beneath it influences a process occurring inside the system, like in the case here for the hydride formation in nanoparticles. Knowing this importance, and due to lacking related experimental studies, in

Paper VII we investigated *in operando* the surface segregation state dynamics of $Pd_{75}Au_{25}$ alloy nanoparticles using their intrinsic localized surface plasmon resonance (LSPR) as a probe. We found a direct correlation between LSPR peak shift, $\Delta\lambda_{peak}$, and Au composition on the surface, determined by XPS analysis from the same sample, over the course of 90 days. We also investigated the impact of the found Au segregation to the alloy surface on the hydrogen sorption thermodynamics and kinetics of the alloy nanoparticles. We found a gradual appearance of hysteresis in the isotherms for an aged sample, accompanied by slower kinetics during hydrogen desorption.

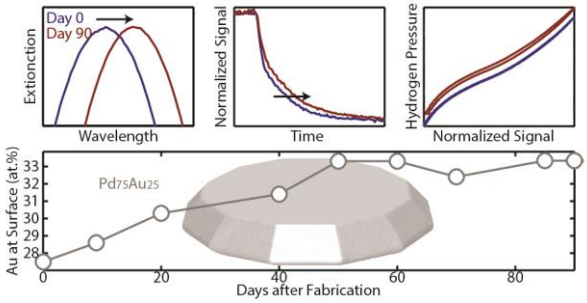

In **Paper VIII** we use indirect nanoplasmonic sensing (INPS) to study the CO_2 adsorption energetics of a microporous polymer. Specifically, we used the well-studied PIM-1 microporous polymer, which has high CO_2 permeability and selectivity, to benchmark our method. By tracking the LSPR readout of the PIM-1 coated INPS sensor in different CO_2 partial pressures and temperatures, we are able to construct CO_2 adsorption isotherms for PIM-1, and fit them using a Langmuir adsorption model. From the isotherms we extracted a Q_{st} of around 29 kJ/mol, which is in excellent agreement with other reports measuring Q_{st} using conventional gravimetric analysis. One of the advantages of our method compared to traditional ones is that sample calibration (*i.e.* the determination of sample's mass and/or volume) is not necessary. We demonstrate this by obtaining similar Q_{st} from four PIM-1 samples with different thicknesses (300–600 nm) without the need to determine their masses and/or volumes accurately and involve them in the data analysis. Moreover, we find that the CO_2 adsorption on PIM-1 can be directly observed and characterized without using INPS (*i.e.* just on glass substrate) and similar Q_{st} were obtained. This is made possible since PIM-1 exhibits an optical absorption band below 480 nm, which provides the necessary optical contrast to detect CO_2 adsorption in a simple transmittance measurement. This study provides a general blueprint for efficient optical screening of (polymeric) materials in terms of their gas adsorption characteristics and energetics.

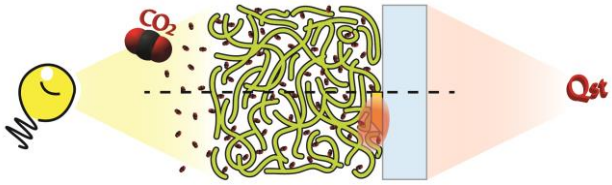

7.2 Outlook

There are many possibilities to continue the work presented in this thesis, especially since we successfully established a fabrication method to produce alloy nanoparticles with excellent control of their composition. This method is highly interesting for many different scientific fields beyond alloy hydrogen sensors presented in this thesis. Specifically, I believe that this may promote significant progress in the field of "alloy plasmonics" both from a fundamental and practical point of view. As an important ingredient towards wide utilization in plasmonics it will be interesting to establish, if possible, a generic model or to generate a library for the dielectric function of metal alloys with arbitrary elements. Even for the well-studied AuAg alloy system, such a model is still actively sought after and several different approaches have

been presented.[108,110,397,398] Finding such a generic model or establishing a dielectric function library will be very important for designing alloy nanoparticles with desired optical properties, which later can be exploited for different applications.

For the hydrogen sensors, I would really love to divert the efforts into addressing more of the fundamental aspects. Understanding the fundamental material properties and their correlation to the observed hydrogen sorption behaviours will provide powerful insights for better designing and engineering of the sensors to ultimately achieve an even faster, more sensitive and stable detection system. For example, what is the origin of the enhanced kinetics in the Pd alloys? As presented in **Paper IV** and **V**, and also from our preliminary results for the case of PdAu alloys, there is a systematic reduction in the apparent activation energy of the rate limiting steps with increasing alloyant concentrations. How does the corresponding sorption mechanism change? Clearly, these answers can be provided by working closely with theoreticians with the help of simulation techniques such as through density functional theory (DTF). Similarly, scrutinizing the exact correlation between grain properties and kinetics in the alloy nanoparticles is also interesting. As shown in **Paper V**, the average grain size (and thus grain boundary length) seems to affect the hydrogen sorption kinetics. Our preliminary results of Pd annealed at different duration (presumably bigger grain size for longer annealing) tend to agree with this observation as well, which indicates that polycrystalline nanoparticles with small grains exhibit faster kinetics. This implies that in the pursuit of fast hydrogen sensors, finding ways to generate alloy nanoparticles with controlled (and small) grain sizes is highly motivated. As a last example in this direction, determining the definite reason for the seemingly generic effect of faster kinetics by applying a coating layer onto a Pd surface will be really valuable. This finding will enable rational selection of the coating layer or even trigger efforts towards synthesizing new types of materials that combine the identified enabling properties and other functionalities, *e.g.* sieving.

Nonetheless, there are also a few experimental works that are interesting to pursue. For example, due to successful realization of ternary system in **Paper IV**, it will be useful if we can do systematic studies examining hydrogen sorption properties in the ternary with different composition. Which component, *i.e.* Au or Cu, dominates the properties? What composition is the best *e.g.* in terms of kinetics, sensitivity and resistance to CO? I am also curious to use Ag instead of Au since it is plasmonically a better material and therefore can be expected to feature higher sensitivity. The enhanced kinetics and stability provided by the plastic plasmonic sensor in **Paper V** may also initiate interest in developing composite hydrogen sensors. In this direction, a *truly* plastic plasmonic sensor can be developed by fully embedding the nanoparticles in a polymer matrix. This can be achieved by mixing the polymer and the alloy nanoparticles, which can be nanofabricated and transferred into a colloidal suspension[399] or generated via colloidal synthesis (note that currently there is no robust method to produce alloy nanoparticles with controlled composition and size, as discussed in **Chapter 3**). This method promises potential of scalable and large-scale processing and also the ability to generate not only flexible sensors that can be formed into various shapes or even casted into 3D objects. In the case of a sensor in film form, it can be coupled to a thin interference layer (*e.g.* Al_2O_3) to

generate optical contrast that can be readable by eye,[316] providing a sensing platform that is completely free of electrical components.

Clearly, there are many interesting and fun continuation that can be pursued based on the results presented in this thesis. I am really excited to see how far this will go in many years from now.

8 Acknowledgements

Finally! After weeks spent to write this thesis, I reach this Chapter; the most important part of the thesis (don't feel bad if you only read this Chapter, I do understand and I am already grateful). This thesis would have never been written without all the helps and supports from *a lot* of wonderful people. I certainly will never be able to mention all of these individuals in the following couple of pages but be assured that ***all*** helps are appreciated and remembered ☺.

My study has been financed by the Swedish Foundation for Strategic Research Framework Program RMA 11-0037 and the Mistra Environmental Nanosafety project. I also acknowledge Knut and Alice Wallenberg Foundation for their support of the infrastructure in the MC2 nanofabrication laboratory at Chalmers, and the Swedish Research Council for their support of the μ-fab cleanroom infrastructure in Sweden.

First and foremost I would like to thank God and His messengers. The journey that I have had is nothing but the signs of His blessings. I sincerely hope that I can be a good human being and all the work done in this thesis (and beyond it) is of utmost beneficial for a lot of people.

I would like to also thank Sweden and its people, for creating a culture and value where one can have a perfect balance between PhD and family. As one being trained in one of the most demanding countries in in the world, I never imagined such concept exists!

I would also like to express my gratitude towards these people:

Christoph, simply for everything ☺. Where do I start? I sincerely believe that I can write all the good things about you as thick as this thesis, and that's not an exaggeration. We met through an unusual path and yet you were the main reason I had to cancel my plan of leaving Sweden right after I got my Master Degree (too cold, too far). Here I am, seven years later, still in awe with what you have achieved. You are truly an inspiration, as a scientist and as human being, and I would like to learn all from you. Your enthusiasm and positivism are unparalleled. You are the best supervisor/mentor one can ever have. Thanks for always answering my (mostly unrelated to science) questions. Be prepared, there will be a lot more to come!

Henrik, my examiner, for providing a comfortable working atmosphere, for all the feedbacks, and, more importantly, for your prompt help when my wife first came to Sweden. We owe you a lot.

Lars, for all the helps in the lab and in the office. I am a proud user of Windows 7 now, thanks to you.

Past and current members of Chemical Physics group. Thank you all for giving a nice environment to work in and all the fun activities and fika. All the best for all of you!

All colleagues whose thesis project I supervised: Sune, Robin, Padraic (my man!), Viktor and Harald. All the best!

Past and current members of the LanghammerLab: Viktoria, Kristina, Carl, Pooya, Rickard, Joachim, Su, Arturo, Stephan, Colin, Irem, Barbora, Zafer, Sara, Christopher. Special shout to David for putting up with me in the office and my fellow countryman, Iwan. Sukses, Wan! Mari kita kuasai lab :D

Nanofabrication laboratory staffs, especially Henrik and Mats, who always help.

All other components in Chalmers. Joy and Eddy for taking care of my (lot of) posts. Ola for prompt help with computers. Milan, Lasse and Lennart for the gases. Everyone in administration, cleaning the office, delivering mails, etc. Thank you very much!

I am very grateful to get a chance to collaborate with many different wonderful people: Tomasz and Vladimir, Amaia, Camilla, Liyang and Christian from Chemistry. Ben, Shima, Alice and Jakob from DTU, Chao and Niklas from Stockholm University, and lastly Herman, Lars and Bernard from Delft. Thank you!

All of the Indonesian friends and communities in Gothenburg that make it feel like home, terima kasih banyak. Throughout seven years in Sweden I have met many great and talented Indonesians. Let's build our home for the better in the future. Special support for fellow PhDs: Iwan, Maulana, Iqbaal, Alit. Semangat yeaw xixixi

My family in Indonesia, my siblings and my nieces, for all the loves, supports and prayers. I will visit and bring a lot of chocolates!

My parents, for everything. I don't have a lot of memories about us, but I truly believe that you nurtured me with love and showered me with noble values. Everything good that I do will always be parts of your legacy. I miss you and I always pray for you.

Lastly, the most important people in my life now. My daughters, Asiyah and Maryam. Two of my most significant "products" of my PhD. Thank you for constantly teaching me love and sincerity, and for all the smiles and laughs every time I reach home. I hope I excels my other PhD (ParenthooD) and you will see me as a good father. I put you two in the cover of this thesis so that when you grow up, you will know that you are my biggest motivation throughout this journey. And lastly, to my wife, Iie. I don't even know what to say. You are my life. I am forever grateful I met you and be your husband. Thank you for always being at my side. You sacrificed a lot for me in this journey. I love you. Let's go for a holiday. You truly deserve it ☺

9 Bibliography

(1) No Title http://www.spaarnestadphoto.nl/.
(2) Schlapbach, L. *Nature* **2009**, *460* (7257), 809–811.
(3) Demirdoven, N.; Deutch, J.; Golden, D. M. *Science (80-.).* **2004**, *305* (5686), 974–976.
(4) Bockris, J. O. M. *Energy, the solar hydrogen alternative*; Wiley: New York, 1975.
(5) Crabtree, G. W.; Dresselhaus, M. S.; Buchanan, M. V. *Phys. Today* **2004**, *57* (12), 39–44.
(6) *Hydrogen Fueling Infrastructure Development - U.S. Deparment of Energy*; 2017.
(7) Hydrogen Detectors Adopted in Toyota Fuel Cell Vehicle Mirai http://www.nissha.com/english/news/2014/12/12th_1.html (accessed Mar 9, 2018).
(8) Gupta, R. B. *Hydrogen fuel: production, transport and storage*; Taylor & Francis, 2009.
(9) Rana, S. V.; Malik, A. *Indian J. Clin. Biochem.* **2014**, *29* (4), 398–405.
(10) Grimes, C. A.; Ong, K. G.; Varghese, O. K.; Yang, X.; Mor, G.; Paulose, M.; Dickey, E. C.; Ruan, C.; Pishko, M. V.; Kendig, J. W.; Mason, A. J. *Sensors* **2003**, *3* (3), 69–82.
(11) Bakenne, A.; Nuttall, W.; Kazantzis, N. *Int. J. Hydrogen Energy* **2016**, *41* (19), 7744–7753.
(12) Zhao, D.; Wang, T.; Heineman, W. R. *TrAC - Trends Anal. Chem.* **2016**, *79*, 269–275.
(13) Flat Icon www.flaticon.com.
(14) HD Wallpapers Act http://www.hdwallpapersact.com/blue-sky/ (accessed Dec 10, 2015).
(15) Sinclair, I. *Sensors and Transducers*, Third Edit.; Science Direct, 2001.
(16) Adams, B. D.; Chen, A. *Mater. Today* **2011**, *14* (6), 282–289.
(17) El Matbouly, H.; Domingue, F.; Palmisano, V.; Boon-Brett, L.; Post, M. B.; Rivkin, C.; Burgess, R.; Buttner, W. J. *Int. J. Hydrogen Energy* **2014**, *39* (9), 4664–4673.
(18) Palmisano, V.; Boon-Brett, L.; Bonato, C.; Harskamp, F.; Buttner, W. J.; Post, M. B.; Burgess, R.; Rivkin, C. *Int. J. Hydrogen Energy* **2014**, *39* (35), 20491–20496.
(19) Palmisano, V.; Weidner, E.; Boon-Brett, L.; Bonato, C.; Harskamp, F.; Moretto, P.; Post, M. B.; Burgess, R.; Rivkin, C.; Buttner, W. J. *Int. J. Hydrogen Energy* **2015**, *40* (35), 11740–11747.
(20) Hübert, T.; Boon-Brett, L.; Black, G.; Banach, U. *Sensors Actuators, B Chem.* **2011**, *157* (2), 329–352.
(21) *ISO 26142:2010 Hydrogen detection apparatus -- Stationary applications*; 2010.
(22) StorHy – Hydrogen storage systems for automotive application: Integrated Project Number 502667. Final report on sensor testing, Deliverable DSA10 http://www.storhy.net/.
(23) Boon-Brett, L.; Bousek, J.; Black, G.; Moretto, P.; Castello, P.; Hübert, T.; Banach, U. *Int. J. Hydrogen Energy* **2010**, *35* (1), 373–384.
(24) *U.S. Department of Energy, Energy Efficiency and Renewable Energy (EERE), Fuel Cell Technologies Office. Multi-Year Research, Development, and Demonstration Plan, 2011-2020. Section 3.7 Hydrogen Safety, Codes and Standards*; 2015.
(25) Penner, R. M. *Acc. Chem. Res.* **2017**, *50* (8), 1902–1910.

(26) Wadell, C.; Syrenova, S.; Langhammer, C. *ACS Nano* **2014**, *8* (12), 11925–11940.
(27) Schwarz, R. B.; Khachaturyan, A. G. *Acta Mater.* **2006**, *54* (2), 313–323.
(28) Clerbaux, C.; Edwards, D. P.; Deeter, M.; Emmons, L.; Lamarque, J.-F.; Tie, X. X.; Massie, S. T.; Gille, J. *Geophys. Res. Lett.* **2008**, *35* (3), L03817.
(29) Hübert, T.; Boon-Brett, L.; Palmisano, V.; Bader, M. A. *Int. J. Hydrogen Energy* **2014**, *39* (35), 20474–20483.
(30) Korotcenkov, G.; Han, S. Do; Stetter, J. R. *Chem. Rev.* **2009**, *109* (3), 1402–1433.
(31) Mayer, K. M.; Hafner, J. H. *Chem. Rev.* **2011**, *111* (6), 3828–3857.
(32) Feynmann, R. P. Plenty of Room at the Bottom, 1959.
(33) Larsson, E. M.; Alegret, J.; Käll, M.; Sutherland, D. S. *Nano Lett.* **2007**, *7* (5), 1256–1263.
(34) McMahon, S. J.; Currell, F. J. In *Nanomedicine*; Elsevier, 2013; pp 65–66.
(35) Barber, D. J.; Freestone, I. C. *Archaeometry* **1990**, *32* (1), 33–45.
(36) The British Museum http://www.britishmuseum.org/ (accessed Dec 10, 2015).
(37) Mie, G. *Ann. Phys.* **1908**, *330* (3), 377–445.
(38) Stockman, M. *Phys. Rev. Lett.* **2004**, *93* (13), 137404.
(39) Verhagen, E.; Kuipers, L.; Polman, A. *Nano Lett.* **2007**, *7* (2), 334–337.
(40) Xiao, J. J.; Yakubo, K.; Yu, K. W. *Appl. Phys. Lett.* **2006**, *88* (24), 241111.
(41) Smolyaninov, I. I.; Davis, C. C. *Chemphyschem* **2009**, *10* (4), 625–628.
(42) Huang, X.; Jain, P. K.; El-Sayed, I. H.; El-Sayed, M. A. *Lasers Med. Sci.* **2008**, *23* (3), 217–228.
(43) Hainfeld, J. F.; Slatkin, D. N.; Smilowitz, H. M. *Phys. Med. Biol.* **2004**, *49* (18), N309–N315.
(44) Paciotti, G. F.; Kingston, D. G. I.; Tamarkin, L. *Drug Dev. Res.* **2006**, *67* (1), 47–54.
(45) Anker, J. N.; Hall, W. P.; Lyandres, O.; Shah, N. C.; Zhao, J.; Van Duyne, R. P. *Nat. Mater.* **2008**, *7* (6), 442–453.
(46) Novo, C.; Funston, A. M.; Mulvaney, P. *Nat. Nanotechnol.* **2008**, *3* (10), 598–602.
(47) Stewart, M. E.; Anderton, C. R.; Thompson, L. B.; Maria, J.; Gray, S. K.; Rogers, J. A.; Nuzzo, R. G. *Chem. Rev.* **2008**, *108* (2), 494–521.
(48) Larsson, E. M.; Syrenova, S.; Langhammer, C. *Nanophotonics* **2012**, *1* (3–4), 249–266.
(49) Tittl, A.; Giessen, H.; Liu, N. *Nanophotonics* **2014**, *3* (3), 157–180.
(50) Nugroho, F. A. A.; Xu, C.; Hedin, N.; Langhammer, C. *Anal. Chem.* **2015**, *87* (20), 10161–10165.
(51) Kreno, L. E.; Hupp, J. T.; Van Duyne, R. P. *Anal. Chem.* **2010**, *82* (19), 8042–8046.
(52) Langhammer, C.; Zorić, I.; Kasemo, B.; Clemens, B. M. *Nano Lett.* **2007**, *7* (10), 3122–3127.
(53) Yip, H. K.; Zhu, X.; Zhuo, X.; Jiang, R.; Yang, Z.; Wang, J. *Adv. Opt. Mater.* **2017**, *5* (24), 1700740.
(54) Jiang, R.; Qin, F.; Ruan, Q.; Wang, J.; Jin, C. *Adv. Funct. Mater.* **2014**, *24* (46).
(55) Liu, N.; Tang, M. L.; Hentschel, M.; Giessen, H.; Alivisatos, A. P. *Nat. Mater.* **2011**, *10* (8), 631–636.
(56) Syrenova, S.; Wadell, C.; Nugroho, F. A. A.; Gschneidtner, T. A.; Diaz Fernandez, Y. A.; Nalin, G.; Świtlik, D.; Westerlund, F.; Antosiewicz, T. J.; Zhdanov, V. P.; Moth-Poulsen, K.; Langhammer, C. *Nat. Mater.* **2015**, *14* (12), 1236–1244.
(57) Alekseeva, S.; Fanta, A. B. da S.; Iandolo, B.; Antosiewicz, T. J.; Nugroho, F. A. A.; Wagner, J. B.; Burrows, A.; Zhdanov, V. P.; Langhammer, C. *Nat. Commun.* **2017**, *8* (1), 1084.
(58) Tang, M. L.; Liu, N.; Dionne, J. A.; Alivisatos, A. P. *J. Am. Chem. Soc.* **2011**, *133* (34), 13220–13223.
(59) Baldi, A.; Narayan, T. C.; Koh, A. L.; Dionne, J. A. *Nat. Mater.* **2014**, *13* (12), 1143.
(60) Isaac, N. A.; Ngene, P.; Westerwaal, R. J.; Gaury, J.; Dam, B.; Schmidt-Ott, A.;

Biskos, G. *Sensors Actuators B Chem.* **2015**, *221*, 290–296.
(61) Matuschek, M.; Singh, D. P.; Jeong, H.-H.; Nesterov, M.; Weiss, T.; Fischer, P.; Neubrech, F.; Liu, N. *Small* **2017**, 1702990.
(62) Lacis, A. A.; Schmidt, G. A.; Rind, D.; Ruedy, R. A. *Science* **2010**, *330* (6002), 356–359.
(63) Contribution of Working Group III to the Fifth Assessment Report of the Intergovernmental Panel on Climate Change. https://www.ipcc.ch/report/ar5/wg3/ (accessed Dec 11, 2015).
(64) Turino, G. M.; Goldring, R. M.; Heinemann, H. O. Nahas, G., Schaefer, K. E., Eds.; Springer-Verlag: New York; pp 273–281.
(65) Poyart, C. F.; Nahas, G. G.; Vulliemoz, Y. *Mol. Pharmacol.* **1968**, *4* (4), 389–401.
(66) D'Alessandro, D. M.; Smit, B.; Long, J. R. *Angew. Chem. Int. Ed. Engl.* **2010**, *49* (35), 6058–6082.
(67) Gibbins, J.; Chalmers, H. *Energy Policy* **2008**, *36* (12), 4317–4322.
(68) Sumida, K.; Rogow, D. L.; Mason, J. A.; McDonald, T. M.; Bloch, E. D.; Herm, Z. R.; Bae, T.-H.; Long, J. R. *Chem. Rev.* **2012**, *112* (2), 724–781.
(69) Choi, S.; Drese, J. H.; Jones, C. W. *ChemSusChem* **2009**, *2* (9), 796–854.
(70) Bae, Y.-S.; Snurr, R. Q. *Angew. Chem. Int. Ed. Engl.* **2011**, *50* (49), 11586–11596.
(71) Özçelik, V. O.; Gong, K.; White, C. E. *Nano Lett.* **2018**, acs.nanolett.7b04981.
(72) Farha, O. K.; Eryazici, I.; Jeong, N. C.; Hauser, B. G.; Wilmer, C. E.; Sarjeant, A. A.; Snurr, R. Q.; Nguyen, S. T.; Yazaydın, A. Ö.; Hupp, J. T. *J. Am. Chem. Soc.* **2012**, *134* (36), 15016–15021.
(73) Patel, H. A.; Byun, J.; Yavuz, C. T. *ChemSusChem* **2017**, *10* (7), 1303–1317.
(74) Nugent, P.; Belmabkhout, Y.; Burd, S. D.; Cairns, A. J.; Luebke, R.; Forrest, K.; Pham, T.; Ma, S.; Space, B.; Wojtas, L.; Eddaoudi, M.; Zaworotko, M. J. *Nature* **2013**, *495* (7439), 80–84.
(75) Keller, J. U.; Robens, E.; du Fresne von Hohenesche, C. *Characterization of Porous Solids VI, Proceedings of the 6th International Symposium on the Characterization of Porous Solids (COPS-VI)*; Studies in Surface Science and Catalysis; Elsevier, 2002; Vol. 144.
(76) Keller, J. U.; Rave, H.; Staudt, R. *Macromol. Chem. Phys.* **1999**, *200* (10), 2269–2275.
(77) Budd, P. M.; Ghanem, B. S.; Makhseed, S.; McKeown, N. B.; Msayib, K. J.; Tattershall, C. E. *Chem. Commun. (Camb).* **2004**, No. 2, 230–231.
(78) Budd, P. M.; Elabas, E. S.; Ghanem, B. S.; Makhseed, S.; McKeown, N. B.; Msayib, K. J.; Tattershall, C. E.; Wang, D. *Adv. Mater.* **2004**, *16* (5), 456–459.
(79) Budd, P. M.; McKeown, N. B.; Fritsch, D. *Macromol. Symp.* **2006**, *245–246* (1), 403–405.
(80) Robeson, L. M. *J. Memb. Sci.* **2008**, *320* (1–2), 390–400.
(81) Du, N.; Park, H. B.; Robertson, G. P.; Dal-Cin, M. M.; Visser, T.; Scoles, L.; Guiver, M. D. *Nat. Mater.* **2011**, *10* (5), 372–375.
(82) Bohren, C. F.; Huffman, D. R. *Absorption and Scattering of Light by Small Particles*; Wiley-VCH: New York, 2007.
(83) Kreibig, U.; Vollmer, M. *Optical Properties of Metal Clusters*; Springer-Verlag: Berlin Heidelberg, 1995.
(84) Langer, J.; Novikov, S. M.; Liz-Marzán, L. M. *Nanotechnology* **2015**, *26* (32), 322001.
(85) Sönnichsen, C.; Franzl, T.; Wilk, T.; von Plessen, G.; Feldmann, J.; Wilson, O.; Mulvaney, P. *Phys. Rev. Lett.* **2002**, *88* (7), 077402.
(86) Sönnichsen, C.; Geier, S.; Hecker, N. E.; von Plessen, G.; Feldmann, J.; Ditlbacher, H.; Lamprecht, B.; Krenn, J. R.; Aussenegg, F. R.; Chan, V. Z.-H.; Spatz, J. P.; Möller, M. *Appl. Phys. Lett.* **2000**, *77* (19), 2949.
(87) Langhammer, C.; Kasemo, B.; Zorić, I. *J. Chem. Phys.* **2007**, *126* (19), 194702.

(88) Jain, P. K.; Lee, K. S.; El-Sayed, I. H.; El-Sayed, M. A. *J. Phys. Chem. B* **2006**, *110* (14), 7238–7248.
(89) Meier, M.; Wokaun, A. *Opt. Lett.* **1983**, *8* (11), 581.
(90) Wokaun, A.; Gordon, J. P.; Liao, P. F. *Phys. Rev. Lett.* **1982**, *48* (14), 957–960.
(91) Kreibig, U.; Schmitz, B.; Breuer, H. D. *Phys. Rev. B* **1987**, *36* (9), 5027–5030.
(92) Naik, G. V.; Kim, J.; Boltasseva, A. *Opt. Mater. Express* **2011**, *1* (6), 1090.
(93) Li, D.; Ning, C. Z. *Opt. Express* **2011**, *19* (15), 14594.
(94) Law, S.; Yu, L.; Rosenberg, A.; Wasserman, D. *Nano Lett.* **2013**, *13* (9), 4569–4574.
(95) Naik, G. V.; Boltasseva, A. *Phys. status solidi - Rapid Res. Lett.* **2010**, *4* (10), 295–297.
(96) Johnson, P. B.; Christy, R. W. *Phys. Rev. B* **1972**, *6* (12), 4370–4379.
(97) Langhammer, C.; Yuan, Z.; Zorić, I.; Kasemo, B. *Nano Lett.* **2006**, *6* (4), 833–838.
(98) Zorić, I.; Zäch, M.; Kasemo, B.; Langhammer, C. *ACS Nano* **2011**, *5* (4), 2535–2546.
(99) Chen, J.; Albella, P.; Pirzadeh, Z.; Alonso-González, P.; Huth, F.; Bonetti, S.; Bonanni, V.; Åkerman, J.; Nogués, J.; Vavassori, P.; Dmitriev, A.; Aizpurua, J.; Hillenbrand, R. *Small* **2011**, *7* (16), 2341–2347.
(100) Strohfeldt, N.; Tittl, A.; Schäferling, M.; Neubrech, F.; Kreibig, U.; Griessen, R.; Giessen, H. *Nano Lett.* **2014**, *14* (3), 1140–1147.
(101) Schwind, M.; Zhdanov, V. P.; Zorić, I.; Kasemo, B. *Nano Lett.* **2010**, *10* (3), 931–936.
(102) Schwind, M.; Hosseinpour, S.; Langhammer, C.; Zoric, I.; Leygraf, C.; Kasemo, B. *J. Electrochem. Soc.* **2013**, *160* (10), C487–C492.
(103) Knight, M. W.; Liu, L.; Wang, Y.; Brown, L.; Mukherjee, S.; King, N. S.; Everitt, H. O.; Nordlander, P.; Halas, N. J. *Nano Lett.* **2012**, *12* (11), 6000–6004.
(104) Langhammer, C.; Schwind, M.; Kasemo, B.; Zorić, I. *Nano Lett.* **2008**, *8* (5), 1461–1471.
(105) Sterl, F.; Strohfeldt, N.; Walter, R.; Griessen, R.; Tittl, A.; Giessen, H. *Nano Lett.* **2015**, *15* (12), 7949–7955.
(106) Nugroho, F. A. A.; Iandolo, B.; Wagner, J. B.; Langhammer, C. *ACS Nano* **2016**, *10* (2), 2871–2879.
(107) Cortie, M. B.; McDonagh, A. M. *Chem. Rev.* **2011**, *111* (6), 3713–3735.
(108) Gong, C.; Leite, M. S. *ACS Photonics* **2016**, *3* (4), 507–513.
(109) Gong, C.; Dias, M. R. S.; Wessler, G. C.; Taillon, J. A.; Salamanca-Riba, L. G.; Leite, M. S. *Adv. Opt. Mater.* **2017**, *5* (1), 1600568.
(110) Link, S.; Wang, Z. L.; El-Sayed, M. A. *J. Phys. Chem. B* **1999**, *103* (18), 3529–3533.
(111) Zhang, H.; Jin, R.; Mirkin, C. A. *Nano Lett.* **2004**, *4* (8), 1493–1495.
(112) Mallin, M. P.; Murphy, C. J. *Nano Lett.* **2002**, *2* (11), 1235–1237.
(113) Wang, G.; Xiao, L.; Huang, B.; Ren, Z.; Tang, X.; Zhuang, L.; Lu, J. *J. Mater. Chem.* **2012**, *22* (31), 15769.
(114) Silkin, V. M.; Chernov, I. P.; Echenique, P. M.; Koroteev, Y. M.; Chulkov, E. V. *Phys. Rev. B* **2007**, *76* (24), 245105.
(115) Silkin, V. M.; Díez Muiño, R.; Chernov, I. P.; Chulkov, E. V; Echenique, P. M. *J. Phys. Condens. Matter* **2012**, *24* (10), 104021.
(116) Mock, J. J.; Barbic, M.; Smith, D. R.; Schultz, D. A.; Schultz, S. *J. Chem. Phys.* **2002**, *116* (15), 6755.
(117) Burgin, J.; Liu, M.; Guyot-Sionnest, P. *J. Phys. Chem. C* **2008**, *112* (49), 19279–19282.
(118) Banholzer, M. J.; Harris, N.; Millstone, J. E.; Schatz, G. C.; Mirkin, C. A. *J. Phys. Chem. C* **2010**, *114* (16), 7521–7526.
(119) Dahmen, C.; von Plessen, G. *Aust. J. Chem.* **2007**, *60* (7), 447.
(120) Hu, M.; Chen, J.; Li, Z.-Y.; Au, L.; Hartland, G. V; Li, X.; Marquez, M.; Xia, Y. *Chem. Soc. Rev.* **2006**, *35* (11), 1084–1094.
(121) Eustis, S.; el-Sayed, M. A. *Chem. Soc. Rev.* **2006**, *35* (3), 209–217.

(122) Jensen, T. R.; Malinsky, M. D.; Haynes, C. L.; Van Duyne, R. P. **2000**.
(123) Jensen, T. R.; Duval, M. L.; Kelly, K. L.; Lazarides, A. A.; Schatz, G. C.; Van Duyne, R. P. **1999**.
(124) Englebienne, P. *Analyst* **1998**, *123* (7), 1599–1603.
(125) Larsson, E. M. Nanoplasmonic Sensing - from Biology to Catalysis, Chalmers University of Technology, 2009.
(126) Schwind, M.; Langhammer, C.; Kasemo, B.; Zorić, I. *Appl. Surf. Sci.* **2011**, *257* (13), 5679–5687.
(127) Jackman, J. A.; Rahim Ferhan, A.; Cho, N.-J. *Chem. Soc. Rev.* **2017**, *46* (12), 3615–3660.
(128) Ferhan, A. R.; Jackman, J. A.; Park, J. H.; Cho, N.-J.; Kim, D.-H. *Adv. Drug Deliv. Rev.* **2017**.
(129) Olofsson, L.; Rindzevicius, T.; Pfeiffer, I.; Käll, M.; Höök, F. *Langmuir* **2003**, *19* (24), 10414–10419.
(130) Morokoshi, S.; Ohhori, K.; Mizukami, K.; Kitano, H. *Langmuir* **2004**, *20* (20), 8897–8902.
(131) Yonzon, C. R.; Jeoung, E.; Zou, S.; Schatz, G. C.; Mrksich, M.; Van Duyne, R. P. *J. Am. Chem. Soc.* **2004**, *126* (39), 12669–12676.
(132) Dahlin, A.; Zäch, M.; Rindzevicius, T.; Käll, M.; Sutherland, D. S.; Höök, F. *J. Am. Chem. Soc.* **2005**, *127* (14), 5043–5048.
(133) Nath, N.; Chilkoti, A. *Anal. Chem.* **2002**, *74* (3), 504–509.
(134) Haes, A. J.; Hall, W. P.; Chang, L.; Klein, W. L.; Van Duyne, R. P. *Nano Lett.* **2004**, *4* (6), 1029–1034.
(135) Voller, A.; Bartlett, A.; Bidwell, D. E. *J. Clin. Pathol.* **1978**, *31* (6), 507–520.
(136) Langhammer, C.; Larsson, E. M. *ACS Catal.* **2012**, *2* (9), 2036–2045.
(137) Marimuthu, A.; Zhang, J.; Linic, S. *Science* **2013**, *339* (6127), 1590–1593.
(138) Seo, D.; Park, G.; Song, H. *J. Am. Chem. Soc.* **2012**, *134* (2), 1221–1227.
(139) Li, K.; Wang, K.; Qin, W.; Deng, S.; Li, D.; Shi, J.; Huang, Q.; Fan, C. *J. Am. Chem. Soc.* **2015**, *137* (13), 4292–4295.
(140) Collins, S. S. E.; Cittadini, M.; Pecharromán, C.; Martucci, A.; Mulvaney, P. *ACS Nano* **2015**, *9* (8), 7846–7856.
(141) Sirinakis, G.; Siddique, R.; Manning, I.; Rogers, P. H.; Carpenter, M. A. *J. Phys. Chem. B* **2006**, *110* (27), 13508–13511.
(142) Ando, M.; Kobayashi, T.; Iijima, S.; Haruta, M. *Sensors Actuators B Chem.* **2003**, *96* (3), 589–595.
(143) Tittl, A.; Mai, P.; Taubert, R.; Dregely, D.; Liu, N.; Giessen, H. *Nano Lett.* **2011**, *11* (10), 4366–4369.
(144) Wadell, C.; Nugroho, F. A. A.; Lidström, E.; Iandolo, B.; Wagner, J. B.; Langhammer, C. *Nano Lett.* **2015**, *15* (5), 3563–3570.
(145) Taylor, A. B.; Zijlstra, P. *ACS Sensors* **2017**, *2* (8), 1103–1122.
(146) Dmitriev, A.; Hägglund, C.; Chen, S.; Fredriksson, H.; Pakizeh, T.; Käll, M.; Sutherland, D. S. *Nano Lett.* **2008**, *8* (11), 3893–3898.
(147) Langhammer, C.; Larsson, E. M.; Kasemo, B.; Zorić, I. *Nano Lett.* **2010**, *10* (9), 3529–3538.
(148) Galush, W. J.; Shelby, S. A.; Mulvihill, M. J.; Tao, A.; Yang, P.; Groves, J. T. *Nano Lett.* **2009**, *9* (5), 2077–2082.
(149) Zhang, S.; Bao, K.; Halas, N. J.; Xu, H.; Nordlander, P. *Nano Lett.* **2011**, *11* (4), 1657–1663.
(150) Hao, F.; Nehl, C. L.; Hafner, J. H.; Nordlander, P. *Nano Lett.* **2007**, *7* (3), 729–732.
(151) Shegai, T.; Langhammer, C. *Adv. Mater.* **2011**, *23* (38), 4409–4414.
(152) Fritzsche, J.; Albinsson, D.; Fritzsche, M.; Antosiewicz, T. J.; Westerlund, F.;

Langhammer, C. *Nano Lett.* **2016**, *16* (12), 7857–7864.
(153) Langhammer, C.; Larsson, E. M.; Zhdanov, V. P.; Zorić, I. *J. Phys. Chem. C* **2012**, *116* (40), 21201–21207.
(154) Susman, M. D.; Feldman, Y.; Bendikov, T. A.; Vaskevich, A.; Rubinstein, I. *Nanoscale* **2017**, *9* (34), 12573–12589.
(155) Mohammadpour, Z.; Safavi, A.; Abdollahi, S. H. *Anal. Chim. Acta* **2017**, *959*, 74–82.
(156) Larsson, E. M.; Langhammer, C.; Zorić, I.; Kasemo, B. *Science* **2009**, *326* (5956), 1091–1094.
(157) Tabib Zadeh Adibi, P.; Mazzotta, F.; Antosiewicz, T. J.; Skoglundh, M.; Grönbeck, H.; Langhammer, C. *ACS Catal.* **2015**, *5* (1), 426–432.
(158) Wettergren, K.; Hellman, A.; Cavalca, F.; Zhdanov, V. P.; Langhammer, C. *Nano Lett.* **2015**, *15* (1), 574–580.
(159) Nugroho, F. A. A.; Diaz de Zerio Mendaza, A.; Lindqvist, C.; Antosiewicz, T. J.; Müller, C.; Langhammer, C. *Anal. Chem.* **2017**, *89* (4), 2575–2582.
(160) Diaz de Zerio Mendaza, A.; Melianas, A.; Nugroho, F. A. A.; Bäcke, O.; Olsson, E.; Langhammer, C.; Inganäs, O.; Müller, C. *J. Mater. Chem. A* **2017**, *5* (8), 4156–4162.
(161) Jackman, J. A.; Zhdanov, V. P.; Cho, N.-J. **2014**.
(162) Jackman, J. A.; Špačková, B.; Linardy, E.; Kim, M. C.; Yoon, B. K.; Homola, J.; Cho, N.-J. *Chem. Commun.* **2016**, *52* (1), 76–79.
(163) Oh, E.; Jackman, J. A.; Yorulmaz, S.; Zhdanov, V. P.; Lee, H.; Cho, N.-J. **2015**.
(164) Nugroho, F. A. A.; Frost, R.; Antosiewicz, T. J.; Fritzsche, J.; Larsson Langhammer, E. M.; Langhammer, C. *ACS Sensors* **2017**, *2* (1), 119–127.
(165) Zhang, C.; Zhao, H.; Zhou, L.; Schlather, A. E.; Dong, L.; McClain, M. J.; Swearer, D. F.; Nordlander, P.; Halas, N. J. *Nano Lett.* **2016**, *16* (10), 6677–6682.
(166) Swearer, D. F.; Zhao, H.; Zhou, L.; Zhang, C.; Robatjazi, H.; Martirez, J. M. P.; Krauter, C. M.; Yazdi, S.; McClain, M. J.; Ringe, E.; Carter, E. A.; Nordlander, P.; Halas, N. J. *Proc. Natl. Acad. Sci. U. S. A.* **2016**, *113* (32), 8916–8920.
(167) Wadell, C.; Langhammer, C. *Nanoscale* **2015**, *7* (25), 10963–10969.
(168) Syrenova, S.; Wadell, C.; Langhammer, C. *Nano Lett.* **2014**, *14* (5), 2655–2663.
(169) Liu, H.; Nosheen, F.; Wang, X. *Chem. Soc. Rev.* **2015**, *44* (10), 3056–3078.
(170) You, H.; Yang, S.; Ding, B.; Yang, H. *Chem. Soc. Rev.* **2013**, *42* (7), 2880–2904.
(171) Ferrando, R.; Jellinek, J.; Johnston, R. L. *Chem. Rev.* **2008**.
(172) Gilroy, K. D.; Ruditskiy, A.; Peng, H.-C.; Qin, D.; Xia, Y. *Chem. Rev.* **2016**, *116* (18), 10414–10472.
(173) Wang, D.; Li, Y. *Adv. Mater.* **2011**, *23* (9), 1044–1060.
(174) *Alloy Phase Diagrams*; Baker, H., Ed.; ASM International: Materials Park, OH, 1992.
(175) Predel, B. In *Ac-Au – Au-Zr*; Springer-Verlag: Berlin/Heidelberg; pp 1–4.
(176) Zhang, K.; Way, J. D. *Sep. Purif. Technol.* **2017**, *186*, 39–44.
(177) Subramanian, P. .; Laughlin, D. . *J. Phase Equilibria* **1991**, *12* (2), 231–243.
(178) Kamakoti, P.; Morreale, B. D.; Ciocco, M. V; Howard, B. H.; Killmeyer, R. P.; Cugini, A. V; Sholl, D. S. *Science* **2005**, *307* (5709), 569–573.
(179) Sonwane, C. G.; Wilcox, J.; Ma, Y. H. *J. Chem. Phys.* **2006**, *125* (18), 184714.
(180) Howard, B. .; Killmeyer, R. .; Rothenberger, K. .; Cugini, A. .; Morreale, B. .; Enick, R. .; Bustamante, F. *J. Memb. Sci.* **2004**, *241* (2), 207–218.
(181) Liu, X.; Wang, D.; Li, Y. *Nano Today* **2012**, *7* (5), 448–466.
(182) Noh, H.; Flanagan, T. B.; Gavra, Z.; Johnson, J. R.; Reilly, J. J. *Scr. Metall. Mater.* **1991**, *25* (9), 2177–2180.
(183) Lee, E.; Lee, J. M.; Lee, E.; Noh, J.-S.; Joe, J. H.; Jung, B.; Lee, W. *Thin Solid Films* **2010**, *519* (2), 880–884.
(184) Burch, R.; Buss, R. G. *J. Chem. Soc. Faraday Trans. 1 Phys. Chem. Condens. Phases* **1975**, *71* (0), 913.

(185) Luo, S.; Wang, D.; Flanagan, T. B. *J. Phys. Chem. B* **2010**, *114* (18), 6117–6125.
(186) Westerwaal, R. J.; Rooijmans, J. S. A.; Leclercq, L.; Gheorghe, D. G.; Radeva, T.; Mooij, L.; Mak, T.; Polak, L.; Slaman, M.; Dam, B.; Rasing, T. *Int. J. Hydrogen Energy* **2013**, *38* (10), 4201–4212.
(187) Hughes, R. C.; Schubert, W. K.; Zipperian, T. E.; Rodriguez, J. L.; Plut, T. A. *J. Appl. Phys.* **1987**, *62* (3), 1074.
(188) Zhao, Z.; Sevryugina, Y.; Carpenter, M. A.; Welch, D.; Xia, H. *Anal. Chem.* **2004**, *76* (21), 6321–6326.
(189) Amandusson, H.; Ekedahl, L.-G.; Dannetun, H. *J. Memb. Sci.* **2001**, *193* (1), 35–47.
(190) Debauge, Y.; Abon, M.; Bertolini, J. C.; Massardier, J.; Rochefort, A. *Appl. Surf. Sci.* **1995**, *90*, 15–27.
(191) Rochefort, A.; Abon, M.; Delichère, P.; Bertolini, J. C. *Surf. Sci.* **1993**, *294* (1–2), 43–52.
(192) Illas, F.; López, N.; Ricart, J. M.; Clotet, A.; Conesa, J. C.; Fernández-García, M. *J. Phys. Chem. B* **1998**, *102* (41), 8017–8023.
(193) O'Brien, C. P.; Lee, I. C. *J. Phys. Chem. C* **2017**, *121* (31), 16864–16871.
(194) O'Brien, C. P.; Lee, I. C. *Catalysis Today*. September 2017.
(195) Burton, J. J.; Hyman, E.; Fedak, D. G. *J. Catal.* **1975**, *37* (1), 106–113.
(196) Løvvik, O. M. *Surf. Sci.* **2005**, *583* (1), 100–106.
(197) Deng, L.; Hu, W.; Deng, H.; Xiao, S.; Tang, J. *J. Phys. Chem. C* **2011**, *115* (23), 11355–11363.
(198) Deng, L.; Hu, W.; Deng, H.; Xiao, S. *J. Phys. Chem. C* **2010**, *114* (25), 11026–11032.
(199) Park, J. Y.; Zhang, Y.; Joo, S. H.; Jung, Y.; Somorjai, G. A. *Catal. Today* **2012**, *181* (1), 133–137.
(200) Cui, C.; Gan, L.; Heggen, M.; Rudi, S.; Strasser, P. *Nat. Mater.* **2013**, *12* (8), 765–771.
(201) Tománek, D.; Mukherjee, S.; Kumar, V.; Bennemann, K. H. *Surf. Sci.* **1982**, *114* (1), 11–22.
(202) Rousset, J. L.; Bertolini, J. C.; Miegge, P. *Phys. Rev. B* **1996**, *53* (8), 4947–4957.
(203) Tarditi, A. M.; Imhoff, C.; Miller, J. B.; Cornaglia, L. *Surf. Interface Anal.* **2015**, *47* (7), 745–754.
(204) Zhao, M.; Sloof, W. G.; Böttger, A. J. *Int. J. Hydrogen Energy* **2018**, *43* (4), 2212–2223.
(205) Miller, J. B.; Matranga, C.; Gellman, A. J. *Surf. Sci.* **2008**, *602* (1), 375–382.
(206) Grzelczak, M.; Pérez-Juste, J.; Mulvaney, P.; Liz-Marzán, L. M. *Chem. Soc. Rev.* **2008**, *37* (9), 1783–1791.
(207) Niu, W.; Zhang, L.; Xu, G. *ACS Nano* **2010**, *4* (4), 1987–1996.
(208) Guisbiers, G.; Mendoza-Cruz, R.; Bazán-Díaz, L.; Velázquez-Salazar, J. J.; Mendoza-Perez, R.; Robledo-Torres, J. A.; Rodriguez-Lopez, J.-L.; Montejano-Carrizales, J. M.; Whetten, R. L.; José-Yacamán, M. *ACS Nano* **2016**, *10* (1), 188–198.
(209) Zhang, Q.; Xie, J.; Liang, J.; Lee, J. Y. *Adv. Funct. Mater.* **2009**, *19* (9), 1387–1398.
(210) Liu, S.; Chen, G.; Prasad, P. N.; Swihart, M. T. *Chem. Mater.* **2011**, *23* (18), 4098–4101.
(211) Sánchez-Ramírez, J. F.; Pal, U.; Nolasco-Hernández, L.; Mendoza-Álvarez, J.; Pescador-Rojas, J. A. *J. Nanomater.* **2008**, 620412.
(212) Gonzalez, C. M.; Liu, Y.; Scaiano, J. C. *J. Phys. Chem. C* **2009**, *113* (27), 11861–11867.
(213) Zhang, J.; Yang, H.; Fang, J.; Zou, S. *Nano Lett.* **2010**, *10* (2), 638–644.
(214) Yin, A.-X.; Min, X.-Q.; Zhang, Y.-W.; Yan, C.-H. *J. Am. Chem. Soc.* **2011**, *133* (11), 3816–3819.
(215) Wu, Y.; Cai, S.; Wang, D.; He, W.; Li, Y. *J. Am. Chem. Soc.* **2012**, *134* (21), 8975–8981.

(216) Kim, D.; Resasco, J.; Yu, Y.; Asiri, A. M.; Yang, P. *Nat. Commun.* **2014**, *5*, 4948.
(217) Ely, T. O.; Amiens, C.; Chaudret, B.; Etienne, S.; Verelst, M.; Respaud, M.; Broto, J.-M. **1999**.
(218) Park, S.-J.; Kim, S.; Lee, S.; Khim, Z. G.; Char, K.; Hyeon, T. **2000**.
(219) Shouheng Sun; Fullerton, E. E.; Weller, D.; Murray, C. B. *IEEE Trans. Magn.* **2001**, *37* (4), 1239–1243.
(220) Sun, S.; Murray, C. B.; Weller, D.; Folks, L.; Moser, A. *Science* **2000**, *287* (5460), 1989–1992.
(221) Sun, S. *Adv. Mater.* **2006**, *18* (4), 393–403.
(222) Rutledge, R. D.; Morris, W. H.; Wellons, M. S.; Gai, Z.; Shen, J.; Bentley, J.; Wittig, J. E.; Lukehart, C. M. **2006**.
(223) Robinson, I.; Zacchini, S.; Tung, L. D.; Maenosono, S.; Thanh, N. T. K. *Chem. Mater.* **2009**, *21* (13), 3021–3026.
(224) Sra, A. K.; Schaak, R. E. *J. Am. Chem. Soc.* **2004**, *126* (21), 6667–6672.
(225) Chen, W.; Yu, R.; Li, L.; Wang, A.; Peng, Q.; Li, Y. *Angew. Chemie* **2010**, *122* (16), 2979–2983.
(226) Wang, T.; Pearson, A. J.; Dunbar, A. D. F.; Staniec, P. A.; Watters, D. C.; Yi, H.; Ryan, A. J.; Jones, R. A. L.; Iraqi, A.; Lidzey, D. G. *Adv. Funct. Mater.* **2012**, *22* (7), 1399–1408.
(227) Wu, M.-L.; Chen, D.-H.; Huang, T.-C. *Langmuir* **2001**, *17* (13), 3877–3883.
(228) Kan, C.; Cai, W.; Li, C.; Zhang, L.; Hofmeister, H. *J. Phys. D. Appl. Phys.* **2003**, *36* (13), 1609–1614.
(229) Jana, N. R.; Gearheart, L.; Murphy, C. J. **2001**.
(230) Jana, N. R.; Gearheart, L.; Murphy, C. J. **2001**.
(231) Jana, N. R.; Gearheart, L.; Murphy, C. J. *Chem. Commun.* **2001**, *0* (7), 617–618.
(232) Wang, Y.; Peng, H.-C.; Liu, J.; Huang, C. Z.; Xia, Y. *Nano Lett.* **2015**, *15* (2), 1445–1450.
(233) Xiong, Y.; Xia, Y. *Adv. Mater.* **2007**, *19* (20), 3385–3391.
(234) Rioux, D.; Meunier, M. *J. Phys. Chem. C* **2015**, *119* (23), 13160–13168.
(235) Xu, M.; Feng, J.; Liu, Y.-S.; Jin, Y.; Wang, H.-Y.; Sun, H.-B. *Appl. Phys. Lett.* **2014**, *105* (15), 153303.
(236) Verma, S.; Rao, B. T.; Detty, A. P.; Ganesan, V.; Phase, D. M.; Rai, S. K.; Bose, A.; Joshi, S. C.; Kukreja, L. M. *J. Appl. Phys.* **2015**, *117* (13), 133105.
(237) Thompson, C. V. *Annu. Rev. Mater. Res.* **2012**, *42* (1), 399–434.
(238) Kang, M.; Ahn, M.-S.; Lee, Y.; Jeong, K.-H. *ACS Appl. Mater. Interfaces* **2017**, *9* (42), 37154–37159.
(239) Park, M.; Hwang, C. S. H.; Jeong, K.-H. *ACS Appl. Mater. Interfaces* **2018**, *10* (1), 290–295.
(240) Qiu, G.; Ng, S. P.; Wu, C.-M. L. *Sensors Actuators B Chem.* **2018**.
(241) Kunwar, S.; Pandey, P.; Sui, M.; Bastola, S.; Lee, J. *Metals (Basel).* **2017**, *7* (12), 472.
(242) Graham, T. *Philos. Trans. R. Soc. London* **1866**, *156* (0), 399–439.
(243) Wadell, C.; Pingel, T.; Olsson, E.; Zorić, I.; Zhdanov, V. P.; Langhammer, C. *Chem. Phys. Lett.* **2014**, *603*, 75–81.
(244) Gdowski, G. E.; Felter, T. E.; Stulen, R. H. *Surf. Sci.* **1987**, *181* (3), L147–L155.
(245) Okuyama, H.; Siga, W.; Takagi, N.; Nishijima, M.; Aruga, T. *Surf. Sci.* **1998**, *401* (3), 344–354.
(246) Cattania, M. G.; Penka, V.; Behm, R. J.; Christmann, K.; Ertl, G. *Surf. Sci.* **1983**, *126* (1–3), 382–391.
(247) Langhammer, C.; Zhdanov, V. P.; Zorić, I.; Kasemo, B. *Phys. Rev. Lett.* **2010**, *104* (13), 135502.
(248) Behm, R. J.; Christmann, K.; Ertl, G. *Surf. Sci.* **1980**, *99* (2), 320–340.

(249) Conrad, H.; Ertl, G.; Latta, E. E. *Surf. Sci.* **1974**, *41* (2), 435–446.
(250) *Hydrogen in Intermetallic Compunds II*; Schlapbach, L., Ed.; Topics in Applied Physics; Springer Berlin Heidelberg: Berlin, Heidelberg, 1992; Vol. 67.
(251) Christmann, K. *Surf. Sci. Rep.* **1988**, *9* (1–3), 1–163.
(252) Li, G.; Kobayashi, H.; Dekura, S.; Ikeda, R.; Kubota, Y.; Kato, K.; Takata, M.; Yamamoto, T.; Matsumura, S.; Kitagawa, H. *J. Am. Chem. Soc.* **2014**, *136* (29).
(253) Sieverts, A. *Zeitschrift für Met.* **1929**, *21*, 37.
(254) Fukai, Y. *The Metal-Hydrogen System*; Springer-Verlag, 1993.
(255) Wicke, E.; Brodowsky, H.; Züchner, H. Springer Berlin Heidelberg, 1978; pp 73–155.
(256) Wadell, C. Plasmonic Nanostructures for Optical Absorption Engineering and Hydrogen Sensing, Chalmers University of Technology, 2015.
(257) Lejcek, P. *Grain Boundary Segregation in Metals*; Springer Series in Materials Science; Springer Berlin Heidelberg: Berlin, Heidelberg, 2010; Vol. 136.
(258) Herbig, M.; Raabe, D.; Li, Y. J.; Choi, P.; Zaefferer, S.; Goto, S. *Phys. Rev. Lett.* **2014**, *112* (12), 126103.
(259) Frolov, T.; Divinski, S. V.; Asta, M.; Mishin, Y. *Phys. Rev. Lett.* **2013**, *110* (25), 255502.
(260) Delmelle, R.; Amin-Ahmadi, B.; Sinnaeve, M.; Idrissi, H.; Pardoen, T.; Schryvers, D.; Proost, J. *Int. J. Hydrogen Energy* **2015**, *40* (23), 7335–7347.
(261) Narayan, T. C.; Baldi, A.; Koh, A. L.; Sinclair, R.; Dionne, J. A. *Nat. Mater.* **2016**, *15* (April).
(262) Bérubé, V.; Radtke, G.; Dresselhaus, M.; Chen, G. *Int. J. Energy Res.* **2007**, *31* (6–7), 637–663.
(263) Sachs, C.; Pundt, A.; Kirchheim, R.; Winter, M.; Reetz, M. T.; Fritsch, D. *Phys. Rev. B* **2001**, *64* (7), 075408.
(264) Pundt, A.; Sachs, C.; Winter, M.; Reetz, M. .; Fritsch, D.; Kirchheim, R. *J. Alloys Compd.* **1999**, *293–295*, 480–483.
(265) Pundt, A.; Suleiman, M.; Bähtz, C.; Reetz, M. T.; Kirchheim, R.; Jisrawi, N. M. *Mater. Sci. Eng. B* **2004**, *108* (1–2), 19–23.
(266) Langhammer, C.; Zhdanov, V. P.; Zorić, I.; Kasemo, B. *Chem. Phys. Lett.* **2010**, *488* (1–3), 62–66.
(267) Yamauchi, M.; Ikeda, R.; Kitagawa, H.; Takata, M. **2008**.
(268) Narehood, D. G.; Kishore, S.; Goto, H.; Adair, J. H.; Nelson, J. A.; Gutiérrez, H. R.; Eklund, P. C. *Int. J. Hydrogen Energy* **2009**, *34* (2), 952–960.
(269) Griessen, R.; Strohfeldt, N.; Giessen, H. *Nat. Mater.* **2015**, *15* (November).
(270) Bardhan, R.; Hedges, L. O.; Pint, C. L.; Javey, A.; Whitelam, S.; Urban, J. J. *Nat. Mater.* **2013**, *12* (10).
(271) Ulvestad, A.; Yau, A. *Nat. Commun.* **2017**, *8* (1), 1376.
(272) Gryaznov, V. M. *Platin. Met. Rev.* **1986**, *30* (2), 68–72.
(273) Uemiya, S.; Matsuda, T.; Kikuchi, E. *J. Memb. Sci.* **1991**, *56* (3), 315–325.
(274) Holleck, G. L. *J. Phys. Chem.* **1970**, *74* (3), 503–511.
(275) Vegard, L. *Zeitschrift für Phys.* **1921**, *5* (1), 17–26.
(276) Alefeld, G.; Völkl, J. *Hydrogen in Metals II*; Springer: Berlin Heidelberg, 1978.
(277) Alefeld, G.; Völkl, J. *Hydrogen in metals I - Basic properties*; Alefeld, G., Völkl, J., Eds.; Springer Berlin Heidelberg, 1978.
(278) Westerwaal, R. J.; Gersen, S.; Ngene, P.; Darmeveil, H.; Schreuders, H.; Middelkoop, J.; Dam, B. *Sensors Actuators B Chem.* **2014**, *199*, 127–132.
(279) Opalka, S. M.; Huang, W.; Wang, D.; Flanagan, T. B.; Løvvik, O. M.; Emerson, S. C.; She, Y.; Vanderspurt, T. H. *J. Alloys Compd.* **2007**, *446*, 583–587.
(280) Mooij, L. P. A.; Baldi, A.; Boelsma, C.; Shen, K.; Wagemaker, M.; Pivak, Y.; Schreuders, H.; Griessen, R.; Dam, B. *Adv. Energy Mater.* **2011**, *1* (5), 754–758.

(281) Zhdanov, V. P. *Mod. Phys. Lett. B* **2016**, *30* (26), 1650330.
(282) Marchal, R.; Genest, A.; Krüger, S.; Rösch, N. *J. Phys. Chem. C* **2013**, *117* (42), 21810–21822.
(283) Sonwane, C. G.; Wilcox, J.; Ma, Y. H. *J. Phys. Chem. B* **2006**, *110* (48), 24549–24558.
(284) Galipaud, J.; Martin, M. H.; Roué, L.; Guay, D. *J. Phys. Chem. C* **2015**, *119* (47), 26451–26458.
(285) Schlapbach, L.; Züttel, A. *Nature* **2001**, *414* (6861), 353–358.
(286) Yoshimura, K.; Langhammer, C.; Dam, B. *MRS Bull.* **2013**, *38* (06), 495–503.
(287) Huiberts, J. N.; Griessen, R.; Rector, J. H.; Wijngaarden, R. J.; Dekker, J. P.; de Groot, D. G.; Koeman, N. J. *Nature* **1996**, *380* (6571), 231–234.
(288) Oumellal, Y.; Rougier, A.; Nazri, G. A.; Tarascon, J.-M.; Aymard, L. *Nat. Mater.* **2008**, *7* (11), 916–921.
(289) Remhof, A.; Borgschulte, A. *ChemPhysChem* **2008**, *9* (17), 2440–2455.
(290) Avila, J. I.; Matelon, R. J.; Trabol, R.; Favre, M.; Lederman, D.; Volkmann, U. G.; Cabrera, A. L. *J. Appl. Phys.* **2010**, *107* (2), 023504.
(291) Şennik, E.; Kılınç, N.; Öztürk, Z. Z. *J. Appl. Phys.* **2010**, *108* (5), 054317.
(292) Lee, E.; Lee, J. M.; Koo, J. H.; Lee, W.; Lee, T. *Int. J. Hydrogen Energy* **2010**, *35* (13), 6984–6991.
(293) Johnson, P. B.; Christy, R. W. *Phys. Rev. B* **1972**, *6* (12), 4370–4379.
(294) Isidorsson, J.; Giebels, I. A. M. E.; Arwin, H.; Griessen, R. *Phys. Rev. B* **2003**, *68* (11), 115112.
(295) Manchester, F. D.; San-Martin, A.; Pitre, J. M. *J. Phase Equilibria* **1994**, *15* (1), 62–83.
(296) Maclntyr, J.; Marshall, T. *Instrum Technol.* **1972**, *18*, 29–32.
(297) Lundström, K. I.; Shivaraman, M. S.; Svensson, C. M. *J. Appl. Phys.* **1975**, *46* (9), 3876–3881.
(298) Butler, M. A. *Appl. Phys. Lett.* **1984**, *45* (10), 1007–1009.
(299) Butler, M. A.; Ginley, D. S. *J. Appl. Phys.* **1988**, *64* (7), 3706–3712.
(300) Armgarth, M.; Nylander, C. *IEEE Electron Device Lett.* **1982**, *3* (12), 384–386.
(301) Sutapun, B.; Tabib-Azar, M.; Kazemi, A. *Sensors Actuators B Chem.* **1999**, *60* (1), 27–34.
(302) Mandelis, A.; Garcia, J. A. *Sensors Actuators B Chem.* **1998**, *49* (3), 258–267.
(303) Tobiška, P.; Hugon, O.; Trouillet, A.; Gagnaire, H. *Sensors Actuators B Chem.* **2001**, *74* (1–3), 168–172.
(304) Sekimoto, S.; Nakagawa, H.; Okazaki, S.; Fukuda, K.; Asakura, S.; Shigemori, T.; Takahashi, S. *Sensors Actuators B Chem.* **2000**, *66* (1–3), 142–145.
(305) Bévenot, X.; Trouillet, A.; Veillas, C.; Gagnaire, H.; Clément, M. *Meas. Sci. Technol.* **2002**, *13* (1), 118–124.
(306) Butler, M. A. *Sensors Actuators B Chem.* **1994**, *22* (2), 155–163.
(307) Favier, F.; Walter, E. C.; Zach, M. P.; Benter, T.; Penner, R. M. *Science (80-.).* **2001**, *2227* (293), 2227--2231.
(308) Walter, E. C.; Favier, F.; Penner, R. M. *Anal. Chem.* **2002**, *74* (7), 1546–1553.
(309) Yang, F.; Kung, S.-C.; Cheng, M.; Hemminger, J. C.; Penner, R. M. *ACS Nano* **2010**, *4* (9), 5233–5244.
(310) Yang, F.; Taggart, D. K.; Penner, R. M. *Small* **2010**, *6* (13), 1422–1429.
(311) Li, X.; Le Thai, M.; Dutta, R. K.; Qiao, S.; Chandran, G. T.; Penner, R. M. *ACS Sensors* **2017**, *2* (2), 282–289.
(312) Li, X.; Liu, Y.; Hemminger, J. C.; Penner, R. M. *ACS Nano* **2015**, *9* (3), 3215–3225.
(313) Koo, W.-T.; Qiao, S.; Ogata, A. F.; Jha, G.; Jang, J.-S.; Chen, V. T.; Kim, I.-D.; Penner, R. M. *ACS Nano* **2017**, *11* (9), 9276–9285.
(314) Gremaud, R.; Broedersz, C. P.; Borsa, D. M.; Borgschulte, A.; Mauron, P.; Schreuders, H.; Rector, J. H.; Dam, B.; Griessen, R. *Adv. Mater.* **2007**, *19* (19), 2813–2817.

(315) Radeva, T.; Ngene, P.; Slaman, M.; Westerwaal, R.; Schreuders, H.; Dam, B. *Sensors Actuators B Chem.* **2014**, *203*, 745–751.
(316) Ngene, P.; Radeva, T.; Slaman, M.; Westerwaal, R. J.; Schreuders, H.; Dam, B. *Adv. Funct. Mater.* **2014**, *24* (16), 2374–2382.
(317) Slaman, M.; Dam, B.; Pasturel, M.; Borsa, D. M.; Schreuders, H.; Rector, J. H.; Griessen, R. *Sensors Actuators B Chem.* **2007**, *123* (1), 538–545.
(318) Boelsma, C.; Bannenberg, L. J.; van Setten, M. J.; Steinke, N.-J.; van Well, A. A.; Dam, B. *Nat. Commun.* **2017**, *8*, 15718.
(319) Perrotton, C.; Westerwaal, R. J.; Javahiraly, N.; Slaman, M.; Schreuders, H.; Dam, B.; Meyrueis, P. *Opt. Express* **2013**, *21* (1), 382.
(320) Victoria, M.; Westerwaal, R. J.; Dam, B.; van Mechelen, J. L. M. *ACS Sensors* **2016**, *1* (3), 222–226.
(321) Borsa, D. M.; Gremaud, R.; Baldi, A.; Schreuders, H.; Rector, J. H.; Kooi, B.; Vermeulen, P.; Notten, P. H. L.; Dam, B.; Griessen, R. *Phys. Rev. B* **2007**, *75* (20), 205408.
(322) Palmisano, V.; Filippi, M.; Baldi, A.; Slaman, M.; Schreuders, H.; Dam, B. *Int. J. Hydrogen Energy* **2010**, *35* (22), 12574–12578.
(323) Ngene, P.; Longo, A.; Mooij, L.; Bras, W.; Dam, B. *Nat. Commun.* **2017**, *8* (1), 1846.
(324) Lee, J.; Shim, W.; Lee, E.; Noh, J.-S.; Lee, W. *Angew. Chemie Int. Ed.* **2011**, *50* (23), 5301–5305.
(325) Lim, S. H.; Radha, B.; Chan, J. Y.; Saifullah, M. S. M.; Kulkarni, G. U.; Ho, G. W. *ACS Appl. Mater. Interfaces* **2013**, *5* (15), 7274–7281.
(326) Xu, T.; Zach, M. P.; Xiao, Z. L.; Rosenmann, D.; Welp, U.; Kwok, W. K.; Crabtree, G. W. *Appl. Phys. Lett.* **2005**, *86* (20), 1–3.
(327) Pak, Y.; Lim, N.; Kumaresan, Y.; Lee, R.; Kim, K.; Kim, T. H.; Kim, S.-M.; Kim, J. T.; Lee, H.; Ham, M.-H.; Jung, G.-Y. *Adv. Mater.* **2015**, *27* (43), 6945–6952.
(328) Hughes, R. C.; Schubert, W. K. *J. Appl. Phys.* **1992**, *71* (1), 542–544.
(329) Lupan, O.; Postica, V.; Labat, F.; Ciofini, I.; Pauporté, T.; Adelung, R. *Sensors Actuators B Chem.* **2018**, *254*, 1259–1270.
(330) Offermans, P.; Tong, H. D.; van Rijn, C. J. M.; Merken, P.; Brongersma, S. H.; Crego-Calama, M. *Appl. Phys. Lett.* **2009**, *94* (22), 223110.
(331) Villatoro, J.; Monzón-Hernández, D. *Opt. Express* **2005**, *13* (13), 5087.
(332) Monzón-Hernández, D.; Luna-Moreno, D.; Martínez-Escobar, D. *Sensors Actuators B Chem.* **2009**, *136* (2), 562–566.
(333) Zhao, Z.; Carpenter, M. A.; Xia, H.; Welch, D. *Sensors Actuators B Chem.* **2006**, *113* (1), 532–538.
(334) Liu, K.; Song, C.; Subramani, V. *Hydrogen and Syngas Production and Purification Technologies*; Liu, K., Song, C., Subramani, V., Eds.; John Wiley & Sons, Inc.: Hoboken, NJ, USA, 2009.
(335) Shao, L.; Low, B. T.; Chung, T.-S.; Greenberg, A. R. *J. Memb. Sci.* **2009**, *327* (1–2), 18–31.
(336) Rochefort, A.; Fournier, R. *J. Phys. Chem.* **1996**, *100* (32), 13506–13513.
(337) Hong, J.; Lee, S.; Seo, J.; Pyo, S.; Kim, J.; Lee, T. *ACS Appl. Mater. Interfaces* **2015**, *7* (6), 3554–3561.
(338) Jeon, K.-J.; Moon, H. R.; Ruminski, A. M.; Jiang, B.; Kisielowski, C.; Bardhan, R.; Urban, J. J. *Nat. Mater.* **2011**, *10* (4), 286–290.
(339) Nyberg, C.; Tengstål, C. G. *J. Chem. Phys.* **1984**, *80* (7), 3463–3468.
(340) Ngene, P.; Westerwaal, R. J.; Sachdeva, S.; Haije, W.; de Smet, L. C. P. M.; Dam, B. *Angew. Chemie Int. Ed.* **2014**, *53* (45), 12081–12085.
(341) Delmelle, R.; Ngene, P.; Dam, B.; Bleiner, D.; Borgschulte, A. *ChemCatChem* **2016**, *8* (9), 1646–1650.

(342) Li, G.; Kobayashi, H.; Taylor, J. M.; Ikeda, R.; Kubota, Y.; Kato, K.; Takata, M.; Yamamoto, T.; Toh, S.; Matsumura, S.; Kitagawa, H. *Nat. Mater.* **2014**, *13* (8), 802–806.
(343) Nanba, Y.; Tsutsumi, T.; Ishimoto, T.; Koyama, M. *J. Phys. Chem. C* **2017**, *121* (27), 14611–14617.
(344) Zoric´, I.; Larsson, E. M.; Kasemo, B.; Langhammer, C. *Adv. Mater.* **2010**, *22* (41), 4628–4633.
(345) Niu, W.; Zhang, W.; Firdoz, S.; Lu, X. *Chem. Mater.* **2014**, *26* (6), 2180–2186.
(346) Yang, A.; Huntington, M. D.; Cardinal, M. F.; Masango, S. S.; Van Duyne, R. P.; Odom, T. W. *ACS Nano* **2014**, *8* (8).
(347) Fredriksson, H.; Alaverdyan, Y.; Dmitriev, A.; Langhammer, C.; Sutherland, D. S.; Zäch, M.; Kasemo, B. *Adv. Mater.* **2007**, *19* (23), 4297–4302.
(348) Scriven, L. E. *MRS Proc.* **2011**, *121*, 717.
(349) Flamm, D. L. *Plasma Processing of Semiconductors*; Dordrecth: The Netherlands, 1997.
(350) Pigłowski, J.; Gancarz, I.; Staniszewska-Kuś, J.; Paluch, D.; Szymonowicz, M.; Konieczny, A. *Biomaterials* **1994**, *15* (11), 909–916.
(351) *Plasma Surface Modification of Polymers: Relevance to Adhesion*; Strobel, M., Lyons, C. S., Mittal, K. L., Eds.; VSP: Utrecht, 1994.
(352) Mattox, D. M. *Handbook of Physical Vapor Deposition (PVD) Processing*; Elsevier: Oxford, 1998.
(353) Hitchman, M. L.; Jensen, K. F. *Chemical Vapor Deposition Applications*; Academic Press, 1993.
(354) Hulteen, J. C.; Van Duyne, R. P. *J. Vac. Sci. Technol. A Vacuum, Surfaces, Film.* **1995**, *13* (3), 1553–1558.
(355) Haynes, C. L.; Van Duyne, R. P. *J. Phys. Chem. B* **2001**, *105* (24), 5599–5611.
(356) Hanarp, P.; Sutherland, D. S.; Gold, J.; Kasemo, B. *Colloids Surfaces A Physicochem. Eng. Asp.* **2003**, *214* (1–3), 23–36.
(357) Ai, B.; Möhwald, H.; Wang, D.; Zhang, G. *Adv. Mater. Interfaces* **2017**, *4* (1), 1600271.
(358) Zhao, J.; Jaber, S.; Mulvaney, P.; Braun, P. V.; Giessen, H. *Adv. Opt. Mater.* **2015**, *3* (5), 680–686.
(359) Frederiksen, M.; Sutherland, D. S. *Nanoscale* **2014**, *6* (2), 731–735.
(360) Ogier, R.; Shao, L.; Svedendahl, M.; Käll, M. *Adv. Mater.* **2016**, *28* (23), 4658–4664.
(361) Lodewijks, K.; Miljkovic, V.; Massiot, I.; Mekonnen, A.; Verre, R.; Olsson, E.; Dmitriev, A. *Sci. Rep.* **2016**, *6* (1), 28490.
(362) Newton, R. G. *Am. J. Phys.* **1976**, *44* (7), 639.
(363) Egerton, R. F. *Physical Principles of Electron Microscopy: An Introduction to TEM, SEM, and AEM*; Springer: New York, 2005.
(364) Betzig, E.; Chichester, R. J. *Science (80-.).* **1993**, *262* (5138), 1422–1425.
(365) Humphreys, F. . *Scr. Mater.* **2004**, *51* (8), 771–776.
(366) Nishikawa, S.; Kikuchi, S. *Nature* **1928**, *121* (3061), 1019–1020.
(367) Keller, R. R.; Geiss, R. H. *J. Microsc.* **2012**, *245* (3), 245–251.
(368) Grant, A. W.; Hu, Q.-H.; Kasemo, B. *Nanotechnology* **2004**, *15* (9), 1175–1181.
(369) Moulder, J. F.; Chastain, J. *Handbook of x-ray photoelectron spectroscopy : a reference book of standard spectra for identification and interpretation of XPS data*; Physical Electronics Division, Perkin-Elmer Corp, 1992.
(370) Khanuja, M.; Mehta, B. R.; Agar, P.; Kulriya, P. K.; Avasthi, D. K. *J. Appl. Phys.* **2009**, *106* (9), 093515.
(371) Rodahl, M.; Höök, F.; Krozer, A.; Brzezinski, P.; Kasemo, B. *Rev. Sci. Instrum.* **1995**, *66* (7), 3924–3930.

(372) Sauerbrey, G. *Zeitschrift für Phys.* **1959**, *155* (2), 206–222.
(373) Marx, K. A. *Biomacromolecules* **2003**, *4* (5), 1099–1120.
(374) Dixon, M. C. *J. Biomol. Tech.* **2008**, *19* (3), 151–158.
(375) Arnau, A.; Antonio. *Sensors* **2008**, *8* (12), 370–411.
(376) Höök, F.; Vörös, J.; Rodahl, M.; Kurrat, R.; Böni, P.; Ramsden, J. .; Textor, M.; Spencer, N. .; Tengvall, P.; Gold, J.; Kasemo, B. *Colloids Surfaces B Biointerfaces* **2002**, *24* (2), 155–170.
(377) Tjärnhage, T.; Puu, G. *Colloids Surfaces B Biointerfaces* **1996**, *8* (1–2), 39–50.
(378) Reimhult, E.; Larsson, C.; Kasemo, B.; Höök, F. **2004**.
(379) Bailey, L. E.; Kambhampati, D.; Kanazawa, K. K.; Knoll, W.; Frank, C. W. **2001**.
(380) Wang, G.; Rodahl, M.; Edvardsson, M.; Svedhem, S.; Ohlsson, G.; Höök, F.; Kasemo, B. *Rev. Sci. Instrum.* **2008**, *79* (7), 075107.
(381) Edvardsson, M.; Svedhem, S.; Wang, G.; Richter, R.; Rodahl, M.; Kasemo, B. *Anal. Chem.* **2009**, *81* (1), 349–361.
(382) Bucur, R. V.; Flanagan, T. B. *Zeitschrift für Phys. Chemie* **1974**, *88* (5_6), 225–241.
(383) EerNisse, E. P. *J. Appl. Phys.* **1972**, *43* (4), 1330–1337.
(384) Frazier, G. A.; Glosser, R. *J. Phys. D. Appl. Phys.* **1979**, *12* (10), L113–L115.
(385) Frazier, G. A.; Glosser, R. *J. Less Common Met.* **1980**, *74* (1), 89–96.
(386) Papathanassopoulos, K.; Wenzl, H. *J. Phys. F Met. Phys.* **1982**, *12* (7), 1369–1381.
(387) Feenstra, R.; Bruin-Hordijk, G. J. de; Bakker, H. L. M.; Griessen, R.; Groot, D. G. de. *J. Phys. F Met. Phys.* **1983**, *13* (2), L13–L18.
(388) Feenstra, R.; Groot, D. G. de; Rector, J. H.; Salomons, E.; Griessen, R. *J. Phys. F Met. Phys.* **1986**, *16* (12), 1953–1963.
(389) Rydén, J.; Hjörvarsson, B.; Ericsson, T.; Karlsson, E.; Krozer, A.; Kasemo, B. *J. Less Common Met.* **1989**, *152* (2), 295–309.
(390) Rocklein, M. N.; George, S. M. *Anal. Chem.* **2003**, *75* (19), 4975–4982.
(391) Langhammer, C. Nanoparticle Plasmons in Classic and Novel Materials - Fundamentals and Hydrogen Sensing, Chalmers University of Technology, 2009.
(392) Poyli, M. A.; Silkin, V. M.; Chernov, I. P.; Echenique, P. M.; Muiño, R. D.; Aizpurua, J. *J. Phys. Chem. Lett.* **2012**, *3* (18), 2556–2561.
(393) Jonsson, M. P.; Jönsson, P.; Höök, F. *Anal. Chem.* **2008**, *80* (21), 7988–7995.
(394) Zhu, J.; Huang, S.; Ye, J.; Zhang, X.; Liu, G. *Sensors Actuators A Phys.* **2015**, *229*, 141–146.
(395) Larsson, E. M.; Edvardsson, M. E. M.; Langhammer, C.; Zorić, I.; Kasemo, B. *Rev. Sci. Instrum.* **2009**, *80* (12), 125105.
(396) Mubeen, S.; Zhang, S.; Kim, N.; Lee, S.; Krämer, S.; Xu, H.; Moskovits, M. *Nano Lett.* **2012**, *12* (4), 2088–2094.
(397) Moskovits, M.; Srnová-Šloufová, I.; Vlčková, B. *J. Chem. Phys.* **2002**, *116* (23), 10435.
(398) Rioux, D.; Vallières, S.; Besner, S.; Muñoz, P.; Mazur, E.; Meunier, M. *Adv. Opt. Mater.* **2014**, *2* (2), 176–182.
(399) Verre, R.; Odebo Länk, N.; Andrén, D.; Šípová, H.; Käll, M. *Advanced Optical Materials*. Wiley-Blackwell April 1, 2018, p 1701253.